THE UNIVERSITY OF CHICAGO

HIGH BRIGHTNESS PHOTOELECTRON BEAMLINES

FOR FEMTOSECOND SCIENCE

A DISSERTATION SUBMITTED TO

THE FACULTY OF THE DIVISION OF THE PHYSICAL SCIENCES

IN CANDIDACY FOR THE DEGREE OF

DOCTOR OF PHILOSOPHY

DEPARTMENT OF PHYSICS

BY

MATTHEW A. GORDON

CHICAGO, ILLINOIS

AUGUST 2022

For my family, both in blood and in action.

"If I had more time I would have written a shorter letter" - Attributed to many people

TABLE OF CONTENTS

LIST OF FIGURES

LIST OF TABLES

ACKNOWLEDGMENTS

I would like to start by thanking Young-Kee for being my advisor. You have given me a holistic view of what it means to be a physicist. Your support over the years has driven me forward and you have focused my priorities on what truly matters.

Thank you Jared Maxson, who over the years has given me the opportunity to work along side him and his group at Cornell. It has been a challenging but rewarding journey, and I will treasure it always.

Stas, thank you for all of the life lessons and fun discussions we had over the years. Your mathematical rigor was only matched by the strength of your morals. I wish the best for you and your family.

I would like to thank my thesis committee, who helped make my knowledge in accelerators well rounded. In particular, I would like to given special thanks to Sergei, who has been vital in the development of my science communication skills.

Brendan, Chih-Kai, Jody, Kyle, Lipi, Mark, Melody, and Nikita, the five plus years I have gotten to know you all here has been amazing. I couldn't begin to compare the impacts you all have had on my life, so I put you in alphabetical order. I consider you all family, thanks for the crazy times we had.

I would be wrong not to thank the friends I worked along side at Cornell as well. Adam, Cameron, Chad, Michael, and William, thanks for the crash course on how to be an experimentalist.

I dedicate this dissertation to my family, without which, I would not be who I am today. I can not thank you all enough for everything you have done for me. I love you all, through all of the highs and the lows we have had together.

ABSTRACT

Particle accelerators can be used as cameras, creating bunches of electrons or X-ray pulses which can produce images of objects smaller than what can be resolved with visible light. Denser and colder electron bunches create higher resolution images both in space and time. The development of high brightness photocathodes is a driving force in the improvement of accelerators used for time resolved science. In this thesis, a fundamental limit in the creation cold dense electron beams from photocathodes is presented and simulated. Additionally, methods for preserving the quality of cold dense electron beams in transport are simulated and experimentally demonstrated in an operating ultrafast electron diffraction beamline.

CHAPTER 1

INTRODUCTION

Studying matter at atomic resolutions has been made possible through techniques including electron diffraction, electron microscopy, x-ray absorption and diffraction. From small crystals, to biological molecules, such as proteins, DNA, and viruses, these techniques have advanced our understanding of physics, chemistry, and biology.

But nature does not exist in a static state. A full understanding of the dynamics of a biological molecule, chemical reaction, or phase transition cannot be understood with a single image of a structure. Instead, a series of images must be made during the dynamics. To see what is happening during a process, a series of images needs to be taken. Like a camera taking pictures of an object in motion, the shutter/integration time of these images needs to be small or else the images will be blurred.

Images from diffraction and microscopy experiments need to integrate a signal of particles, either electrons or photons, over an extended period of time. The amount of time needed for the integration is dependent on the incoming flux of particles, as well as the interaction probability between the particles and the sample being studied. In state of the art detectors, the minimum integration time is on the order of microseconds [1].

The timescales for many processes in nature are much smaller than this however. Processes like melting and protein folding happen on the time scale of nanoseconds. Phase transitions, phonon vibrations, breaking and forming chemical bonds happen even faster, on the time scale of femtoseconds [2, 3, 4]. None of these are possible to study with a continuous integration of particles used to form images in the techniques described above.

Thus there is a need to create images resolved in space to the atomic scale, but simultaneously resolved in time on the femtosecond scale. This additional simultaneous constraint comes with many challenges, both fundamentally and technologically and necessitated the creation of a new generation of instruments and techniques that are still being refined today.

This thesis introduces some solutions to the problems that come with this challenge as well as details a new issue that will soon need to be addressed as the push for higher resolution continues.

1.1 An Overview of Time-Resolved Electron and X-ray Beams

Ultrafast electron diffraction(UED), ultrafast electron microscopy(UEM), and the X-ray free electron laser (XFEL) are three of the most powerful modern tools/techniques for time-resolved science [5, 6, 7, 8]. This thesis will focus on UED, however, to understand the role UED has in time-resolved science, it is essential to understand all of the available tools to be able to compare their strengths and weaknesses. One important difference in these techniques is the particle type used for imaging, electrons vs. X-rays. The advantages and disadvantages of using one type of particle vs. the other will be discussed in the next section.

One of the most prevalent methods of producing a short electron beam today is through shining a light onto a metal surface, known as a photocathode. If the frequency of the light is large enough for a given metal, electrons in the metal will absorb a photon and be emitted from the metal in what was coined by Einstein in 1905 as the photoelectric effect [9]. The development of photocathodes for electron beams was propelled by the invention of the laser, the first of which was made in 1960 by Theodore Maiman [10]. The development of short laser pulses, down to the scale of femtoseconds would then allow for the generation of equally short electron pulses from photocathodes using these lasers. These short electron pulses from photocathodes allow for the short shutter times needed for UED.

The development of X-ray sources started with the discovery of the X-ray in 1895 by Wilhelm Röntgen. Within two weeks of the discovery, Wilhelm was able to take a picture underneath the skin of his wife's hand. This penetration capability was highly desired by the medical community and would soon draw interest from the scientific community. The development of X-ray sources was forever changed with the observation of synchrotron

radiation in 1947. The radiation of charged particles in circular accelerators was first thought to be a nuisance, however, the collimated X-ray source quickly was seen as invaluable, and in the following decades, dedicated machines were made specifically for the generation of this radiation. However, synchrotron sources still suffered from a lack of high temporal resolution. Thus, the demand remained for a X-ray laser. This demand would lead to the development of the XFEL, in which a high energy micro-bunched electron beam is oscillated in a magnetic device called an undulator, to produce highly coherent X-ray pulses. [11, 12].

1.2   Electrons vs. X-rays

Electrons and X-rays are known to be complementary in their ability to probe matter, both in the static and ultrafast regimes. X-rays primarily interact with electrons in matter while electrons as charged particles interact both with electrons and atomic nuclei. Because of the difference in the nature of their interaction, electrons are much more likely to scatter from a material, both elastically and inelastically. Electrons at keV energy scales have a scattering cross-section 10^4 - 10^6 times larger than X-rays. While this provides more useful elastic scattering events per incident particle, the inelastic scattering of electrons and ejected valence electrons from the sample create additional background in diffraction images. If energy filtering can be used to separate the background, then using electrons can result in less radiation damage relative to X-rays, which is advantageous in situations where sample deterioration inhibits measurement. Additionally, the low energy electron beams allow UED devices to have a size on the order of meters while XFELs are on the scale of kilometers. However, electron repulsion limits pulse density/pulse charge, making simultaneously large spatial and temporal resolution more difficult to achieve. Because of this, XFELs can typically run at much higher fluxes than electron diffraction devices, 10^6 times more or higher, making up for the loss in scattering cross section while having higher temporal resolution [5, 8, 13, 14, 15].

1.3   A Brief History of UED

The first time-resolved electron diffraction experiments occurred at the University of Rochester in the mid 1980s. S. Williamson, G. Mourou, and J. C. M. Li. used an optical streak camera to create electron pulses with pulse lengths of 20 ps, with a final beam energy of 25 keV and 10^4 electrons per pulse. A schematic of their setup from their original paper [16] is shown in fig. 1.1. They used this apparatus to study the melting of aluminum. The results of their experiment, while misinterpreted from the data [17], went on to spark a wide range of experiments in time-resolved electron diffraction.
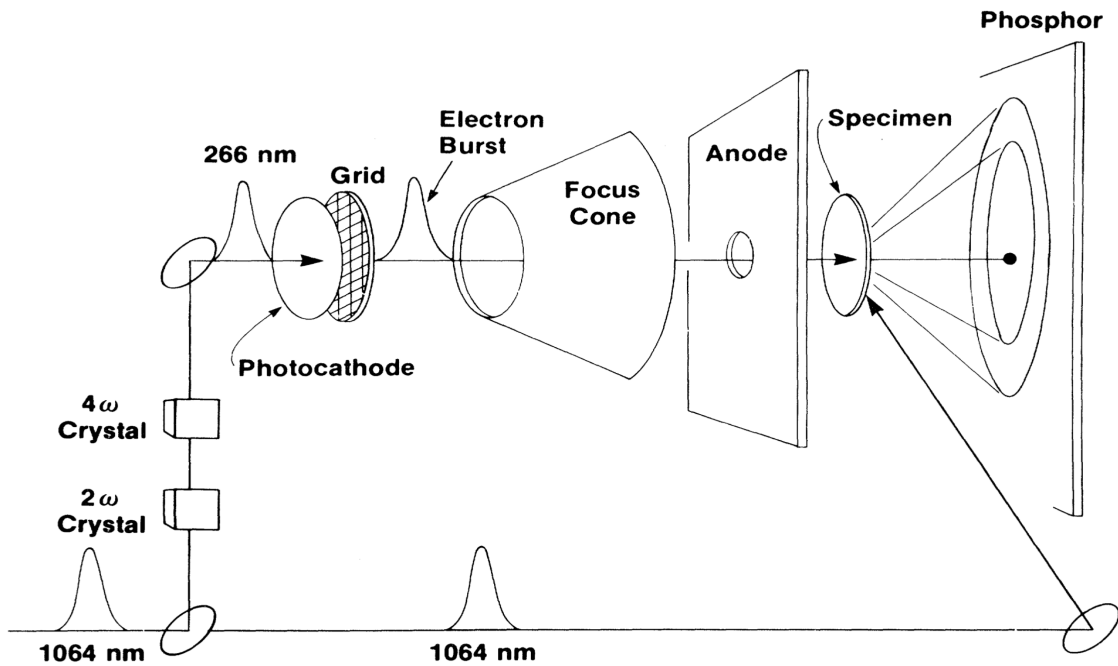
Figure 1.1: Schematic of the picosecond electron diffraction setup used by Williamson, Mourou and Li. A streak camera is used to make a 20 ps electron bunch which would be accelerated to 25 keV and diffract through an Aluminum sample.

H. E. Elsayed-Ali would join Mourou at the university of Rochester for the next development. While the original experiment was done through the diffraction of transmitted electrons in aluminum, this next experiment would use the diffraction of reflected electrons from a 250 Angstrom gold film with 150 ps electron pulses. This would allow for the study

of the first few mono-layers of atoms of a material, without the material needing to be thin enough for the electron beam to transmit through [18].

J.C. Williamson, M. Dantus, S.B. Kim, and A.H. Zewail from Caltech would make the next major development. The group was able to bring the electron pulse length, from time scales of ps, down to tens of femtoseconds using fs scale laser pulses. At high intensities, coulomb repulsion would extend these short electron pulses up to 10 ps. Nonetheless, for reversible processes, this provided a way of measuring dynamics on the fs scale [19].
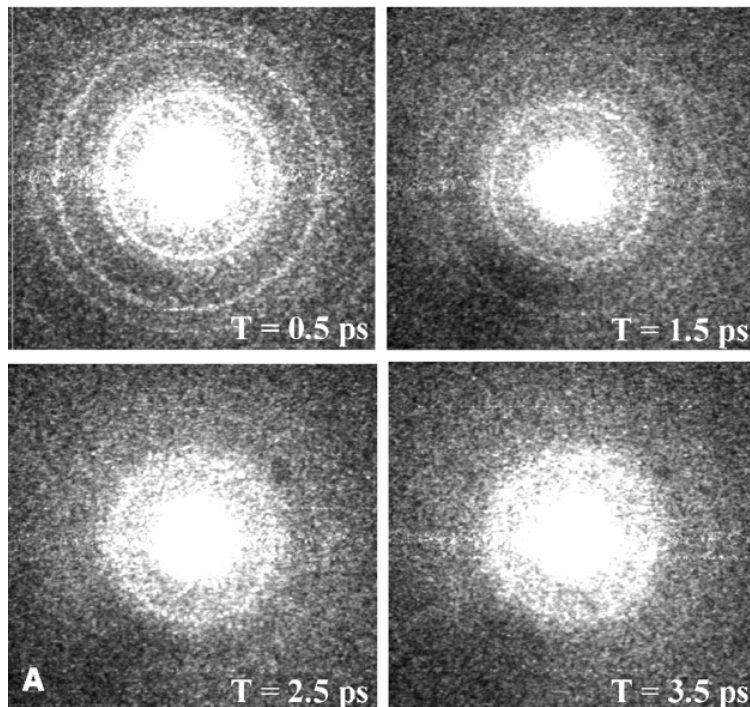
Figure 1.2: UED of melting aluminum done by B.J. Siwick et. al. The disappearance of the diffraction rings corresponds to the transition to the liquid phase, which is seen to occur on the time scale of 3.5 ps.

The study of time-resolved non-reversible dynamics would not come until much later, in 2003, where B.J. Siwick, J.R. Dwyer, R.E. Jordan, and R.J. Dwayne Miller would repeat the time-resolved diffraction of the melting of aluminum, shown in fig. 1.2 from [20], now with a 600 fs electron pulse. With this much shorter electron pulse, they found that the diffraction rings indicative that the aluminum was solid, would disappear on the time scale of 3.5 ps

[20]. In the original experiment, the 20 ps electron pulse was much larger than the time it took for the dynamics to occur, thus making it impossible to measure.

The continued prevalence of UED today is largely due to the advancement of the MeV UED beamline [13]. At higher beam energies, it has become possible to create fs scale electron beam lengths with appreciable bunch charges, between 1-100 fC. This has allowed insights in phenomenon in a large range of materials, from those as ubiquitous as water to exotic quantum materials [7, 21, 22, 23, 24, 25, 26, 27].

Going to higher energies is not the only method to achieve short dense electron beams. With the addition of an RF bunching cavity, a longitudinal energy correlation can be made on the beam, allowing for bunch length compression. With this, UED beamlines are capable of starting off with a much longer electron beam, mitigating the effects of electron repulsion to a brief moment when the beam comes to a longitudinal focus near the sample being studied. This method has allowed keV energy scale UED beamlines to achieve similar temporal resolution.

UED has room for further improvement today through beamline specialization, increasing the scope of the processes that can be studied. Samples with larger periodic structures require electron beams with small momentum spreads. Samples that are difficult to grow over extended areas need equally small electron beam sizes to study. With a combination of many devices specialized for studying different types of samples and dynamics, UED remains a prominent tool in time-resolved science.

CHAPTER 2

BEAM DYNAMICS IN LINEAR ACCELERATORS

The time-resolved devices described in chapter one are examples of particle accelerators. Accelerators use electromagnetic fields to accelerate and manipulate charged particles. Understanding the physics of particle accelerators requires knowledge of classical mechanics, special relativity, and electromagnetism.

2.1 Charged Particle Dynamics

The dynamics of a charged particle in an electric field $\vec{E}$ and magnetic field $\vec{B}$ are governed by the Lorentz force law:

$$\frac{d\vec{p}}{dt} = \vec{F} = q(\vec{E} + \vec{v} \times \vec{B}) \tag{2.1}$$

where q is the charge of the particle, $\vec{v}$ is its velocity and $\vec{p}$ is the relativistic momentum of the particle:

$$\vec{p} = \gamma m \vec{v} \tag{2.2}$$

where m is mass and gamma is the Lorentz factor, $\gamma = \frac{1}{\sqrt{1 - v^2/c^2}}$, and c is the speed of light [28]. The relativistic form of the law here is essential as electrons in UED devices are accelerated to have kinetic energies on the order of, or greater than their rest energy.

2.1.1 Accelerator Beamline Elements and Mathematical Formulation

A charged particle accelerator is composed of a series of elements, including empty beam pipe segments called drifts, magnets, a particle source like an electron gun, and radiofrequency (RF) cavities. A description of each of these elements used in UED as well as how they are used is described here.

The coordinate system used for describing motion of charged particles in linear acceler-

ators, which will be used throughout this dissertation, aligns the z-axis with the direction of travel of the electron beam. The origin of the xy-plane is chosen to be the center of the ideal particle trajectory, typically the center of a round beam pipe. The z-direction is therefore referred to as the longitudinal direction while the x and y directions are referred to as transverse directions, in relation to the direction the beam travels.

The terminology of linear accelerator is used to differentiate from circular accelerators. In a linear accelerator, particles pass through a set of beamline elements once. In a circular accelerator, particles will go through a periodic structure of beamline elements, often called a lattice, multiple times. The distinction between these is simple, however, it results in differences in the mathematical formulation that is best suited to describe the dynamics.

In circular accelerators, particles must by definition return to the same longitudinal position multiple times. Each time a particle returns to a longitudinal position, it will have some transverse phase space coordinate, as well as a longitudinal velocity. The collection of transformations of the phase space coordinates as the particle goes around the accelerator can be thought of as a map. This formulation is quite fruitful, as a major concern in many circular accelerators is to prevent the loss of particles over many turns, a problem which in this formulation corresponds to the region of stability of the map.

In linear accelerators by contrast, particles only travel through each element once. The idea of maps can still be used on individual elements, although stability over multiple applications of a map is not as much of a concern, so I will not use that framework. A relativistic Newtonian framework is sufficient for discussing the beam dynamics for UED beamlines, and will be used throughout this dissertation.

Drifts

In an ideal drift, there are no external electric and magnetic fields. Therefore, a single electron traveling through an ideal drift experiences 0 forces. While a drift therefore is not inherently

an interesting element, it is nevertheless necessary. A force from an applied electric or magnetic field on a charged particle needs time for a momentum change to result in a change in the position of the particle. Because these particles are travelling through the accelerator, any time requirement inherently corresponds to a length requirement. Additionally, drifts inherently provide a way of measuring the transverse momentum of an electron beam, as the change of momentum over a drift is 0, thus the change of transverse position over a drift can be used to directly calculate momentum.

Dipole Magnets

A dipole magnet, depicted in fig. 2.1 consists of 1 pair of north-south poles. For the ideal dipole magnet depicted, the magnetic field created by the dipole is $\vec{B} = -B_y \hat{y}$ everywhere ignoring effects from finite size. For a particle traveling no transverse velocity, $\vec{v} = v_z$, the force that the particle experiences using equation 2.1 is:

$$\vec{F}_{dipole} = q v_z B_y \hat{x} \tag{2.3}$$

Thus an ideal dipole magnet can be used to move an electron beam uniformly in a transverse direction perpendicular to the orientation of the dipole [29]. In linear accelerators, one primary use of dipole magnets is to steer the beam. This is done to bring the beam close to the beams ideal trajectory in the beam pipe.

Quadrupole Magnets

A quadrupole magnet, depicted in fig. 2.2 has 2 pairs of north south poles with alternating polarity separated by 90 degrees from its nearest neighbor around the xy-plane. With a south pole in the positive x, positive y quadrant, the resulting ideal magnetic field is: $\vec{B} = K(y\hat{x} + x\hat{y})$ where K is the strength of the quadrupole, again ignoring effects of finite size.
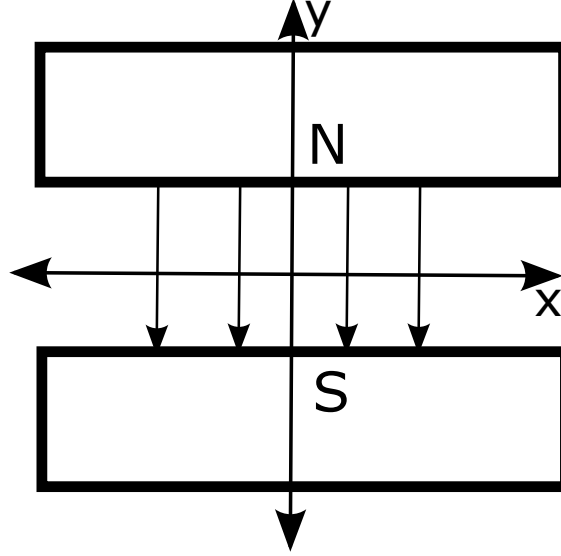
Figure 2.1: Depiction of a dipole magnet oriented along the y-axis.

This results in a force using equation 2.1 of:

$$\vec{F}_{quadrupole} = -qKv_z(x\hat{x} - y\hat{y}) \tag{2.4}$$

For a negatively charged particle, $q < 0$, and a positive quadrupole strength, $K > 0$, this force is linearly defocusing in x and linearly focusing in y. By using pairs of quadrupole magnets with one rotated 90 degrees respect to the other, it is possible to create a structure, called a FODO lattice, that if repeated, can contain the beam in both x and y [29]. Rotating the quadrupole by 45 degrees results in what is called a skew quadrupole. A skew quadrupole introduces correlations between the x and y axes which can be troublesome in experiment.

Sextupole Magnets

A sextupole magnet, depicted in fig. 2.3 has 3 pairs of north south poles with alternating polarity separated by 60 degrees from its nearest neighbor around the xy-plane. With a north pole in the direction of positive y, the magnetic field from the ideal sextupole is $\vec{B} = G(2xy\hat{x} + (x^2 - y^2)\hat{y})$, where G is the sextupole strength. Using equation 2.1, the force
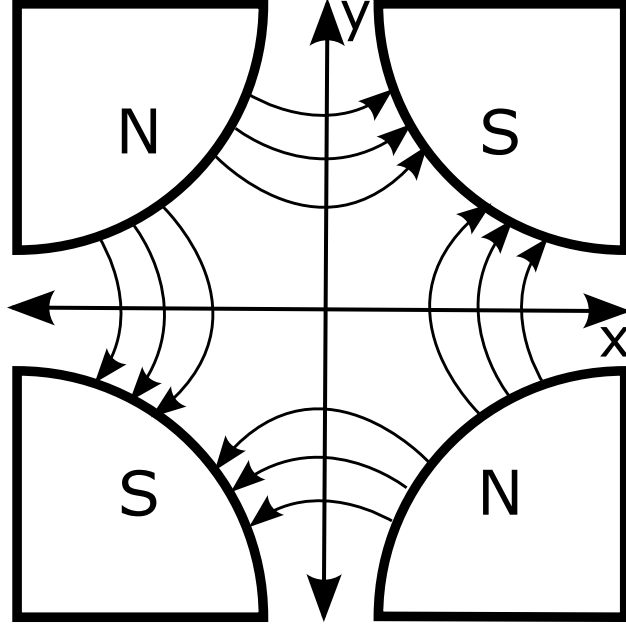
Figure 2.2: Depiction of a quadrupole magnet with North poles in quadrants 2 and 4 and south poles in quadrants 1 and 3.

from this sextupole is:

$$\vec{F}_{sextupole} = -Gqv_z((x^2 - y^2)\hat{x} - 2xy\hat{y}) \tag{2.5}$$

The force from the sextupole is non-linear, and couples the x and y directions. This is typically bad in accelerators as it can lead to particle loss if not controlled. The main use of sextupoles is to correct the focusing of quadrupole magnets, which as seen from equation 2.4, is dependent on the longitudinal velocity of the particle. In a high energy beam of particles, there is going to be a non-negligible spread in the longitudinal velocity of the beam, which will result in different parts of an electron beam coming into focus at different longitudinal positions. Sextupoles can be used to correct for this effect [29].
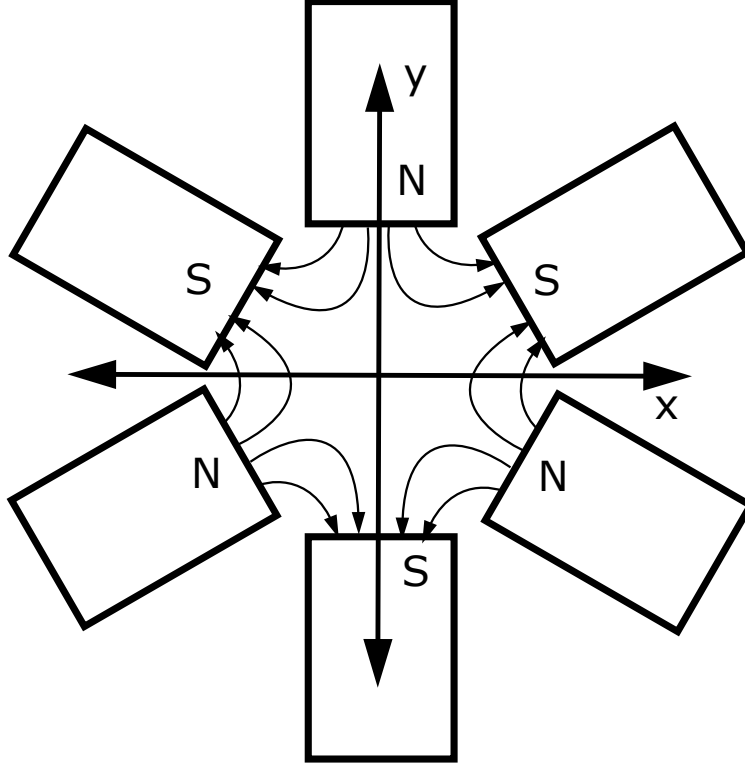
Figure 2.3: Depiction of a sextupole magnet with a north pole in the positive y direction.

Solenoids

A solenoid magnet in an accelerator is best described in cylindrical coordinates where $r = x^2 + y^2$ and $z = z$. In this coordinate system a solenoid has a constant current density on its surface, or bulk in the case of a thick solenoid, in the ϕ direction. The magnetic field from this solenoid is:

$$
\begin{aligned}
B_z(r, z) &= B(z) - \frac{r^2}{4} B''(z) + ... \\
B_r(r, z) &= -\frac{r}{2} B'(z) + \frac{r^3}{16} B'''(z) + ...
\end{aligned}
$$

(2.6)

where B(z) is an arbitrary field profile [30]. If we assume a hard edge solenoid of length L, positioned between z=0 and z=L, with a constant field B_0 inside, these equations simplify

to:

$$B_z(r, z) = B_0(H(z) - H(z - L))$$

$$B_r(r, z) = -\frac{r}{2}B_0(\delta(z) - \delta(z - L))$$

(2.7)

where here H is the Heaviside function and I ignore higher order derivatives to the Dirac delta as changes to momenta of particles will rely on a single integral of B. For a particle with initial velocity $\vec{v} = v_z\hat{z}$ and radius r_0 entering the solenoid at z = 0, it will experience a force of:

$$\frac{d\vec{p}}{dt} = \frac{qB_0r_0v_z}{2}\delta(z)\hat{\phi}$$

(2.8)

Switching variables $t = z/v_z$, and using the relativistic equation for momentum, equation 2.2, and integrating over a small distance around z = 0, the charged particle gets an imparted velocity of:

$$\Delta\vec{v} = \frac{qB_0r_0}{2m\gamma}\hat{\phi}$$

(2.9)

In the presence of the magnetic field in the solenoid pointed in the z direction, this will result in a resulting change in the radial velocity at the end of the solenoid, z = L, which in the case of a thin lens, $v_z \gg \frac{qB_0L}{2m\gamma}$ is given in [30] and repeated here:

$$\Delta\vec{v} \approx -r\frac{q^2B_0^2L}{4m^2\gamma^2v_z^2}\hat{r}$$

(2.10)

Thus, a solenoid magnet can act as a linear radially focusing lens. However the focusing power is proportional to $1/\gamma^2$ so this is mainly used on lower energy particles.

Electron Gun

A simplified depiction of a DC electron gun is shown in figure 2.4. In this figure, a negatively biased cathode is brought close to a grounded anode. Electrons emitted from the cathode

are accelerated by the gradient of the electrical potential between the cathode and anode. Electrons are then allowed to escape through a hole in the anode where they then will be transported through the remainder of the beamline.
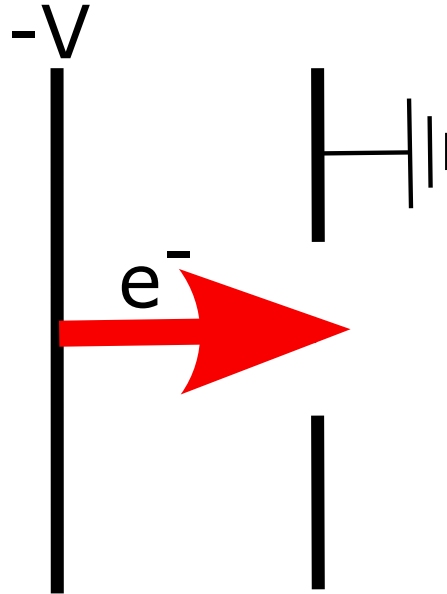
Figure 2.4: Depiction of a simplified electron gun, a diode with a hole in the anode to allow the electrons to escape.

The electron gun thus has two roles, one to house the electron source, which I will be mainly focusing on photocathodes, and to accelerate the electrons relativistically immediately after emission, which will be seen to be important when considering the effects of Coulomb repulsion. The electron gun can be shaped to focus or defocus the produced electron beam. Additionally, the presence of the cathode boundary condition can have significant impact on the dynamics of a produced beam, which will be discussed further in chapter 5.

RF Cavities

The final beamline element that will be discussed briefly is the RF cavity. A RF cavity houses discrete electric and magnetic modes with allowed frequencies determined by the geometry of the cavity [28]. By sending an electron beam into a RF cavity, it is possible to

extract or input energy from a mode into the beam. Thus an RF cavity is flexible in its uses, some examples of these include accelerating electron beams, compressing electron beams longitudinally, and turning longitudinal correlations in a beam to transverse correlations.

For acceleration, traveling wave cavities provide acceleration to charged particles by matching the phase velocity of the wave to the particles velocity. By doing so, as the particle beam travels through the cavity, the beam will remain in a phase with an accelerating electric field. This is primarily done with particles that are already ultra-relativistic, so that the velocity change the particle experiences does not cause the particles position to change with respect to the traveling wave. However, RF cavities are capable of accelerating particles over smaller spaces compared to DC accelerating techniques, so RF acceleration techniques have been used in electron guns, bringing particles from nearly at rest to relativistic velocities [31]. This can be done without splitting the beam longitudinally as long as the total phase drift over the acceleration distance does not result in part of the beam experiencing a decelerating electric field.

2.1.2 Coulomb Interaction

An electron, as a charged particle, generates an electric field of its own:

$$\vec{E} = \frac{1}{4\pi\epsilon_0}\frac{q\hat{r}}{r^2} \tag{2.11}$$

where ϵ_0 is the permittivity of free space. Therefore, all charged particles experience a force from all other charged particles as described by the Lorentz force, this force is known historically as Coulombs law.

$$\vec{F} = \frac{1}{4\pi\epsilon_0}\frac{q_1 q_2 \hat{r}}{r^2} \tag{2.12}$$

where here q_1 and q_2 are the charges of the 2 particles, and r is the distance between them [28].

An electron beam is a collection of densely packed charged particles, and due to the inverse square nature of Coulomb's law the forces between particles in a beam can significantly affect the dynamics of charged particles.

This effect is however suppressed for relativistic particles. To see this, lets assume we have an infinitely long beam of particles with radius R and charge density ρ_0 moving purely longitudinally at a speed v_z. In the co-moving frame, which will be denoted with a $*$, there are no magnetic fields acting on the beam as all particles are at rest in this frame, and there are no longitudinal forces due to symmetry. The force created by this beam on a test charge q at a distance r is:

$$F_r^*(r) = \begin{cases} \frac{q\rho_0^*}{2\epsilon_0}r & r < R \\ \frac{q\rho_0^*}{2\epsilon_0}\frac{R^2}{r} & r < R \end{cases} \tag{2.13}$$

Transforming back to the frame in which the beam is moving, the force, $F_r^* = dp_r^*/dt^* = dp_r/d(t/\gamma) = \gamma F_r$. Additionally, $\rho_0^* = \rho_0/\gamma$ due to the longitudinal length contraction. Looking at the force on an individual particle inside of the beam, $r < R$ thus gives the formula:

$$F_r(r) = \frac{q\rho_0}{2\epsilon_0\gamma^2}r \tag{2.14}$$

From this equation, it can be seen the transverse space charge force is suppressed by a factor of $1/\gamma^2$. This relativistic suppression of space charge forces enables stability of high density charge bunches [29].

While ultra-relativistic particles, $\gamma \gg 1$, will therefore not interact strongly through direct Coulomb interaction, they can interact through the radiation fields. For collections of particles in the limit of $v \to c$, this interaction will effect particles behind the particle emitting the radiation. These radiation field effects are the most pronounced when the

beam pipe is far from a perfect conducting surface, or the cross section of the beam pipe changes over short longitudinal distances [32]. These radiation fields, scattered off of these boundaries, often called wakefields, can be both harmful and beneficial. In the worst case, these fields can cause instabilities, where each electron bunch in an accelerator provides a transverse kick to the bunch behind it, displacing its transverse position and amplifying the kick it provides on the bunch behind it, leading to eventual particle loss. However, by careful calculation and positioning of particle bunches, it is possible for charged bunches to provide focusing as well as accelerating fields to a trailing bunch, in a technique called wakefield acceleration [33]. A fast calculation of wakefields in a dielectric structure is discussed in appendix A.

2.1.3   Mean-Field Approximation and Space Charge

Tracking the individual force contributions from each particle in a beam on every other particle becomes intractable both analytically and computationally. Instead, it is useful to consider a beam as a continuum of charge distributed over a region of space. The potential of this charged fluid can be calculated and from this, and the force acting on each particle can be approximated from this mean-field potential. These forces are often referred to as space charge forces. Space charge forces can be used to calculate quantities such as the maximum current density that can be extracted from a cathode, the Child-Langmuir law, as well as the effective defocusing of a beam [34].

Mean-field calculations of the electric potential of an electron beam have been essential to the analytic study of, as well as simulation of accelerators with large beam densities. If simulating in the time domain, each time step of a simulation requires a calculation of the Coulomb forces from the particles in the beam. An exact calculation of this scales with the number of particles in the beam squared $\mathcal{O}(N^2)$. Comparatively, a mean field calculation of the forces can scale approximately as $\mathcal{O}(N)$ [35].

2.2 Accelerator Simulations

Accelerators are complicated and diverse machines. They come in sizes of less than a meter to tens of kilometers. They are used to produce radiation, to collide particles for studying basic physics, and to produce particles in a large range of energies for various uses. The difference in scale, complexity, geometry, and application mean that there is not one single agreed upon simulation code to simulate what is going on in every accelerator. On the contrary, the number of simulation codes available is in the hundreds [36].

Each code has its own use case and set of physics that it models well. Some codes are good for circular machines, with simulation techniques that ensure conservation of energy at every step, which while true in all accelerators, becomes an issue when you track a particles dynamics over a large number of revolutions. Some codes include computation of space charge, which as shown in section 2.1.2, is vital for low energy accelerators. Some include the effects of radiation of accelerated charged particles. The list of differentiating features is extensive as many codes were designed specifically for one particular beamline or application. For these reasons, an exhaustive discussion of different accelerator codes is beyond the scope of this work.

Instead, it is beneficial to discuss what features should be included in a code for simulation of a UED beamline. The first step of a UED beamline in the creation of the electron beam. A short laser pulse is used to create the electron pulse. Any simulation tool used for UED therefore must either allow the generation of an electron beam based on a given laser profile, or allow the user to input a custom electron distribution created from another tool which can. One of the biggest limiting factors in the time resolution of UED beamlines is the Coulomb interaction, so it is vital that some implementation of it is included. Additionally, the ability to include arbitrary time dependent electromagnetic field maps allows for the simulation of all the necessary beamline elements discussed in section 2.1.

One class of codes that can meet all of these codes are 3D particle tracking codes, in

particular, those that work in the time-domain. For each time step in the simulation, the code propagates the particles forward using the Lorentz force, equation 2.1. Coulomb forces can be calculated directly for small numbers of particles, or with a mean-field algorithm for large numbers of particles.

2.3   Emittance

The 6d phase space volume that a beam takes up is a conserved quantity under Liouville's theorem, with a few caveats. The number of particles in a beam is not infinite, it is possible to exchange the phase space positions of particles and holes, possibly decreasing the volume. Electrons radiate when they are accelerated, this dissapitive force is not covered under Liouville's theorem. The Coulomb force also violate the assumption of the divergence free nature of the velocity field. However, if the contribution to the impulse on any given particle is dominated by the effects of the beam as a whole, instead of nearby particles, the mean-field approximation can be used, which is divergence free. Despite all of these caveats, the phase space volume is still closely conserved in many accelerator systems [37]. Furthermore, in systems with minimal coupling between dimensions, the individual dimensions phase space volume is conserved as well. The emittance, calculated as an rms quantity, is related to the phase-space volume, and thus is close to a conserved quantity. The effects of the emittance being calculated as an rms quantity are discussed in section 2.3.1.

Fig. 2.5 is representative of what the phase space of an electron beam looks like in one transverse dimension while the beam is defocusing in that direction. The normalized rms emittance in this transverse dimension is:

$$\epsilon_{n,rms} = \frac{1}{mc}\sqrt{<x_s^2><p_{x,s}^2> - <x_s p_{x,s}>^2} \qquad (2.15)$$

where in this $<u>$ represents the average of a quantity u and the subscript s indicates that

the phase space coordinate has its mean subtracted from it. The definition of emittance is discussed in many textbooks on accelerator physics including [29]. I will suppress the subscript s going forward to simplify notation with the understanding that all phase space coordinates of a beam will now be considered with their mean subtracted. Additionally, quoted values of the emittance will always be the normalized rms emittance, so the rms subscript will also be dropped. The notion of normalized emittance is in comparison to the geometric emittance. Multiplying the geometric emittance by a factor of γ results in the normalized emittance. The normalized emittance will be used in this dissertation as it is conserved as a beam is accelerated [38].
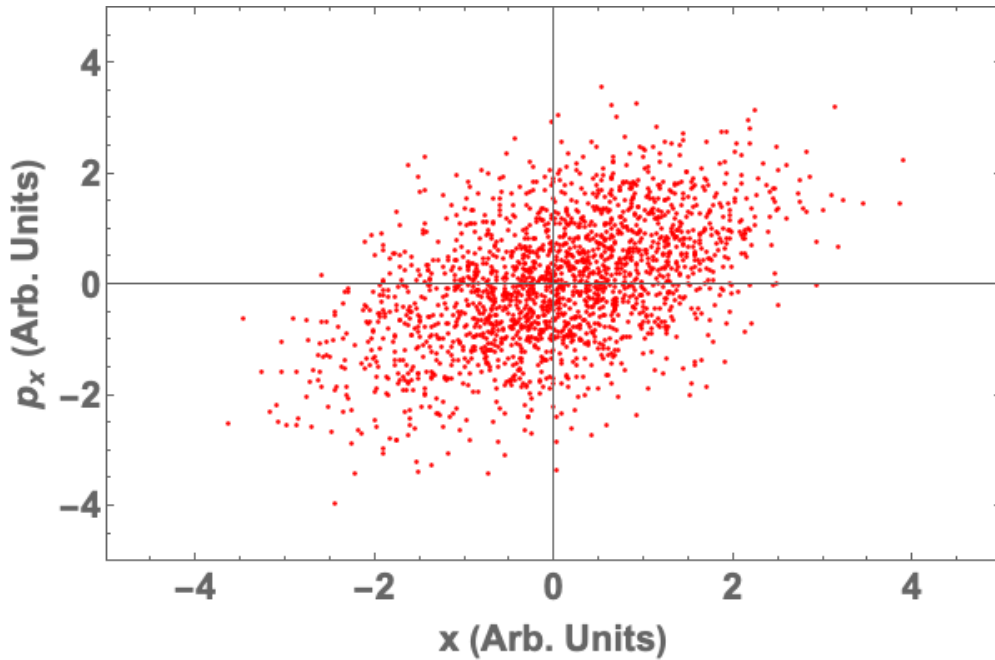
Figure 2.5: $x - p_x$ phase space of a fictitious electron beam. Each red dot represents the x-px phase space coordinate of a single electron.

A linear force acting on a beam of particles will conserve the rms emittance. The effect of a linear force on a beam, such as from a quadrupole magnet or solenoid, causes the beam to tilt in phase space. Fig. 2.6 depicts the effect of a linear focusing force which changes a diverging beam, with positive $x - p_x$ correlation, into a converging beam, with negative $x - p_x$ correlation. Looking at equation 2.15, the linear correlation $< xp_x >$ is subtracted

out in the calculation of the emittance, thus will not effect the emittance calculation.
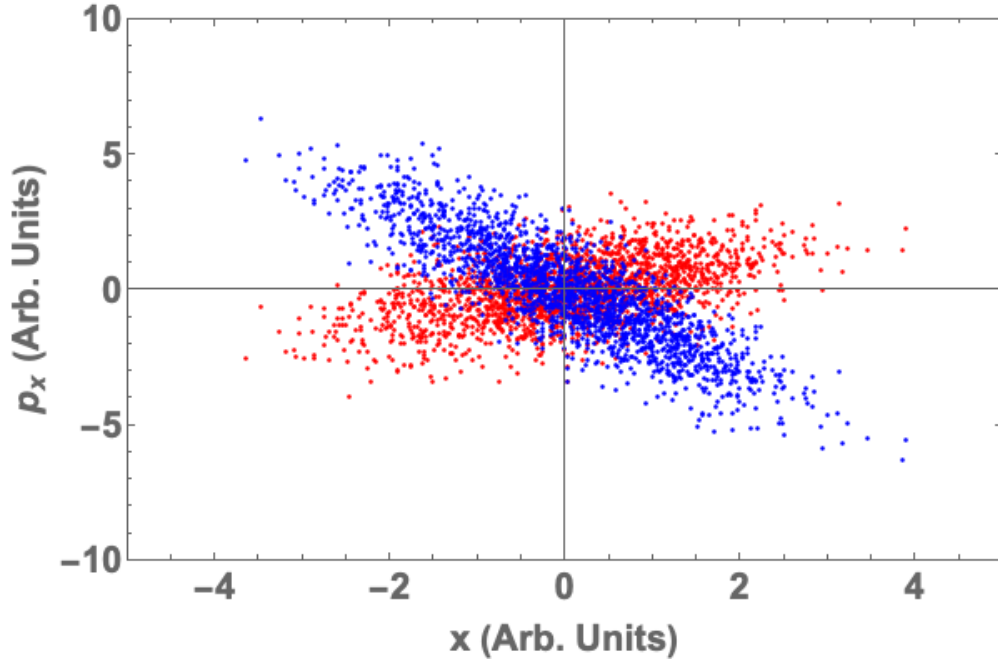
Figure 2.6: $x - p_x$ phase space of 2 fictitious electron beams. Each red dot represents the x-px phase space coordinate of a single electron and each blue dot represents its phase space coordinate after experiencing a linear force.

We can extend this definition of the emittance to include both transverse directions using the idea of the covariance matrix. The normalized x emittance, up to a factor of 1/mc is equal to the square root of the determinant of the 2d, $x - p_x$, covariance matrix. Thus we can define the 4d normalized emittance as the square root of the 4d, $x - p_x - y - p_y$ covariance matrix multiplied by the same factor squared.

$$
\epsilon_{n,4d} = \frac{1}{(mc)^2}
\begin{vmatrix}
<x^2> & <xp_x> & <xy> & <xp_y> \\
<xp_x> & <p_x^2> & <yp_x> & <p_xp_y> \\
<xy> & <yp_x> & <y^2> & <yp_y> \\
<xp_y> & <p_xp_y> & <yp_y> & <p_y^2>
\end{vmatrix}^{1/2}
\tag{2.16}
$$

2.3.1 Non-Linear Emittance Growth

Emittance will not be a conserved quantity in the presence of non-linear forces. Fig. 2.7 shows the effect of a cubic force on the phase space of a beam. The phase space volume of the beam is conserved, however, the tails of the distribution are bent. In a calculation of the rms emittance, the linear $x - p_x$ correlation is subtracted from the beam, but the bent tails will result in inflated values of $< x^2 >$ and $< p_x^2 >$ compared to the beam before the cubic force was applied.
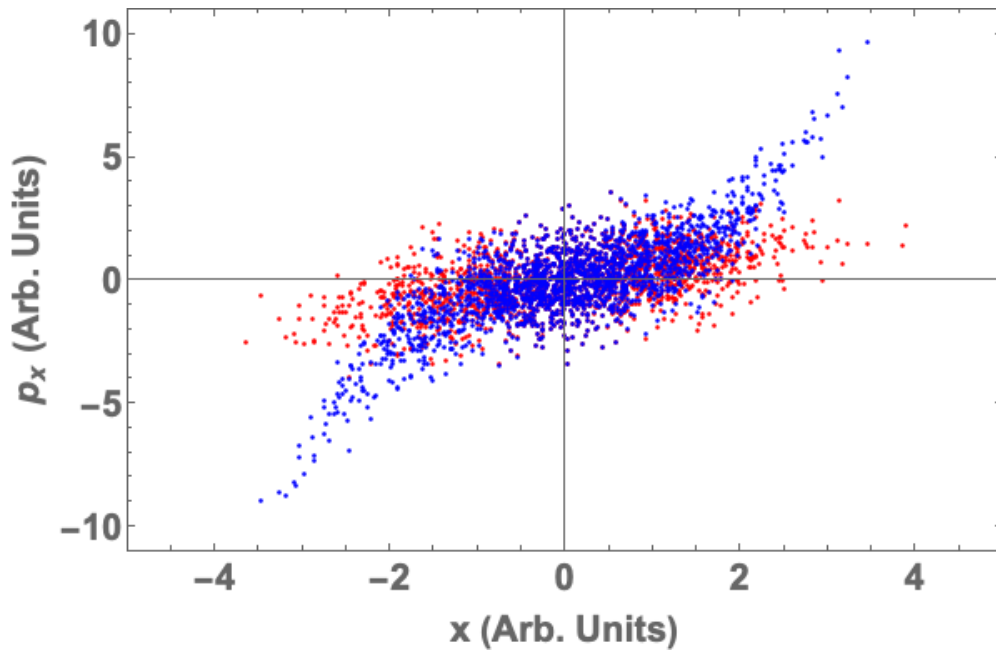
Figure 2.7: $x - p_x$ phase space of 2 fictitious electron beams. Each red dot represents the x-px phase space coordinate of a single electron and each blue dot represents its phase space coordinate after experiencing a cubic force.

The emittance growth from a sextupole will be used to illustrate this effect, and is depicted in figure 2.8. Assume a beam of particles with a Gaussian spatial distribution in x with standard deviation σ_x, with $y, p_x, p_y = 0$ for all particles and a longitudinal velocity v_z. The initial x emittance of this beam is 0 due to having 0 momentum spread. After going through a thin sextupole of length L, such that position coordinates do not change and the field of the sextupole is considered constant inside of it and 0 outside, the final momentum

of each particle using equation 2.5 is: $p_x = -GqLx^2$. Calculating the x emittance of this beam, one finds:

$$\epsilon_{n,x} = \sqrt{3}\frac{e}{mc}GL\sigma_x^3 \tag{2.17}$$
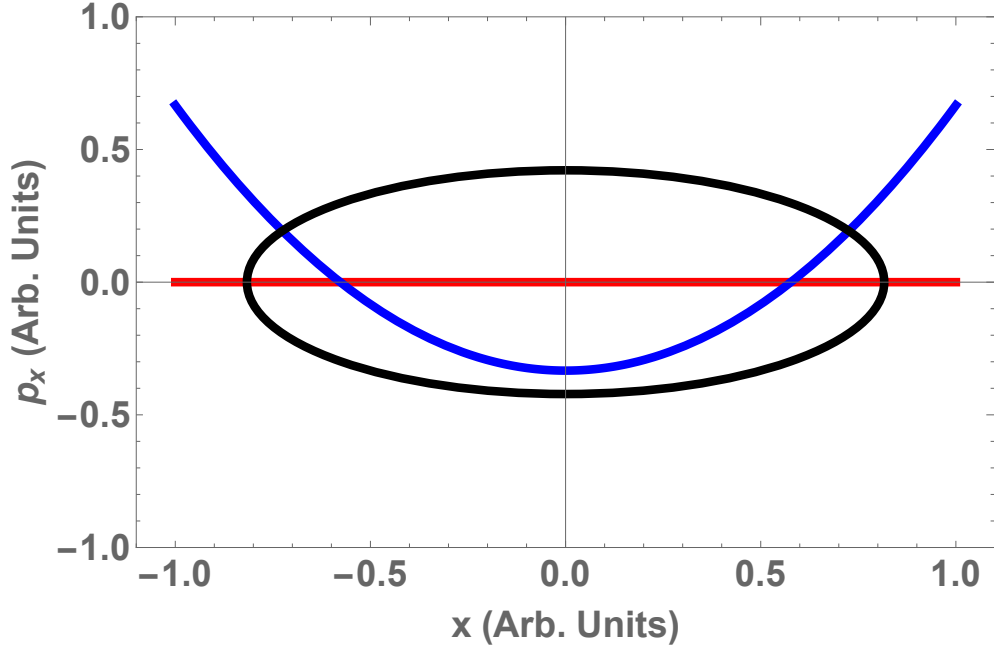
Figure 2.8: $x - p_x$ phase space of an electron beam with no initial momentum spread before (red) and after (blue) going through a sextupole. The ellipse in black has an area equal to the emittance of the beam after the sextupole times π.

The emittance of the beam from a sextupole grows as the size of the beam cubed [39]. This super-linear dependence on the beam size should be expected, as the quadratic force from the sextupole effects large values of x more than small values.

This increase in the emittance while artificial in construction, does effect the beam quality for several applications, thus is undesirable. Reversing the emittance growth of such a force is in theory simple. By acting on the beam with a compensating force, the tails of the beam can be unbent. Doing this for a sextupole nonlinearity in a real UED beamline will be the focus of chapter 4.

2.3.2 Longitudinal Correlations and Emittance Compensation

A typical source of transverse emittance growth in an accelerator comes from transverse-longitudinal correlations. Over the course of an accelerator, different longitudinal slices of a beam can obtain different $x - p_x$ correlations, depicted in fig. 2.9. While the emittance of each longitudinal slice of the beam may have remained constant over transport, the full beam emittance will have increased.
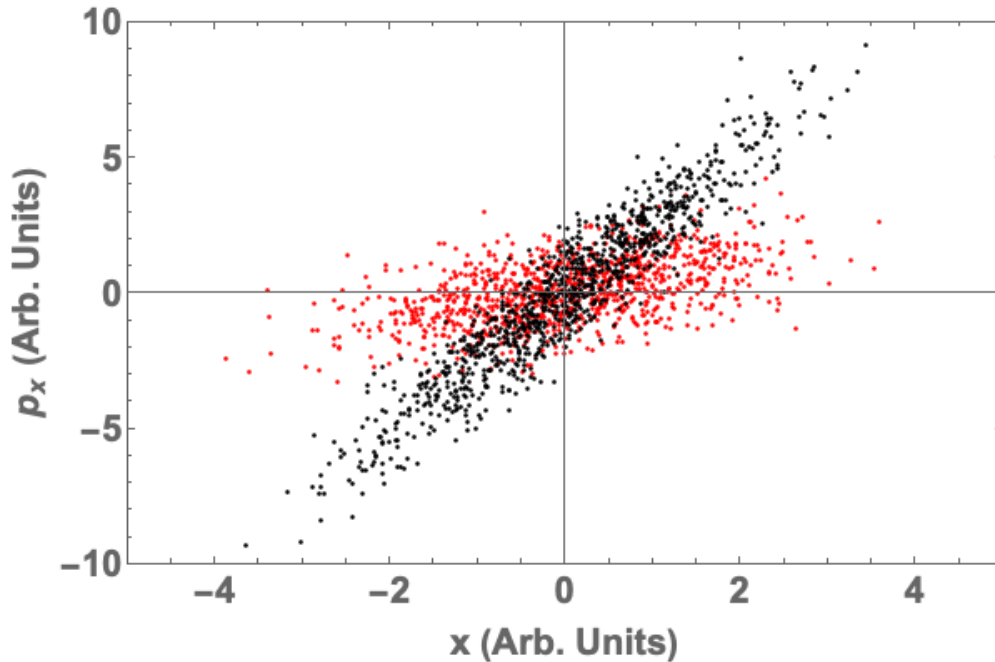
Figure 2.9: $x - p_x$ phase space of a single fictitious electron beams. Each red dot represents the x-px phase space coordinate of an electron from one longitudinal slice of the beam, while each black dot corresponds to a different longitudinal slice of the same beam.

Fixing this misalignment of longitudinal slices is known in the accelerator physics community as emittance compensation, a theory of which is described in [40]. In practice, optimizations of simulated beamlines are sometimes used to achieve this effect, as details of space charge and misalignment of optics in accelerators can add complications. This is discussed further in appendix B.

2.3.3 Density Diluting Effects

Effects discussed up to this point on the emittance have had no impact on the phase-space volume/density. However, some sources of emittance growth do have a direct relation to the reduction of phase space density, depicted in fig. 2.10.
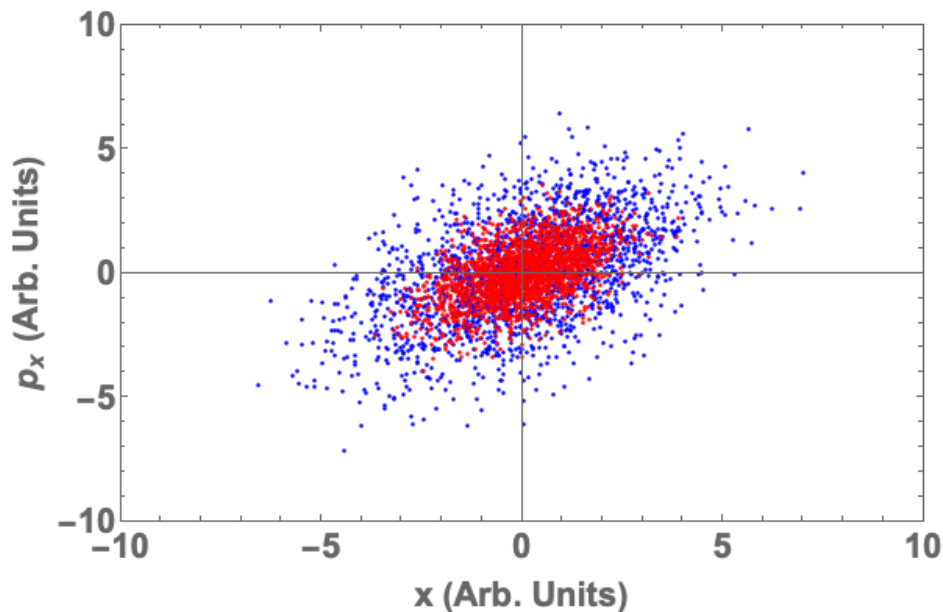
Figure 2.10: $x - p_x$ phase space of 2 fictitious electron beams. Each red dot represents the x-px phase space coordinate of a single electron and each blue dot represents its phase space coordinate after experiencing a density diluting force like an exact Coulomb force.

In particular, direct Coulomb interaction in a beam can decrease the phase space density. This effect from the Coulomb interaction is dependent on the temperature of the beam, with a colder beam, one with less momentum spread, being impacted more than that of a warmer electron beam.

2.3.4 Electron Source Quality

In short linear accelerators, the minimum emittance the electron beam can have is set by the electron source, and can only get worse in transit [41]. The size of the electron beam coming off of the cathode is determined by the size of the laser on the cathode surface. The

momentum spread of the electron beam off the cathode is dependent on the photoemission material and laser wavelength. The momentum spread is characterized by a quantity called the mean transverse energy (MTE), which is defined as:

$$\text{MTE} = \frac{1}{2}m_e < v_\perp^2 > \tag{2.18}$$

where m_e is the electron mass and $v_\perp$ is the velocity of an electron perpendicular to the cathode surface.

From the MTE the emittance of the beam coming from the photocathode, called the thermal emittance can be calculated as:

$$\epsilon_{n,x} = \sigma_x \sqrt{\frac{MTE}{mc^2}} \tag{2.19}$$

By reducing the MTE of the photocathode, the emittance of the resulting beam can thus be decreased. At small values of MTE, $<$ 20 meV, the mean field approximation of space charge breaks down for typical electron densities used in UED and XFELs. This will be the main focus of chapter 5.

2.3.5   Brightness

While emittance is an often used metric for beam quality, it alone is not enough to characterize an electron beam. UEM, which is typically run with an average of $<$ 1 electron per pulse often uses sharply tipped sources as they have much smaller emittance then flat photocathodes at the cost of charge [42]. However, this small number of electrons results in days of running the microscope in order to get a series of time-resolved images. In UED, diffraction and changes in diffraction patterns from a laser probe happen to a fraction of electrons on the scale of 10^{-4} [43], making single electron sources far less appealing.

An often more important metric then is the number of electrons that fit into a phase

space volume, or the phase space number density. This is often described through a quantity called the brightness. The 4d brightness is defined as:

$$B = \frac{1}{8\pi^2} \frac{I}{\epsilon_x \epsilon_y} \tag{2.20}$$

where I is the current of the electron beam. Depending on the application, the average or peak brightness of the electron beam will be a more useful metric. The average brightness uses the average current over many pulses. The peak brightness is defined using the peak current, defined as the charge of an electron pulse divided by its pulse length. For UED applications, the average brightness, along with the emittance, can be used to determine which features can be resolved, and how long it will take running the UED beamline to make those images.

CHAPTER 3

UED

UED is a pump-probe style experiment, depicted in figure 3.1. In a pump-probe experiment, the sample being studied is activated by a pump, which in UED is typically a fs scale laser pulse. This pump initiates dynamics which are then observed at a later time Δt by a probe, which in the case of UED, is a fs scale or smaller electron pulse. The observation is then recorded by a downstream detector. By repeating this process varying the delay between the pump and probe, it is possible to observe the sample at different times during its dynamics. By compiling these observations together, a full description of the dynamics of a system can be made [44].
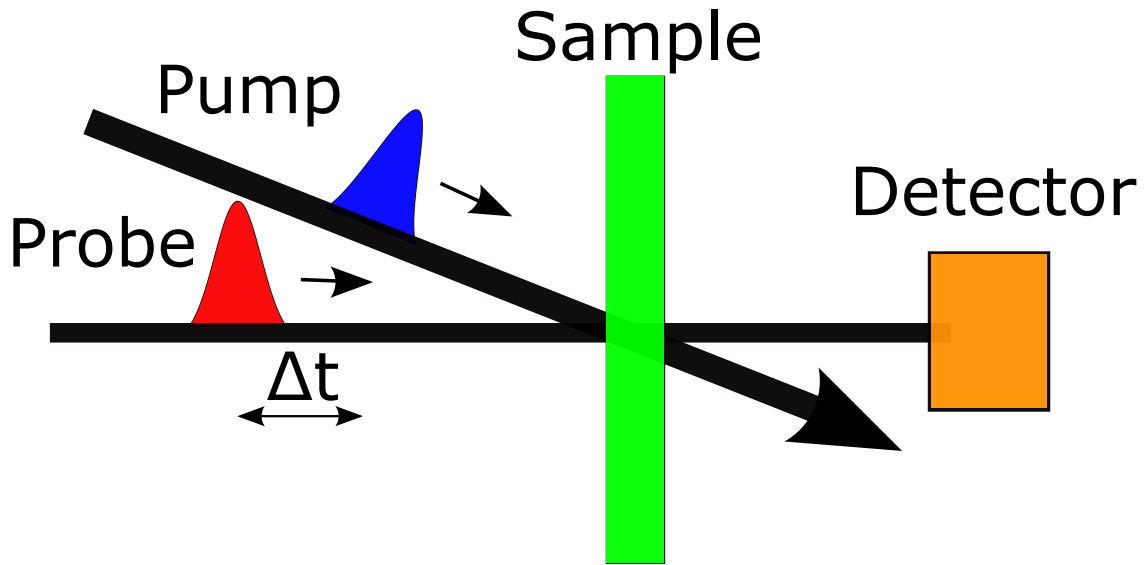
Figure 3.1: Depiction of a pump-probe experiment. A pump laser pulse excites dynamics in a sample. A short time later, Δt, a probe pulse/beam, of electrons in UED, interacts with the sample, recording the dynamics at that time delay.

The time delay between the pump and the probe can be controlled by changing the path length of the pump laser. Typically this is done as the probe electron beam is often compressed through RF cavities, so changing the arrival time of the probe electron beam would require a simultaneous change of the RF phase, which is more challenging with no

benefit in many setups. The pump laser path length can be changed through the use of a motorized mirror which sends the incoming laser in the opposite direction of incidence, with a transverse displacement, see fig. 3.2. A displacement of this mirror by 150 μm changes the delay of the pump laser by about 1 ps, allowing for fs level control with a motor with micron precision in the motor control.
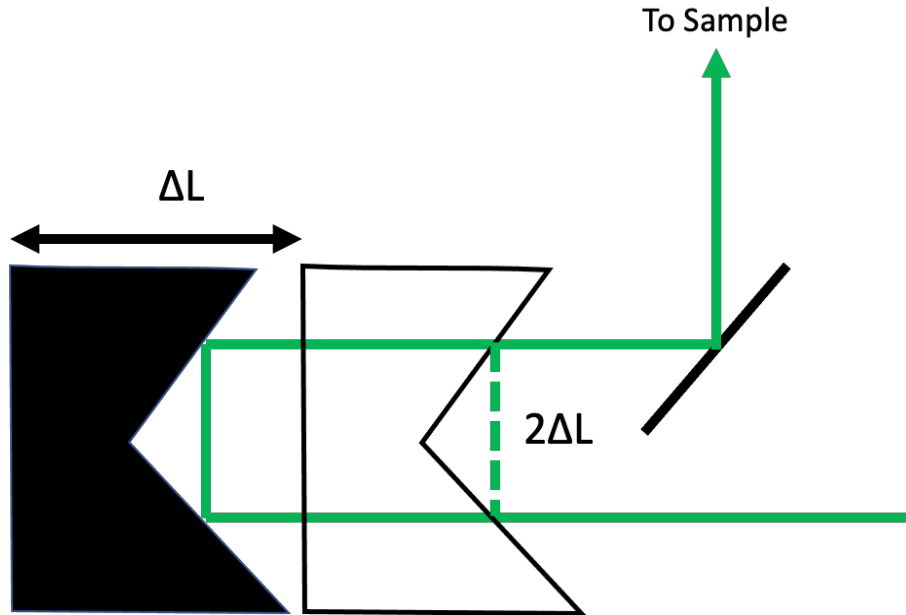
Figure 3.2: Schematic of changing the pump probe arrival time difference by changing the path length of the probe laser. A displacement of a mirror by ΔL cause a change in the laser path length by $2\Delta L$

3.1   Synchronization

One of the issues in preforming a pump-probe experiment involves the synchronization of the pump and the probe. In order to know how long after the laser pulse the electron beam hit the sample, you need to know the laser path length at which the electron beam and the pump laser hit the sample at the same time.

One method of doing this synchronization involves the use of a copper transmission electron microscopy (TEM) grid, see fig. 3.3. By shining the pump laser onto this grid it

will photoemit electrons in a cloud. The electron beam will then interact with this cloud and get a slight deflection in its trajectory. By changing the delay of the pump laser compared to the electron beam, it is then possible to find the time at which the deflection from the cloud just begins, which is the onset of the formation of the cloud, thus synchronizing the electron beam and pump laser [45].
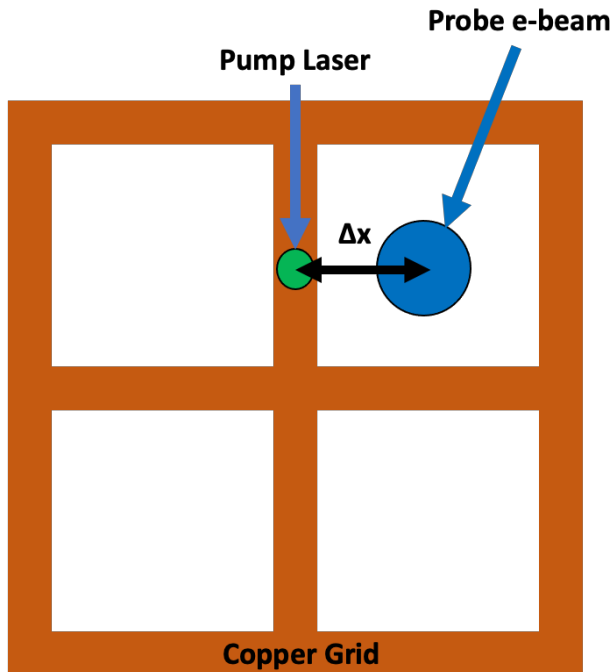
Figure 3.3: Schematic of pump-probe synchronization using a copper TEM grid. A pump laser hits the copper grid, creating an electron cloud at the location of the laser. This cloud then deflects the probe electron beam which is at a distance Δx away

An additional complication in this method occurs when the electron beam does not overlap the electron cloud spatially. What is seen is that the temporal location of the peak in the deflection is dependent on how far the electron beam is away from pump laser, see fig. 3.4. If we were to treat the electron cloud as a free ball of electrons, this result makes no sense. The electron cloud should appear as a point charge to the electron beam at any arbitrary distance outside of the cloud.

This time delay can be explained from the inclusion of image charge forces, to show
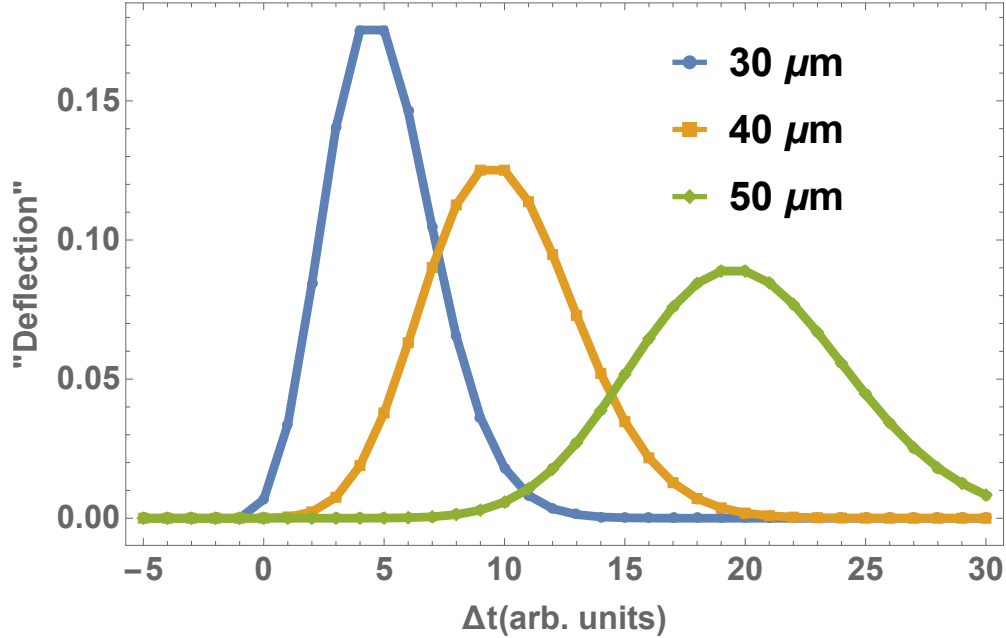
Figure 3.4: Idealized depiction of the momentum deflection using the copper grid TEM for different pump delays, Δt between the pump electron beam and probe laser. For larger distances between the electron beam and the electron cloud, the peak of the deflection moves to higher Δt.

this, I used the following semi-analytic method. I simulated an electron cloud expanding at a velocity expected from similar experiments. At several different snapshots in time, I recorded the positions of all of the electrons in the cloud. I treat the electron cloud as static charges at each snapshot recorded, as the electron beam passing it is moving almost the speed of light, so on the time scale of the beam passing the cloud, the cloud does not move much. I then analytically calculated the momentum kick on the beam from an electron (as well as the kick from the dipole made with its image charge), an arbitrary distance away from the beam on a path from infinity to the image plane. It is assumed that this momentum kick is small, and thus does not significantly impact the trajectory of the beam. By then summing up the effect of this with the positions recorded at different times in the electron clouds time evolution, the momentum kick at different coincidence times and beam positions can be calculated.

The resulting momentum kick from the dipole force as a function of time delay is shown
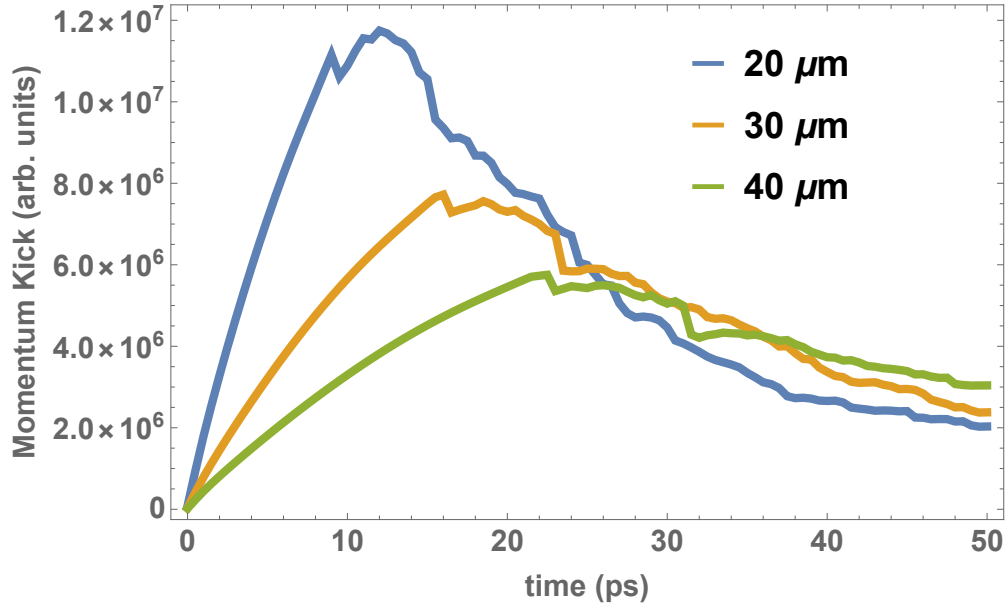
Figure 3.5: Model of deflection strength vs. time of arrival of electron beam at different distances away from an electron cloud.

in fig. 3.5. The behavior of the delayed peak in the deflection magnitude is clear and explains the observed effect.

3.2   Diffraction

A well known property of quantum mechanics is wave-particle duality, in which all particles and quantum objects can be described as both particles and waves [46]. So not only must we consider our electron beam as a collection of particles, but as a collection of delocalized waves.

When a wave passes around the corners of an obstacle or through an opening, it is bent or distorted around it. The effects of this are more noticeable when the size of the obstacle or aperture are not large compared to the wavelength of the wave. This collection of effects is known as diffraction which is talked about in most textbooks on the properties of waves such as [47].

The diffraction phenomenon of interest to UED is the effect of a wave traveling through

a lattice. The difference in the incoming and outgoing wavevectors, $\Delta \vec{k}$ of a wave in a lattice undergoing elastic scattering must be a linear combination of the reciprocal lattice vectors, known as Laue's equations. Simplifying to one dimension, and using a lattice with lattice constant L, this condition is:

$$\Delta k L = 2\pi n \tag{3.1}$$

where n is an integer [48]. The lowest magnitude non-zero change in wavevector has $n = \pm 1$. Using $k = 2\pi p/h$ for a free particle, where h is Planck's constant, the minimum change of momentum for a free particle going through the lattice is:

$$\Delta p = \frac{h}{L} \tag{3.2}$$

3.2.1   Coherence Length

For diffraction to be observed in a lattice, the momentum kick in a direction, using x as an example, from the lattice needs to be larger than the momentum spread, σ_{p_x}, of the beam. If it is not, the spread of electrons of a single peak on a detector will overlap neighboring peaks.

Setting σ_{p_x} to be greater than the momentum kick described in equation 3.2 and solving for the lattice spacing L:

$$L < \frac{h}{\sigma_{p_x}} \tag{3.3}$$

This expression gives the maximum lattice spacing that an electron beam will be able to resolve the diffraction pattern for, and is often referred to as the transverse coherence length. This equation can be rewritten in terms of the emittance at a beam waist, $< x p_x >= 0$ using equation 2.15:

$$L < \frac{h}{mc} \frac{\sigma_x}{\epsilon_{n,x}} \tag{3.4}$$

33

This expression for the coherence length is useful because in UED, the necessary coherence length is set by the sample, and with a conserved emittance, this determines the size that the electron beam, and thus the sample needs to be bigger than in order to do diffraction experiments.

3.3   Mitigating Space Charge

Using electrons for time-resolved diffraction involves a dense beam of electrons, short both longitudinally and transversely. The Coulomb force directly fights against this, and in a dense beam can irreversibly ruin the emittance and thus coherence length of the electron beam.

Several methods have been used in order to mitigate the effects of space charge in UED. Decreasing the charge emitted from the cathode can work, but results in more repeated measurements to be taken to get a complete and noise resolved diffraction image. Shaping of the electron beam can be done to make the space charge force mostly linear [49]. Increasing the energy of the beam has also been done, which as shown in equation 2.14, can relativistically suppress the Coulomb interaction [13]. Decreasing the propagation distance between the cathode and the sample location to the order of cm has been used to minimize the time space charge forces can distort the beam. Another method involves starting with an electron beam which is longitudinally long, and using an RF cavity to bring the beam to a longitudinal focus at the sample location, reducing the time in which space charge forces are large [8].

For systems that use rf bunching cavities, the size of the electron beam alone is not the only thing which determines the temporal resolution of a UED beamline. Additionally in these cases, the jitter in the phase of the RF cavity will cause some bunches to arrive earlier

or later than others. This uncertainty in the arrival time of the bunch adds in quadrature:

$$\sigma_t^2 = \sigma_{t_{bunch}}^2 + \sigma_{t_{jitter}}^2 \tag{3.5}$$

where $\sigma_{t_{bunch}}$ is the size of the electron bunch and $\sigma_{t_{jitter}}$ is the size of the temporal of a single electron due to RF phase jitter. Thus the achievement of high temporal resolution through compression methods is limited to the quality of the RF electronics, and is not a complete solution to the mitigation of space charge.

CHAPTER 4

STRAY-FIELD CORRECTION IN UED BEAMLINES

This chapter is a modified version of this work [50]. The work is based on removing stray magnetic fields from a UED beamline at Cornell depicted in fig. 4.1, from [43].

Legend:
1. Cathode transfer system
2. 200 kV dc gun
3. Focusing solenoid
4. 3GHz rf buncher
5. Sample chamber
6. Detector
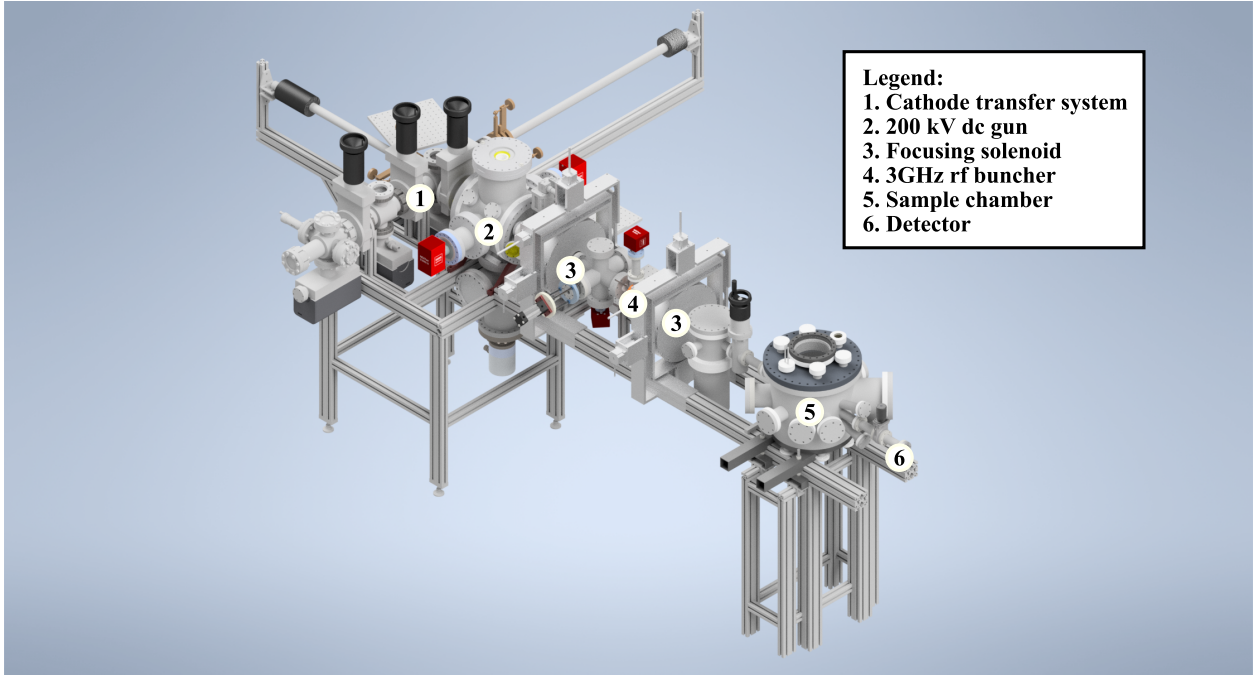
Figure 4.1: A schematic of the MEDUSA ultrafast electron diffraction beamline.

4.1 Stray Fields in UED

Doing diffraction on samples the scale of microns, often called micro-diffraction, is necessary for some materials, as creating crystalline structures of these materials at larger scales can be impractical [51, 52]. For these experiments, the electron probe must be smaller than the sample being measured. During emission, where the electrons start nearly at rest, space charge forces will cause a small electron beam to grow quickly. Attempting to keep the beam small throughout the entire beamline results in non-linear space charge forces diluting the final emittance of the beam. So the electron beam must either start at a large size or

become large over its transport. Then to achieve a small electron beam size at the sample, an electron beam can be focused by a solenoid close to the sample location. A bigger beam size in the focusing lens results in a smaller size at the beam waist. Therefore, doing micro-diffraction results in large beam sizes in optical elements, meaning non-linear fields like those from sextupoles become more important to control.

Quadrupole stray fields in or prior to solenoids couple the transverse phase spaces and dilute the two dimensional emittances. The successful correction of these stray quadrupole fields in solenoid magnets and from rf couplers in photoelectron guns has been well studied and demonstrated with downstream correction quadrupoles [53, 54, 55, 56, 57]. Previously, sextupole aberrations in solenoid magnets and their correction have been considered theoretically and in simulation, and it was found that a similar correction procedure with a downstream sextupole corrector magnet would be successful [39].

In this chapter, I show that the MEDUSA beamline's emittance is sensitive to aberrations up to sextupole order, and describe in detail the correction procedure. To our knowledge, this is the first experimental demonstration of stray sextupole correction in a photoinjector. To diagnose aberrations and beam brightness, we employ a 4-dimensional transverse phase space mapping system with sub-nm emittance resolution. We then describe the brightness performance of the device with rf-compressed bunches containing up to 10^5 electrons, and show that the measured emittances are in good agreement with aberration-free space charge simulations.

4.2   Designing and Building a Sextupole Corrector

To fix a stray sextupole moment effecting the beam there are two ways to go about fixing it. The first method involves finding the source of the sextupole field and removing it. For example, by removing the source of asymmetry in an RF cavity or solenoid, the stray field sextupole can be removed [58, 59]. However, this method can be difficult to achieve

practically, as first, it is necessary to locate the exact cause of the sextupole field. Once it is found, then it needs to be fixed, and there are limitations to how perfectly something can be machined and aligned. The second method involves the insertion of a designed sextupole magnet whose field will undo the effects of the stray sextupole on the beam. This designed sextupole magnet for the purpose of removing stray sextupole fields is called a sextupole corrector.

A sextupole corrector has different constraints on it, depending on the beamline it is used in. In circular accelerators, where the charged beam will pass through the same set of magnets several times, the position of the sextupole magnet in the beamline is important, as small errors have the opportunity to build through multiple passes. For linear accelerators however, sextupole correction can be done as long as the sextupole corrector is placed where size of the beam in its transverse oscillations is near that where the sextupole originated. An example of this in simulation is shown in section 4.6.

The first step in designing a sextupole corrector is the electromagnetic design. I did the electromagnetic design of the sextupole corrector using the three-dimensional magnetostatics code, RADIA [60]. The goal of this electromagnetic design was to create the sextupole corrector with dimensions that could fit on the few inches of beam pipe that were available, with a sextupole field large enough to cancel the observed effect while running at a low enough current that the sextupole would not require additional cooling.

I composed the sextupole in RADIA with 6 thick solenoids with current flowing in the ϕ direction in local cylindrical coordinates, see figure 4.2. Neighboring tubes having opposing current directions to flip the polarity of the polarity of neighboring poles. The radial and longitudinal sizes of the solenoids, the thickness of the solenoids, and the distance of the solenoids from the origin are variables to be determined in the design.

The solenoid size was determined by constraints of fitting the corrector on the beamline. The height of the solenoid was chosen to be 25 mm. The inner solenoid radius was chosen
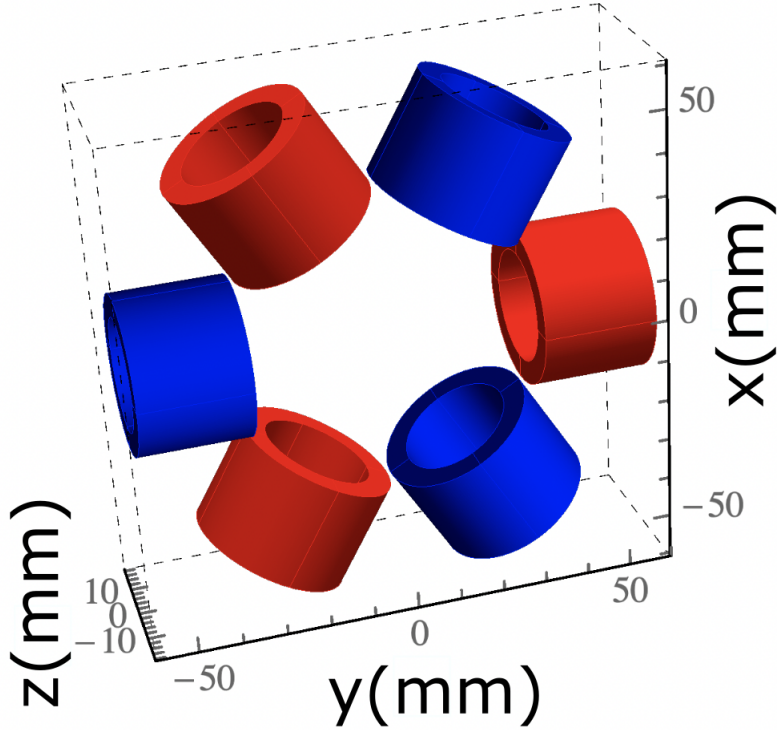
Figure 4.2: RADIA implementation of the sextupole corrector. Red represents magnetic field pointing towards the origin from a given tube and blue represents magnetic field pointing away from the origin.

to be 25 mm. The outer solenoid radius is determined by the distance of the solenoid to the solenoid to the origin, such that the solenoids are barely not touching.

The distance of each solenoid from the origin was then optimized, with a minimum distance set at 25 mm by the minimum outer solenoid radius, which is the inner solenoid radius. The maximum current density that magnet wire, which will be used to wind the solenoid, can have running through it without cooling is conservatively estimated to be under $2.5 \ \text{A/mm}^2$. For multiple choices of distance from the origin the current necessary to produce a sextupole large enough to cancel the observed sextupole field were found.

In order to find the sextupole strength necessary to cancel out the moment in the beam-line, the difference in emittance between the measured beam and a simulation of the beam-line were used. Using equation 2.17, the emittance growth is proportional to the sextupoles strength multiplied by its length. The length in this equation assumed a constant field

39

strength over a length L with 0 field outside, which is not true for this sextupole, so an effective length must be found.

The effective length of the solenoid was found as follows. A field profile, B_y was found for different longitudinal positions from the center of the sextupole, see fig. 4.3. By integrating the normalized field, I find that the effective length of the solenoid with a constant magnetic field equal to its value at z=0 value to be about 41 cm.
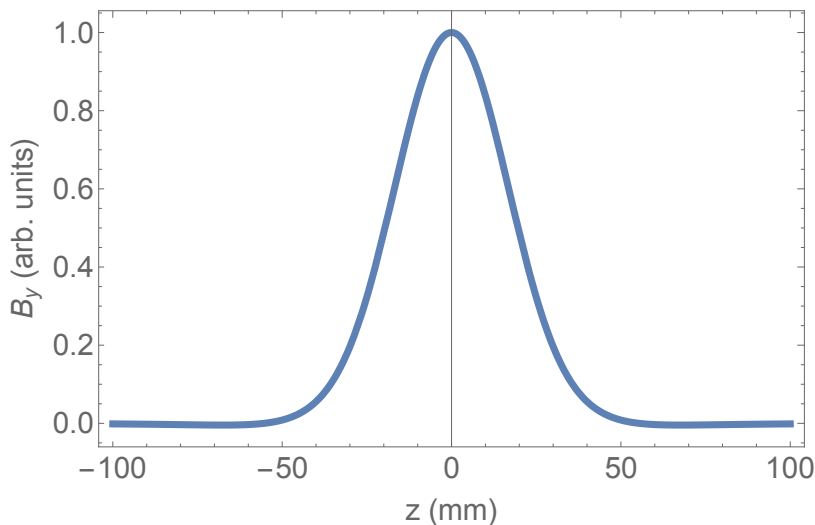
Figure 4.3: Magnetic field in y-direction as a function of longitudinal position from the center of the sextupole. A small transverse offset was used such that the field is non-zero.

With this effective length, the necessary current density of the magnet wire can then be found. The sextupole strength G at $z = 0$ is found by doing a quadratic fit of B_y vs x^2 and y^2 and taking an average. The strength G then varies with the current density in the wire, so the necessary current density was found and plotted as a function of the solenoid distance from the origin, shown in fig. 4.4. The shape of the plot can be understood as follows. For small radii, the outer radius limits to the inner radius, making the total volume where current is flowing equal to 0, requiring a diverging current density at 25 mm. For large distances, the extra volume from increasing the size of the solenoid is at a cost of moving the solenoid farther from the beam axis, resulting in a a higher current density needed for the same field near the origin.
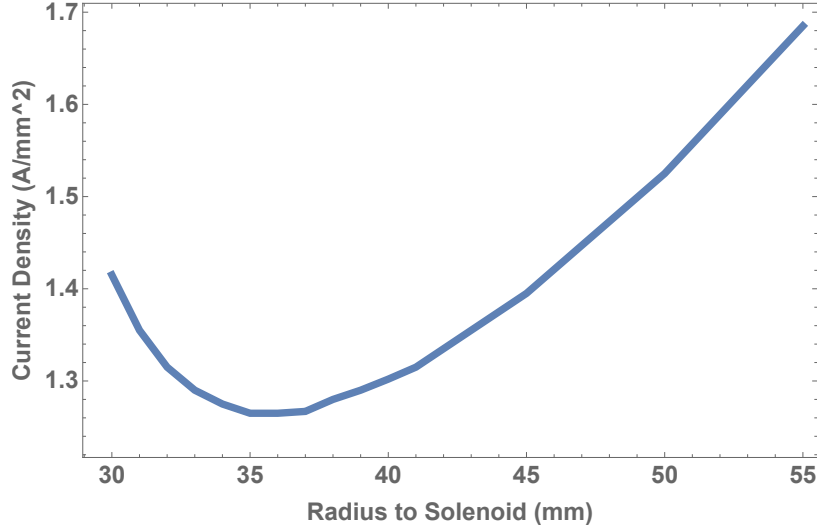
Figure 4.4: Current density needed in the magnet wire as a function of radius to the the inner edge of the solenoid.

As an additional complication, this calculation assumed that the current density would be constant throughout the solenoid, which is not true. The solenoid will be composed of wound circular magnet wire. It is not possible to fill the entirety of the volume inside of the tube with this wire. Instead, this problem can be thought of as the packing of circles in a plane, see fig. 4.5 from [61]. The maximum you can fill the solenoid depends on the lattice structure of the wire. For example hexagonal packing has a packing fraction of about 90.7%, the highest of any packing scheme. Square packing has a lower fill fraction of 78.5%. My winding is in between these with a packing efficiency of about 81%. Thus the current density needed has an additional multiplier of 1/.81.

Even with the packing efficiency included, the maximum current density of 2.5 A/mm^2 is well above the range of values explored. To allow the solenoid design to be additionally used for applications outside of the sextupole, a final distance from the solenoid to the origin of 50 mm was chosen.

After the electromagnetic design was finished, a mount was needed to secure the sextupole together, and hold it to the beamline. I designed the mount in Autodesk Inventor, see fig. 4.6. The mount consists of a 2 part aluminum core, 6 aluminum solenoid winding mounts, 4

41

square packing   hexagonal packing
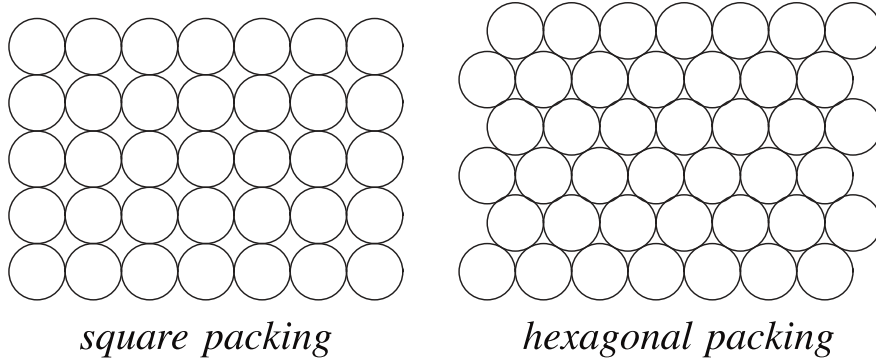
Figure 4.5: 2d packing of circles in a plane, representative of the winding of wires in a solenoid.

aluminum straps to hold the core together, and 4 aluminum clamps to secure the sextupole corrector to the beamline. The parts are held together by 314 steel screws. All materials were chosen such that the mount was non-magnetic such that it did not produce stray-fields of its own.

After design, the mount was fabricated in the Cornell Newman Lab machine shop. I assembled the parts and with the help of M. Kaemingk, wound the 6 solenoids with 1000 ± 3 turns of 24 gauge magnet wire. A final image of the constructed solenoid is shown in fig. 4.7

4.3   MEDUSA Beamline

The experiments presented in this chapter were conducted in the MEDUSA ultrafast electron diffraction beamline [43]. A schematic is shown in fig. 4.8. The electron beam is produced by the photoemission of a Na-K-Sb photocathode using a red (650 nm) laser pulse with a full width at half max of 10 ps. At this wavelength the MTE of the photocathode is expected to be below 50 meV.

The main operating mode the MEDUSA beamline was designed for is ultrafast electron micro-diffraction, with final rms probe sizes on the order of a few microns using a 10 micron probe defining aperture. In order to obtain a sufficient charge on target, typically a few hundred electrons, the beam must come to a tight focus at the aperture.
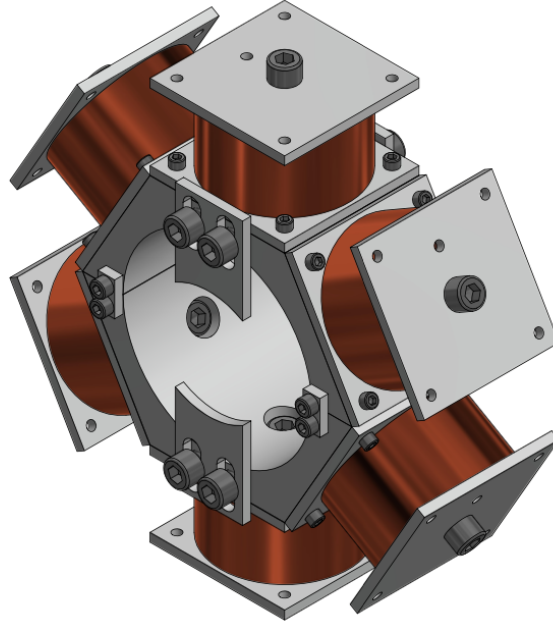
Figure 4.6: Assembly of sextupole mount components created in Autodesk Inventor. Copper color is representative of the magnet wire and is not included in the mount.

In this operating mode, to achieve maximal transmission through the aperture, the first solenoid is set to 0 current. When this is done, for bunch charges on the scale of tens of fC, the beam grows to the size of the buncher aperture, approximately 1.5 mm in diameter, before reaching the buncher. Thus, the buncher acts as a collimator, clipping large angle charge far from the beam center. This however makes the beam sensitive to stray fields from the buncher. Despite this, through the use of quadrupole and sextupole correctors, we are able to simultaneously achieve high transmission and small emittance at the sample location.

4.4 4D Phase Space Reconstruction

To show the preservation of beam quality throughout the beamline, a measurement of the 4 dimensional transverse phase space is done at the location where UED samples are measured. At the sample location, a 10 μm pinhole was placed. By focusing the beam at the pinhole location, scanning the beam across the pinhole using corrector magnets, and recording the
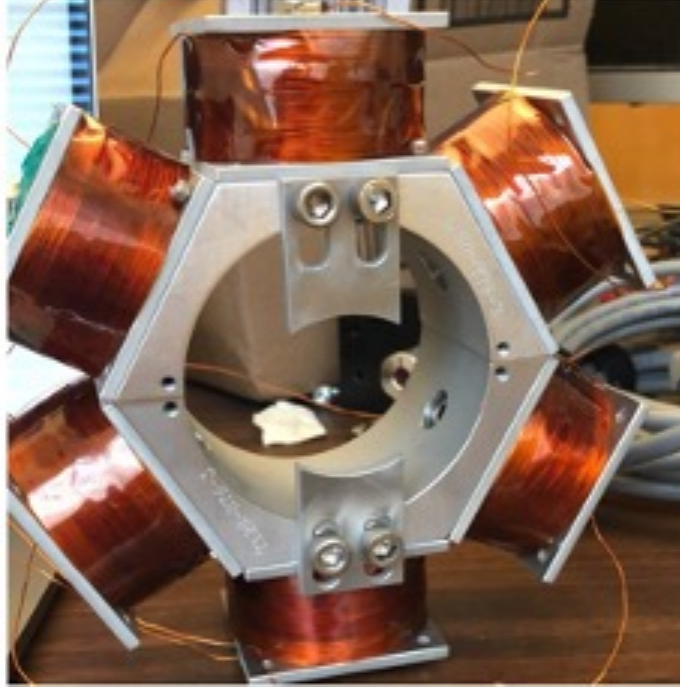
Figure 4.7: Image of the sextupole corrector after fabrication and winding.

resulting clipped beam at a down stream detector, 4D transverse phase space information can be reconstructed. Measurements were done taking 13 μm steps and the angle resolution, determined by the camera pixel size and drift distance between the pinhole and the downstream YAG, is approximately 40 μrad.

With this 4D density matrix information, the 4D beam matrix can be calculated as described in section 2.3 To be comparable to 2D measurements of emittance, when values of the beam emittance are presented in this chapter, the square root of the 4D emittance will be shown.

In figs. 4.9a, 4.9b and 4.9c, the beams real space, $x - p_y$ space, and x phase space are shown respectively, which is done by integrating the 4D density matrix along the unused axes. This is done with an emitted charge of 10 fC with 8 fC of charge making it to the pinhole with a buncher voltage around 3.5 kV. The dashed white line in fig. 4.9b shows the correlation between x and p_y which is seen to be negligible, which is the result of skew quadrupole correction in the beamline.
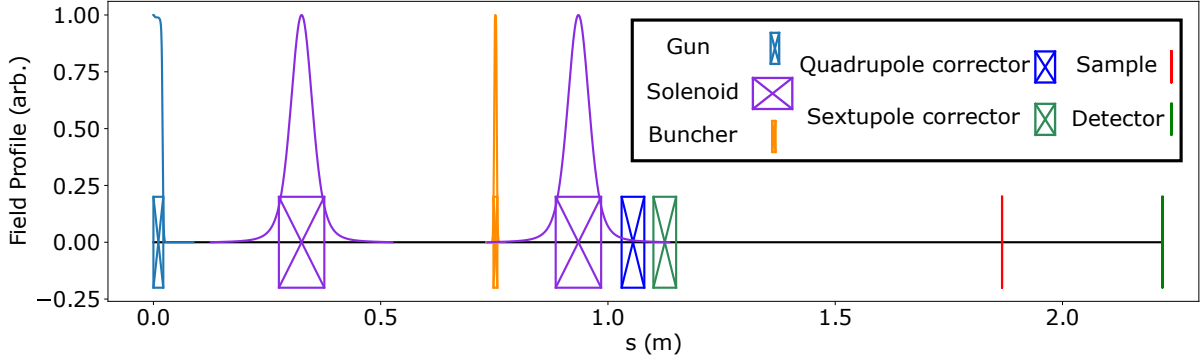
Figure 4.8: Field profile of the MEDUSA ultrafast electron diffraction beamline. The longitudinal field of the gun, solenoids, and buncher are shown, as well as the location of relevant beamline elements. Of particular note are the quadrupole and sextupole correctors, located immediately after the second solenoid. The emittances and phase spaces measured in this chapter are measured at the sample location.

Calculated values of size and emittance are done using a 90% charge threshold on the 4d density matrix. This threshold was chosen to remove the contribution to calculated values from the background noise, which was seen to dominate below 10% of the peak density value.

4.5   Quadrupole and Skew Quad Correction

In the MEDUSA beamline, the primary source of stray quadrupole moments arises from the two solenoids. The construction method used for the solenoids precluded perfect cylindrical symmetry, allowing quadrupole moments to develop.

Fig. 4.10 shows the effects of these solenoid quadrupole moments on the transverse beam profile. Two effects are immediately apparent: the asymmetry in beam size, particularly near the positive focus, and a significant tilt angle. Using General Particle Tracer (GPT), a particle tracking PIC code, we are able to fit for the initial beam parameters and the stray quadrupole moments. We find that the data is well fitted by modeling two components to the stray quadrupoles moments in each solenoid: a component that scales with solenoid

45
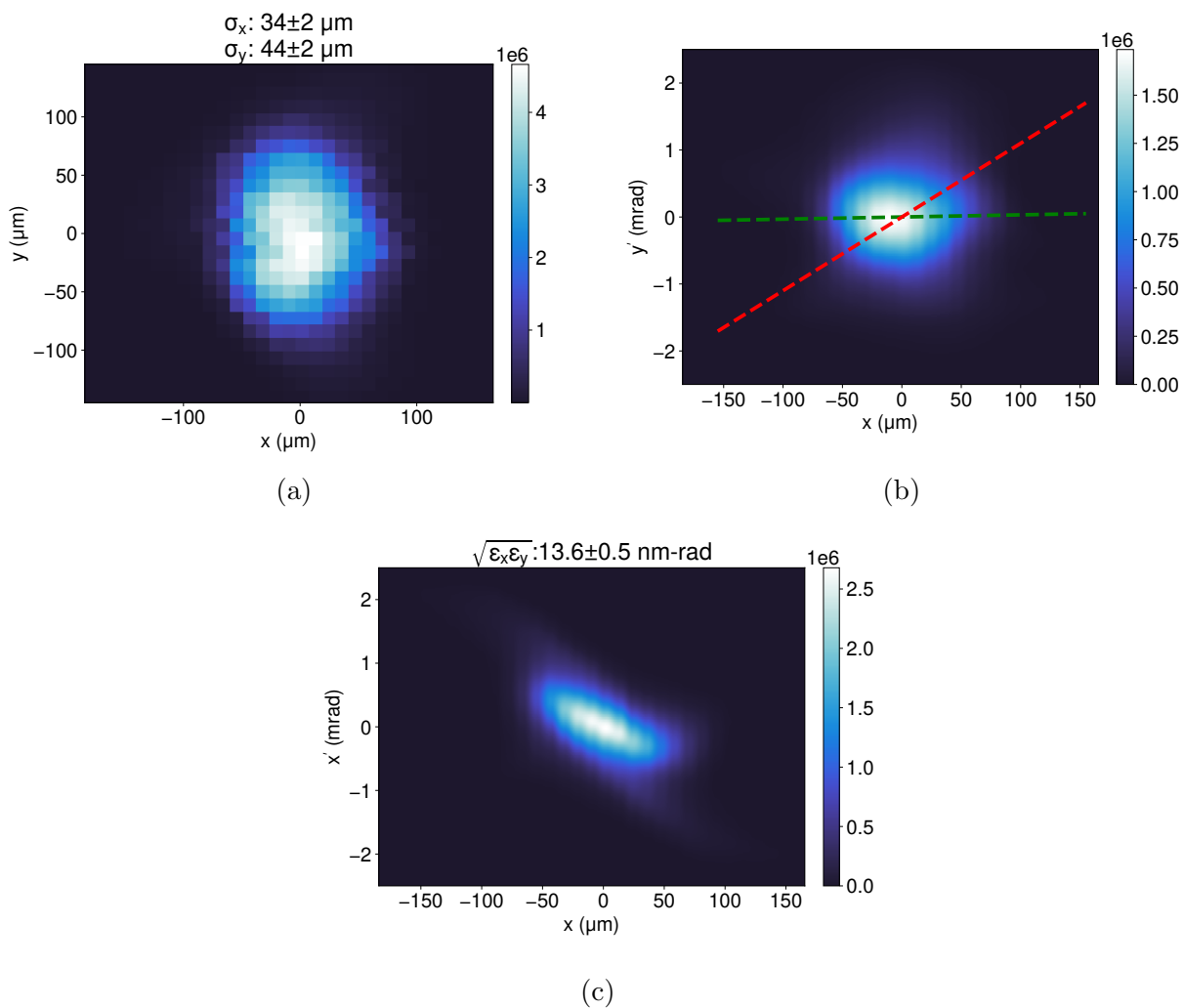
Figure 4.9: (a) x-y, (b) x-p_y, and (c) x-p_x projections of the reconstructed 4d density matrix at the sample location with sextupole correction. The dashed line in (b) shows the correlation between x and p_y which is seen to be near 0.

field strength and a constant component arising from hysteresis in the iron yoke. Both are oriented as normal quadrupoles. The anticipated effects of these quadrupole moments on final beam quality can be seen in Fig. 4.11. Starting with beam settings optimized for maximum transmission through the 10 micron probe-defining aperture (530 electrons, 8.6 nm-rad emittance), the stray quadrupole moments obtained by the fits in Fig. 4.10 were introduced in simulation. A global scale factor was applied to the stray quadrupole moments of both solenoids, so that the dependence of emittance and transmission could be determined.

The emittance increases roughly linearly with the stray quadrupole strength, while the transmission drops sharply before leveling off. At the fitted strengths, the emittance has increased to 41 nm-rad, approximately a factor of 4, while the transmission has dropped to a mere 27 electrons, nearly a factor of 20.

Dowell has shown in an analytic treatment that these drastic effects on beam quality can be mitigated with tunable quadrupole correctors [55] and that the only necessary consideration for the locations of the quadrupole correctors is that they have more effect where the beam is large. As seen in Fig. 4.9a, we put a normal and skew quadrupole corrector immediately after the second solenoid, where the beam is large. With the correctors in place, we were able to measure transmissions consistent with our simulations.

4.6 Sextupole Correction

After quadrupole correction, the beam shape is triangular on the detector. The triangular shape is strong evidence of a stray sextupole field in the beamline. The source of this sextupole field is the bunching cavity, which is asymmetrically coupled to power at its top. To correct for this sextupole moment, a designed sextupole magnet is placed just after the second solenoid, and rotated to produce an opposing sextupole moment.

Using a downstream sextupole corrector to correct emittance growth from a sextupole in a linear accelerator has been studied previously in simulation [39]. Simulations of the
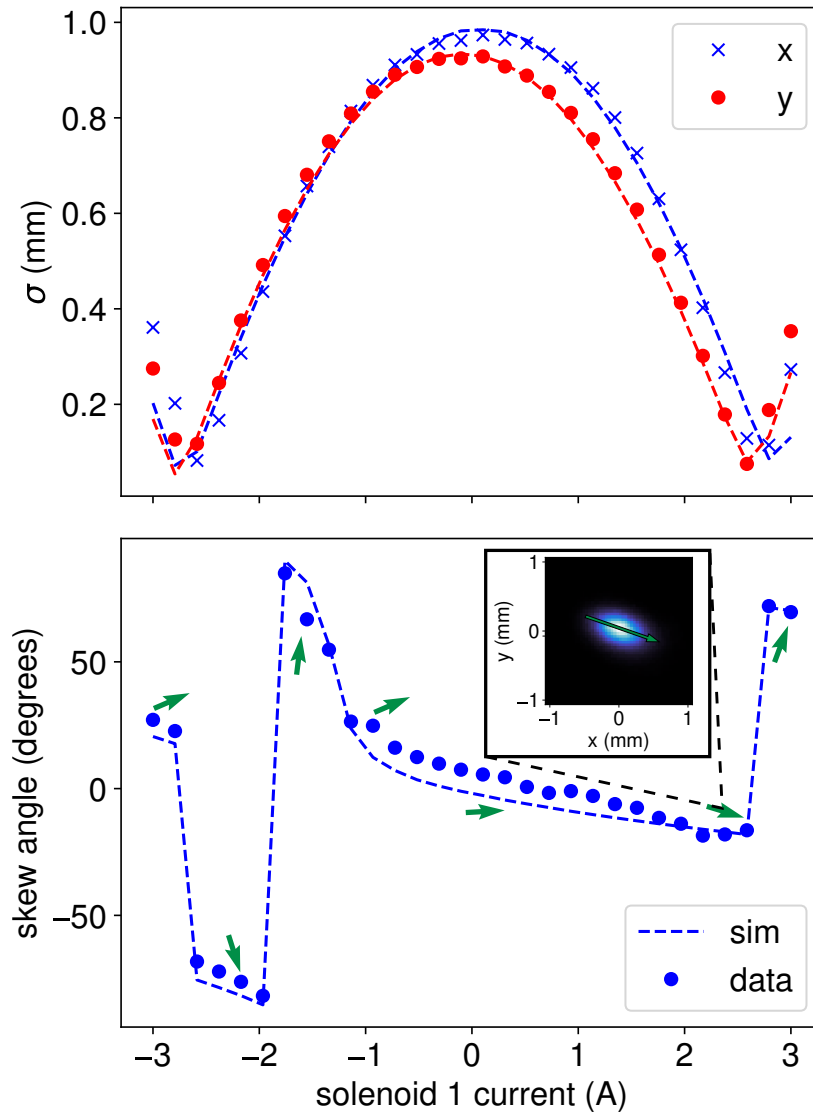
Figure 4.10: An example of the effects of the stray quadrupole moments on the (a) beam size and (b) beam shape. The beam shape is quantified with the skew angle of the beam profile. The green arrows provide a visualization of the directions associated with the skew angles. The dashed lines represent fits done with GPT and show good agreement with the experimental data. Inset: Example of a beam with an evident skew.
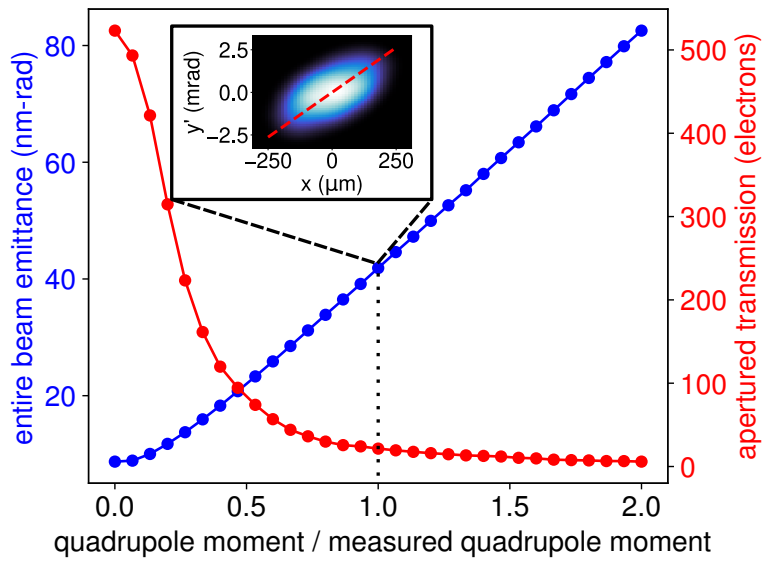
Figure 4.11: A simulated example of the effects of the stray quadrupole moments on entire beam emittance (blue) and transmission through the final aperture (red). The stray quadrupole moments found by the fits in Fig. 4.10 were scaled by a global factor, shown on the x axis, to show the dependence on their strengths. Inset: The x-p_y phase space at the nominal quadrupole moments. A clear correlation, highlighted by the red dashed line, can be seen. Contrast this to the nearly zero correlation in the x-p_y phase space of Fig. 4.9b, represented by the green dashed line.

beamline were done putting a sextupole in the buncher and tuning its strength to match the measured emittance. A second sextupole was then placed after the second solenoid. In fig. 4.12, the simulated emittance of the beam at the sample location is plotted against a varying sextupole corrector angle. It is shown that an appropriate choice of strength and angle in the second sextupole corrects the majority of the emittance growth from the buncher sextupole.
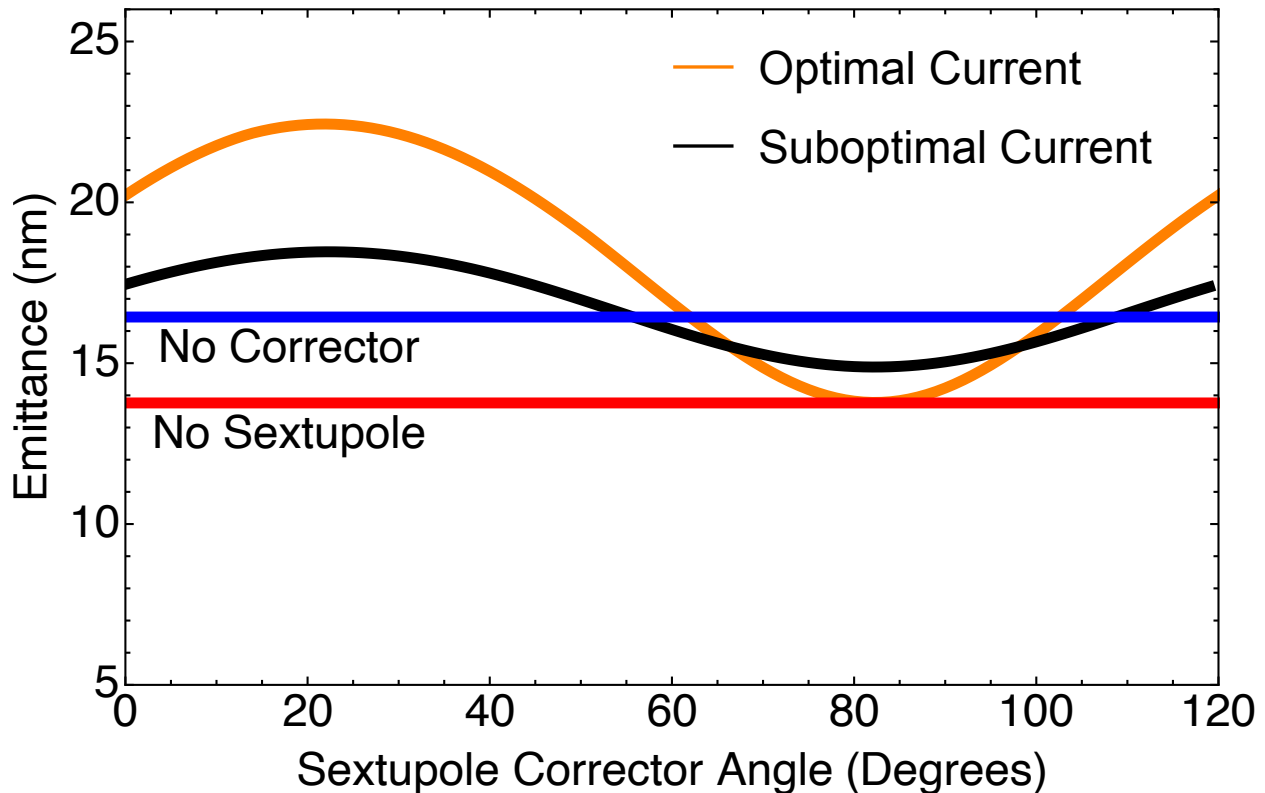
Figure 4.12: Simulated emittance at the sample location varying the angle of a sextupole corrector placed after the second solenoid. The red horizontal line is the emittance of the beamline with no sextupoles included. The blue horizontal line is the emittance of the beamline with a sextupole in the buncher and no corrector. The orange and black curves show the resulting emittance for a corrector current which best cancels the sextupole moment and is half of the needed current respectively.

The emittance growth cancellation is not exact, as the correcting field does not overlap the stray field. The dependence of the emittance calculation on the sextupole corrector position was found by optimizing the corrector angle and strength at different positions along the beamline, as shown in figure 4.13. Exact emittance growth cancellation is shown

to only occur exactly at the buncher location where the stray field originates. However, away from the beam focus, the uncorrected emittance contribution from the sextupole stray field is seen to be under 1 nm, close to .5 nm at the actual corrector position, which is sufficient for the current beam with emittance around 13 nm.
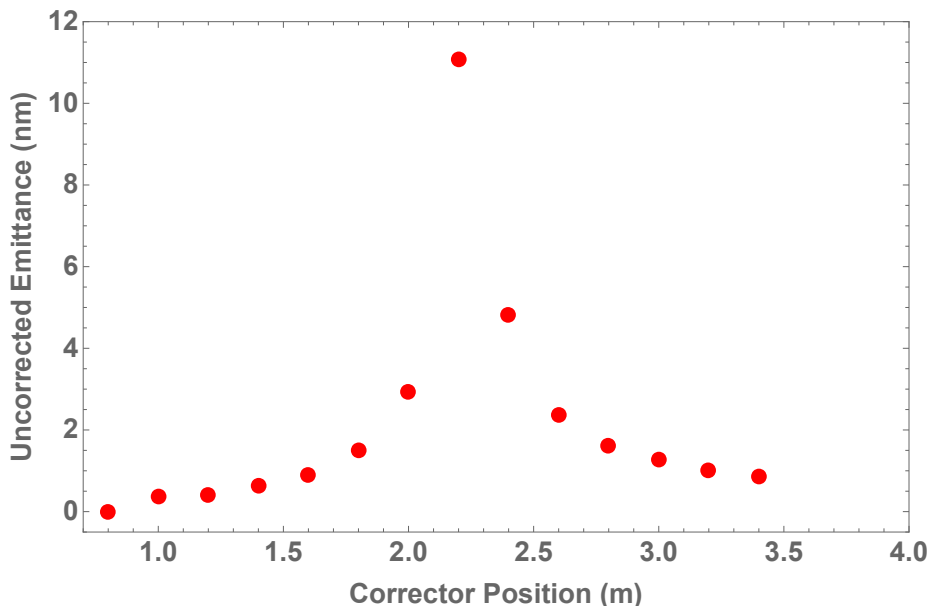
Figure 4.13: Simulated emittance correction for different placements of the sextupole corrector. At the position of the stray field, about .8m, the cancellation is exact as expected. The correction is worst at the beam focus where as expected correction is impossible.

To experimentally cancel the sextupole moment, the following procedure is used, which is shown in fig. 4.14. The triangular shape of the beam is recorded with the sextupole corrector turned off. The sextupole corrector is then turned on to a large current, such that the beam is a triangle with orientation determined solely by the sextupole corrector. The sextupole corrector is then rotated to produce a triangle which is inverted relative to the corrector off triangle. Lastly the current in the sextupole corrector is turned down until the shape of the beam is no longer triangular. After sextupole correction, we see the shape of the beam is not perfectly round, and has evidence of even higher order moments. The magnitude of these moments are relatively small, so fixing them will not be a focus of this chapter.

At different buncher voltages around the optimal bunching voltage, magnet settings were
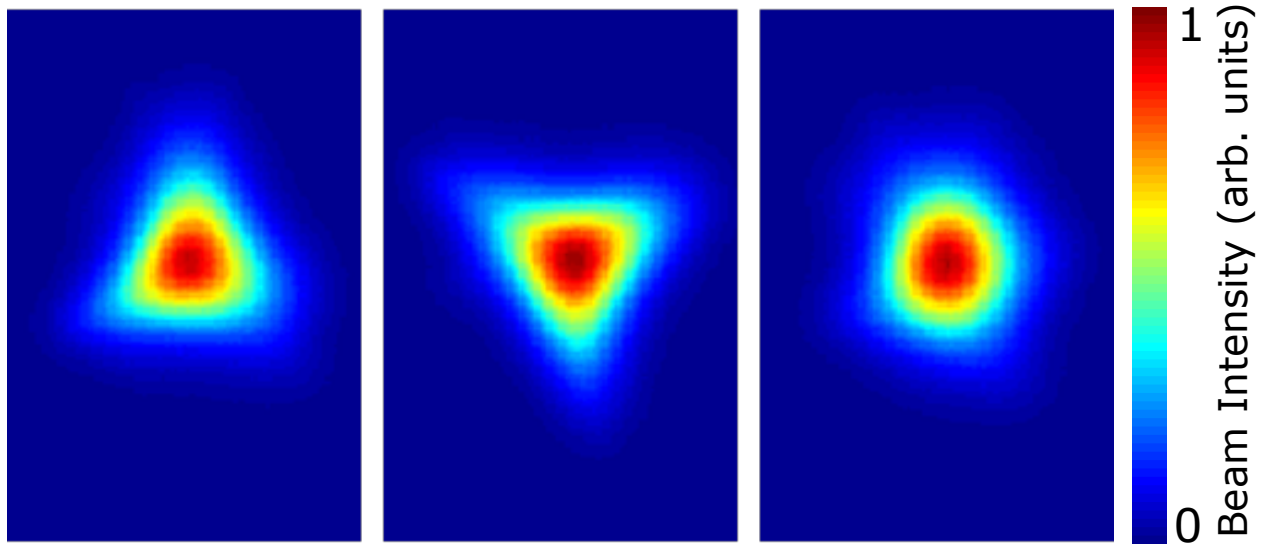
Figure 4.14: Experimental correction of the sextupole moment. From left to right the beam profiles are taken with: the sextupole corrector off, the sextupole corrector anti-aligned with sextupole moment at a large current, the sextupole correcter anti-aligned at a strength to cancel the sextupole moment.

found to optimize the amount of charge making it through the pinhole. This was done twice, once with the sextupole corrector off and once with it on and optimized. Plots of the transverse beam size and emittance as a function of the buncher voltage can be seen in figs. 4.15a and 4.15b.

Simulations of the beamline were done using a MTE of 70 meV which was chosen to best match the results of spot size and emittance simultaneously. With the addition of the sextupole corrector, the emittance of the beam is lower by around 25% and is fit by simulation with no sextupoles included. The points with the sextupole corrector turned off were fit by adding in a sextupole into the simulation, located in the buncher as done before.

Uncertainties in beam size and emittance are chosen based on machine state reproducibility. The measurements at the operating point for UED, with buncher voltage around 3.8 kV, were repeated 5 times, and the standard deviation of these measurements was used as the uncertainty.

An uncertainty in the fit MTE can be made by varying the MTE in simulation to the
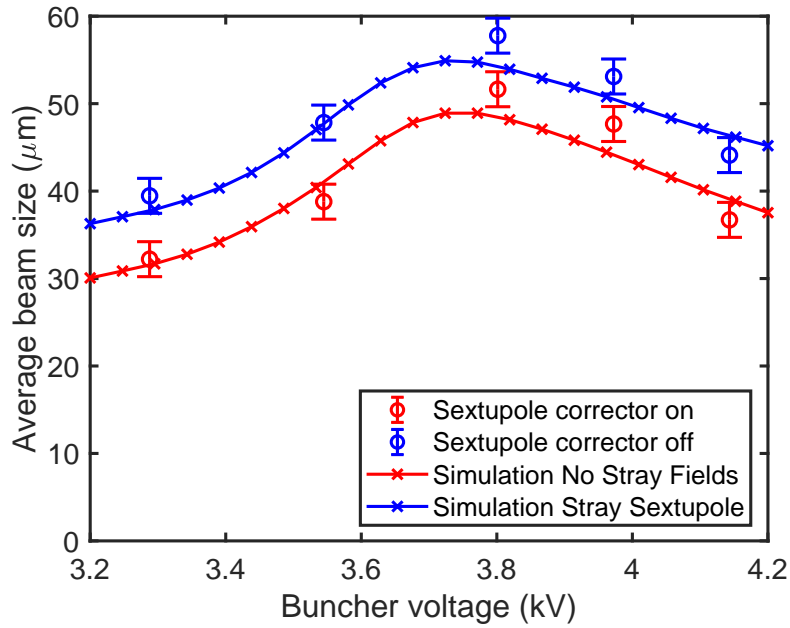
(a)
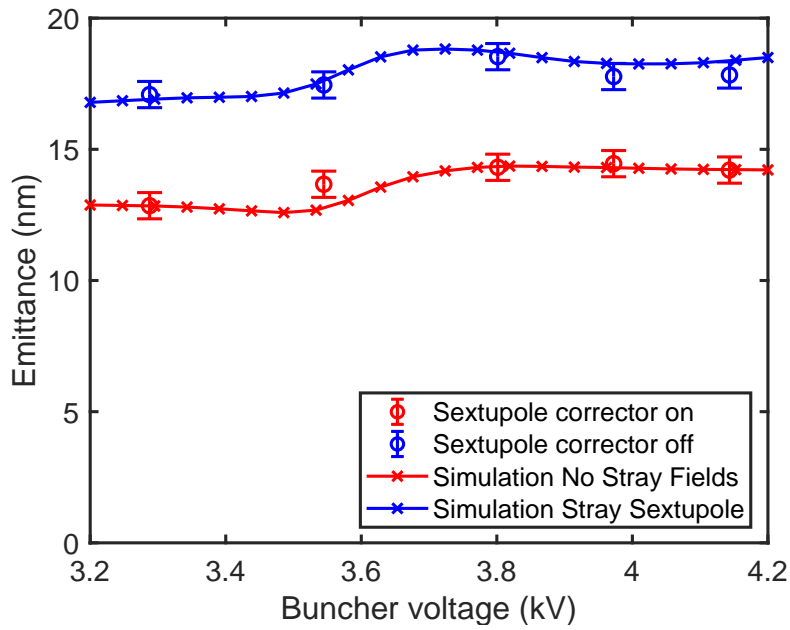
(b)

Figure 4.15: (a) Spot size and (b) transverse normalized rms emittance for different choices of buncher voltage around the optimal bunching voltage. The red line comes from simulation results assuming a MTE of 70 meV, chosen to best fit simultaneously the spot size and emittance data. The blue line was made simulating the same beamline with a sextupole added inside of the rf buncher, with a best-fit strength of the sextupole chosen.

extent that the simulated beam size and emittance vary by one standard deviation. Doing this gives a fit MTE of 70±20 meV. This is above the expected MTE from this photocathode of 50 meV. We attribute this increase in MTE to the photocathodes prolonged use.

4.7 Source of Sextupole

To confirm the source of the triangular beam was a sextupole inside of the buncher, the following procedure was used. First, the buncher phase was changed by 180° from a phase which makes a longitudinally converging beam to a diverging beam. The resulting transverse profile with the sextupole corrector off is shown in fig. 4.16.
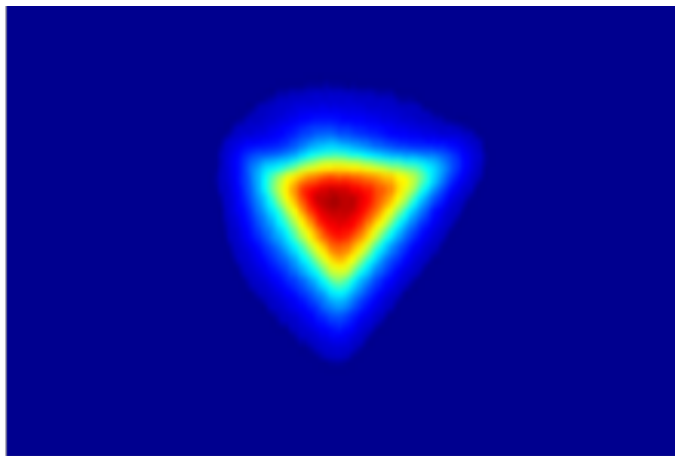
Figure 4.16: Beam profile with the sextupole buncher turned off and the RF buncher set to a longitudinal diverging beam phase. The triangle is seen to be inverted compared to the bunching phase.

The inverted triangle from the phase change can be explained by two causes. One possible cause is that there is a time dependent sextupole in the buncher, and when the RF buncher phase is changed by 180° the sign of the sextupole is flipped. Another possible cause can come from a longitudinal correlation in the beam, where different longitudinal components of the beam conspire to make a triangle, and by changing the energy kick given by the buncher, this effect was inverted. To examine the possibility of this second cause, a deflector cavity was placed inside the sample chamber of the beamline. The deflector cavity is a RF cavity

which gives a time dependent transverse kick to the beam depending on its longitudinal position. Thus the longitudinal profile of the beam can be projected onto a transverse axis, which we choose to be the vertical axis on the image shown.

The resulting beam distribution after being deflected is shown in fig. 4.17. The variation of the horizontal beam size over the longitudinal length of the beam is about 20%. The sharp triangular shape of the beam is not possible with the small observed variation. Therefore, in combination with the stark agreement between the spot size and emittance agreement with and without the inclusion of a stray sextupole field, the likely explanation of the phenomenon is a time-dependent sextupole in the buncher.
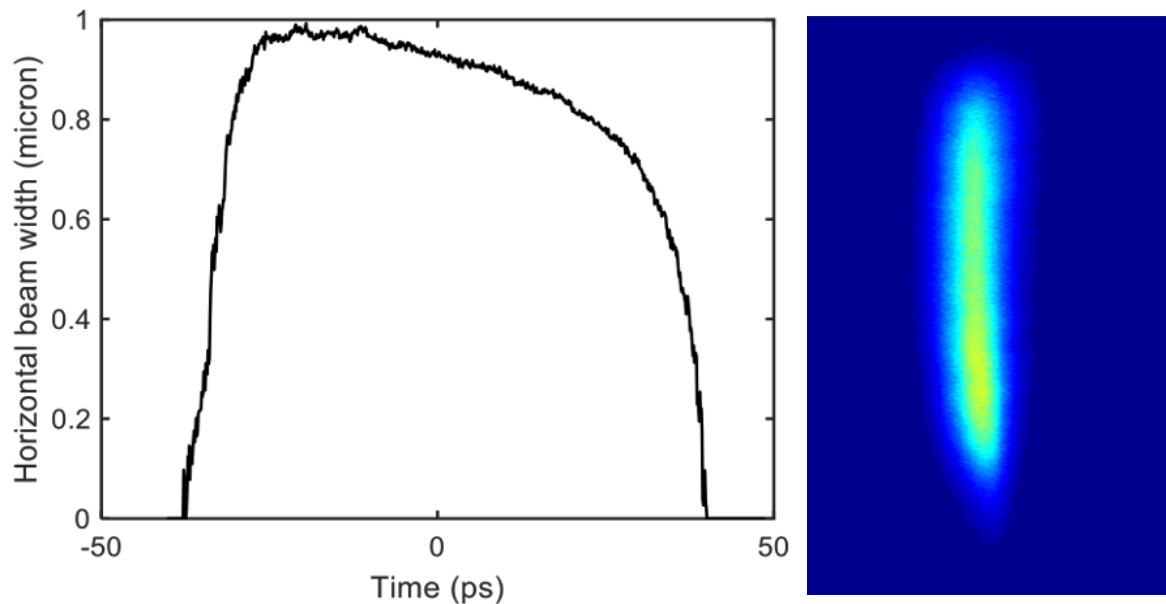
Figure 4.17: Beam profile in debunching phase with the deflector cavity on. Horizontal beam width is plotted as a function of the vertical position, in units of the longitudinal position of the beam in the deflector.

4.8   Summary and Outlook

Low MTE photocathodes produce high quality electron beams for time-resolved science. Preserving the quality of these beams from production to application can be non-trivial due

to the existence of non-linear fields in the beamline. By designing and tuning magnets up to sextupole, the effects of these non-linear fields on the beam quality were corrected, and the emittance of the beam is well predicted by simulation. Doing this we find that the beam is well represented by a cathode with a MTE of 70±20 meV. With the beamline now fully corrected of stray fields, the transverse coherence length of the beamline is now maximized as well as the range of phenomenon it can explore.

CHAPTER 5

POINT-TO-POINT EFFECTS IN HIGH BRIGHTNESS

PHOTOELECTRON BEAMLINES

This chapter is a slightly edited version of my work published in Physical Review: Accelerators and Beams [62], Copyright © 2011 by American Physical Society. All rights reserved. This work, as opposed to the previous chapter, focuses on issues that UED beamlines will face in the future, when photocathode technology has sufficiently advanced to produce very low MTE electron beams.

5.1   Failure of the Mean-Field Space Charge Approximation

The development of high brightness photocathodes is a driving force in the improvement of electron accelerator technologies such as free electron lasers, energy recovery linacs, and ultrafast electron diffraction and microscopy (UED and UEM). The brightness of the beams used in these applications is set at the electron source and can only degrade during further acceleration and transport. Consequently, the brightness of the electron source defines the ultimate limits of the capabilities of these devices [41, 63, 64, 65]. The photocathode brightness is set by two parameters: the density of electrons emitted from the source, and their mean transverse energy (MTE), which acts as an effective beam temperature [66, 67]. Increasing the electron density at the source is not always a viable option, as space charge forces can reduce brightness downstream dramatically. While some of this brightness can be restored via emittance compensation, some is lost to nonlinear distortions which are challenging to reverse [40, 68]. However, it has been shown in many modern applications that reducing the MTE of the photocathode can still lead to large gains in brightness [69].

Reducing the MTE of photocathodes is a very active area of research in which significant progress has been made in the last decade. Typical photocathodes used in accelerator

facilities today have a MTE of a few hundred meV [70, 71, 72] whereas near threshold emission at room temperature has demonstrated electron beams with an MTE of ~ 25 meV [73]. Furthermore, cryocooled photocathodes near threshold have shown the capability to go down even further to an MTE of ~ 5 meV [74]. At these low temperatures, point-to-point interactions play an increasingly important role in the overall beam dynamics, as shown by the following argument.

The mean-field approximation commonly used in simulation codes is only valid when there are many particles in a Debye sphere, see fig. 5.1. This Debye screening length is given by:

$$\lambda = \sqrt{\frac{\epsilon_0 kT}{n_0 e^2}} \tag{5.1}$$

where ϵ_0 is the permittivity of free space, k is the Boltzmann constant, T is the temperature of the beam, n_0 is the volume number density of the beam, and e is the charge of the electron. For $kT = 5$ meV and a density of $10^{17} \mathrm{m}^{-1/3}$ (commonly achieved in photoinjectors today), the Debye screening length is approximately 1.7 μm. However, the average interparticle spacing, $n_0^{-1/3}$ at the same density is 2.2 μm. Thus very few electrons will be within one Debye screening length of any given electron [75]. This situation has been studied extensively for ultracold gas-based plasma and electron sources, which exhibit single meV electron temperatures in photoemission [76, 77, 78, 79, 80, 81, 82, 83].

Brute force calculation of the pairwise Coulomb interaction scales with the square of the number of electrons, $\mathcal{O}(N^2)$, making it prohibitively time consuming to exactly simulate dynamics with large number of electrons. Thus, to accurately capture the beam dynamics, approximation methods are used which compute pairwise interactions of nearby particles, while approximating long range interactions using the mean-field approach. These methods scale as $\mathcal{O}(N \log N)$ for traditional tree-based methods and $\mathcal{O}(N)$ for the fast multipole method, making them feasible for simulation [84, 85]. We will refer to these methods as point-to-point methods.
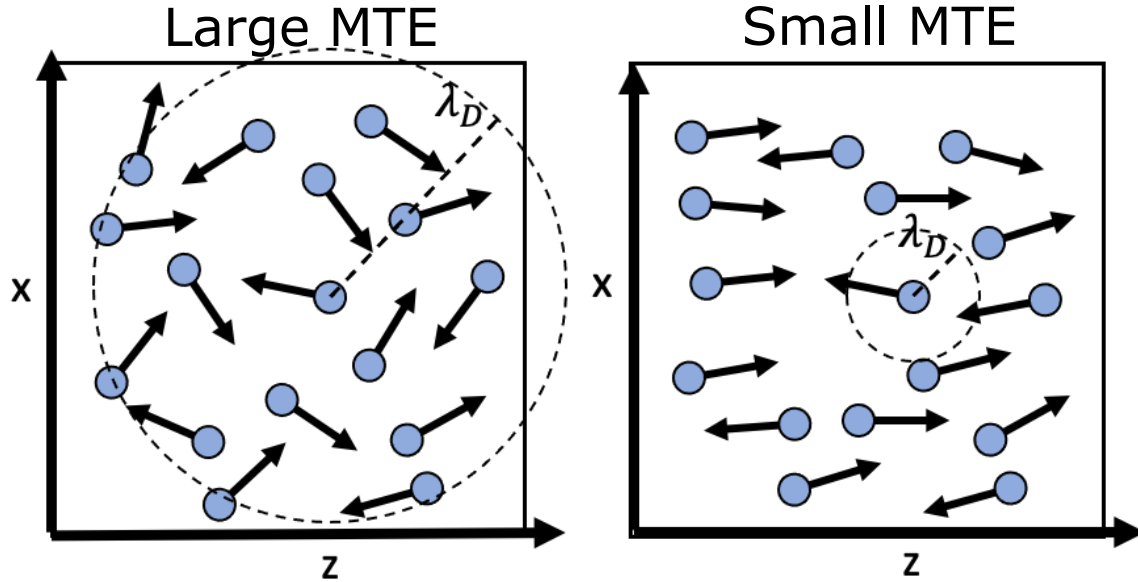
Figure 5.1: Cartoon depiction of the failure of Debye screening. For large MTE photo-cathodes, drawing a sphere around a particle with the Debye screening length as the radius encloses many other particles, a necessary condition for the applicability of mean field theory. At lower MTE, the Debye screening length becomes less than the average interparticle distance

A critical challenge in employing a classical point-charge force model for a photoelectron source is the unphysical divergence of the image potential at the cathode surface. The underlying cause of the problem is that classical equations of motion are not valid at and very near the cathode surface. In a classical simulation however, the size of the integration step typically scales inversely proportional to the gradient of the potential. Thus, near a divergence, the integration step can limit to zero. This produces a scale-matching problem wherein very small step sizes must be maintained throughout the particle emission process, which can lead to prohibitively long simulation times. However, as will be shown below, image charge effects significantly impact beam size and emittance evolution, and cannot be ignored.

This work aims to extend the work on Coulomb effects in ultracold plasma electron sources to photocathode guns, which can potentially support even higher beam density.

We provide a new method to compute the image force which is free of divergences and tuning parameters. Using this model of the overall beam dynamics, we turn to introduce new microscopic figures of merit to disentangle the global and local effects of point-to-point interactions.

To show the generality of the new methods, we examine beam dynamics in two very different UED beamlines based on archetypes used in practice today: a 200 keV dc gun with lower total initial beam density ($\sim 10^{17}$ m^{-3}), and a high gradient 5 MeV RF photoinjector with higher initial beam density ($\sim 10^{18}$ m^{-3}). UED is a good test case for examining point-to-point effects as the number of particles needed per bunch is often relatively small (10^5-10^7) in comparison to synchrotron radiation applications, making it feasible to simulate every particle in the bunch with modest computing resources. Along with this, the short bunch lengths, small spot sizes, and long coherence lengths needed to make atomic scale resolution diffraction patterns with femtosecond time resolution ultimately result in peak current densities comparable to those in free electron laser injectors [41, 86].

Using our new method of calculating near-photocathode dynamics, we highlight one unique point-to-point phenomenon called disorder induced heating (DIH) which arises very near the photocathode. DIH was originally studied in the ultracold plasma community (see e.g. [87]), but it may have significant implications for cold photoemitted electron beams [80, 88]. DIH is the thermalization of the initial potential energy stored in the random positions of near neighbor photoelectrons. Upon thermalization, the particle distribution develops a characteristic microscopic structure with a lack of near neighbors, and the beam simultaneously suffers emittance growth due to the increased temperature. For a stationary (non-accelerating, no expansion) electron bunch starting with zero temperature, the temperature rise due to DIH is given by:

$$kT_{\mathrm{DIH}} = \frac{Ce^2}{4\pi\epsilon_0 a} \tag{5.2}$$

where $a = (3/4\pi n_0)^{1/3}$ is the Wigner-Seitz radius of the bunch, and k is the Boltzmann constant. C is a dimensionless constant which can be determined by tabulated plasma correlation energies to be roughly $C \approx 0.45$ [89, 88]. The timescale τ of the thermalization can be calculated to be a constant fraction of a plasma period [90]. In photoinjectors, this time is typically of the order of ten picoseconds or less, resulting in thermalization near the photocathode during initial acceleration. A correct image charge model is thus critical to understand DIH in photoinjectors. Furthermore, the beam density can change significantly near the photocathode due to space charge expansion and acceleration. The resulting balance has not been studied in detail in photocathode guns before.

In this work we introduce new methods for simulating high brightness photoelectron beamlines. We simulate two UED beamlines with 0 meV MTE with multiple methods of calculating the electrons interactions to show why these new methods are crucial for accurately determining the capabilities of these devices. Next, we quantify DIH via an analysis of the resulting microscopic density distribution. We then estimate the rms emittance increase attributable to DIH, and find that it is the dominant source of emittance dilution in the two cases under study.

5.2   Point-to-Point Simulation Methods

5.2.1   Coulomb interactions and Image Charge Model

The simulations shown in this chapter were performed with the space charge tracking code General Particle Tracer (GPT) [91] using three different algorithms. The first is GPT's mean-field space charge algorithm, a non-equidistant 3D multi-grid Poisson solver [35], which is used to calculate the mean-field interaction of the entire bunch, including image charge effects. The second is the Barnes-Hut algorithm internal to GPT [84], with a Barnes-Hut angle parameter of 0.3, used to model point-to-point Coulomb interactions. It does this by

exactly computing the electric fields from near neighbor particles at each time step using Coulomb's law whereas long-range interactions are approximated using multipole expansions. This makes the Barnes-Hut algorithm capable of simulating stochastic effects like disorder induced heating and Boersch effect, while also taking into account long-range space charge forces. However, due to divergent fields at the cathode, the Barnes-Hut algorithm does not allow for simple inclusion of image effects. To include these effects, we developed a third technique, which we call the Plus-Minus-Plus (PMP) Method.
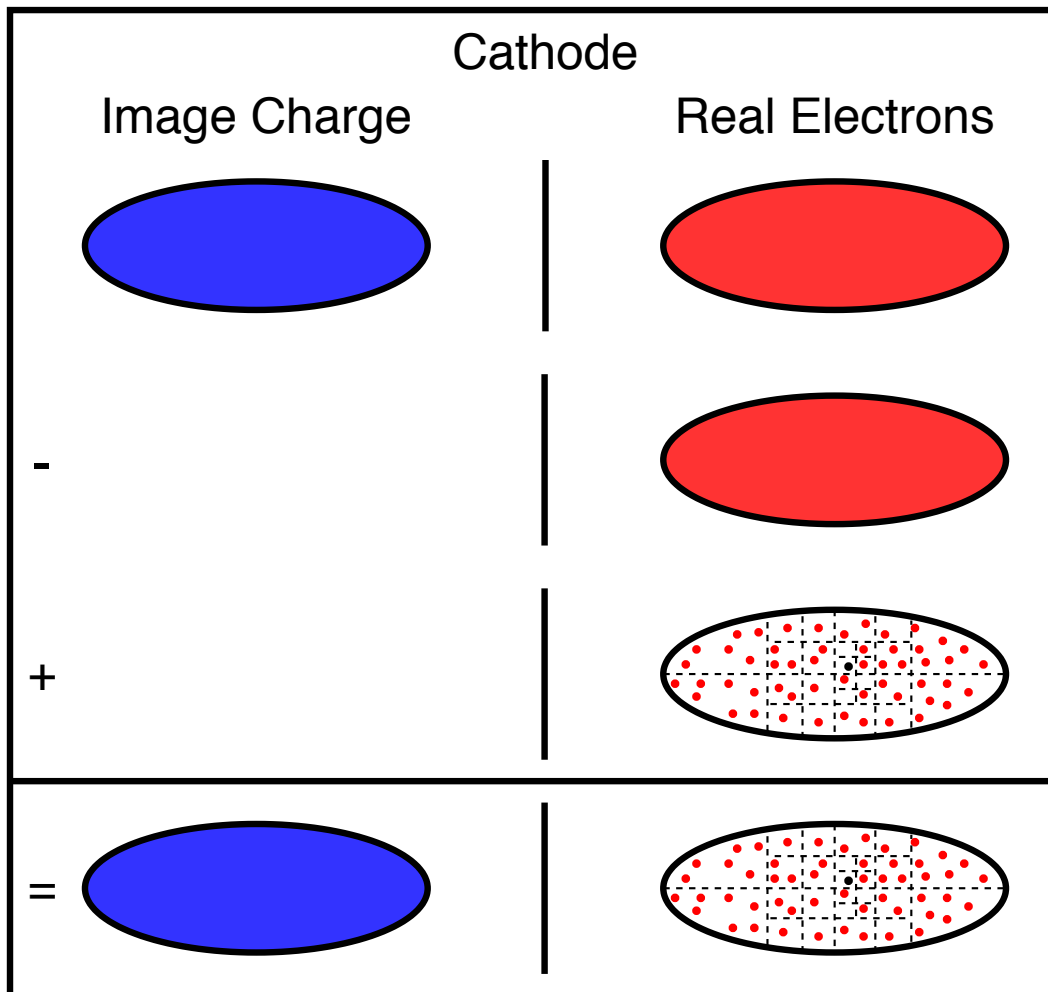
Figure 5.2: Depiction of PMP 3-step space charge calculation. Filled in ellipses represent mean-field calculation of electric fields, and ellipses filled with dots represent a Barnes-Hut calculation of electric fields.

The PMP method approximates the image charge as arising from a mean-field calculation

and the total space charge force is calculated in a three step process as depicted in Fig. 5.2. In PMP, GPT's mean-field space charge algorithm is used to calculate the mean-field interaction of the entire bunch, including image effects. Subsequently, a second call is made to the mean-field solver, but this time without the cathode boundary condition. By subtracting this field from the initial full mean-field space charge calculation, the mean-field approximation of the image field alone is extracted. The last step in the PMP process adds the stochastic interactions to the previously obtained mean-field image charges with the stochastic Barnes-Hut point-to-point method.

In section 5.7 we discuss the accuracy of the assumption of a mean-field image force. Specifically we compare the PMP method with another image charge method which includes point-to-point effects via a dynamical image charge potential which does not diverge [92]. The latter requires additional computing time and tuning parameters, and in general we find good agreement with PMP. Thus PMP is my method of choice throughout the chapter. One additional method of simulating the image potential is discussed in appendix C

To achieve an accurate accounting of stochastic Coulomb effects, each macroparticle represents exactly 1 electron in all simulations, and all distributions are pseduo-random, rather than quasi-random. These same macroparticle settings were used in the mean-field simulations for consistency.

To test the convergence of GPT's mean-field space charge algorithm, the same beamline was simulated multiple times using different space charge solver parameters. We set a convergence limit of 5% relative variation in rms quantities with increasing space charge accuracy. We found that nearly all default settings for GPT's mean field space charge solver were sufficient to satisfy this limit, except for the total number of meshlines which was increased by 20% such that the variation was below this threshold.

5.2.2   Using 90% RMS Figures of Merit

Root-mean-squared (rms) figures of merit for beam size/length, energy spread, and emit-
tance are not well-defined in the presence of strong point-to-point Coulomb interactions.
This is due to the presence of large angle scattering which generates long-tailed distributions
for which rms values diverge [93]. To avoid sensitivity to outliers, but retain the sense of
the traditional accelerator figures of merit, all quantities presented in this chapter are cal-
culated using 90% rms values unless otherwise denoted, wherein a subset of the distribution
containing 90% of the particles are chosen such that the metric in question is minimized.

5.3   Description of dc and NCRF gun UED beamlines

Both beamline designs considered here originated from a multiobjective genetic algorithm
(MOGA) optimization study, using the mean-field space charge model, to provide an emit-
tance minimum at the sample plane with realistic constraints on the bunch length and spot
size. These optimizations are described in Refs. [69, 94, 95]. Each case shown here is an
individual from a MOGA Pareto optimal frontier with a MTE of 0 meV. Individuals were
selected containing a charge closest to 10^5 electrons/pulse, and were then re-evalutated using
the PMP method.
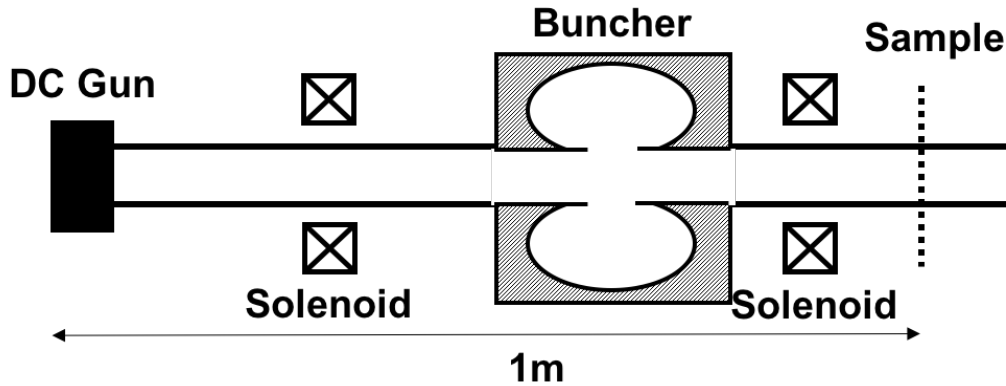
Figure 5.3: Layout of the cryocooled dc gun UED beamline used in the following simulations.

The lower energy dc beamline, depicted schematically in Fig. 5.3, consists of a cryocooled 200 kV dc gun [96] with an extraction electric field of 11.25 MV/m, followed by a solenoid, a normal conducting 3.0 GHz buncher cavity of the Eindhoven design [97], and a second solenoid. The beamline was optimized to have a minimal emittance at a sample location approximately 1 m from the cathode when emitting an electron beam with 0 meV MTE [94]. Beam parameters are shown in table 5.1.

Table 5.1: dc beamline simulation beam parameters

Parameter	Value
Bunch Charge (fC)	-14
Transverse rms Size (μm)	8.1
Laser Pulse Length (ps)	9.8

The higher energy NCRF beamline, depicted schematically in Fig. 5.4, consists of a 1.6 cell 2.856 GHz NCRF gun of the BNL/SLAC/UCLA design [98], with a peak electric field of 100 MV/m, launch phase of 38.6 degrees from peak field, and final beam energy of 5 MeV, followed by a solenoid, a 9 cell buncher cavity, and a second solenoid. The buncher is modeled using 9 copies of the first cell of the SLAC linac [99]. The beamline was optimized to have a minimal emittance at a sample location approximately 2.5 m from the cathode when emitting an electron beam with 0 meV MTE [95]. Beam parameters are shown in table 5.2.

Table 5.2: NCRF beamline simulation beam parameters

Parameter	Value
Bunch Charge (fC)	-17
Transverse rms Size (μm)	2.5
Laser Pulse Length (ps)	3.2
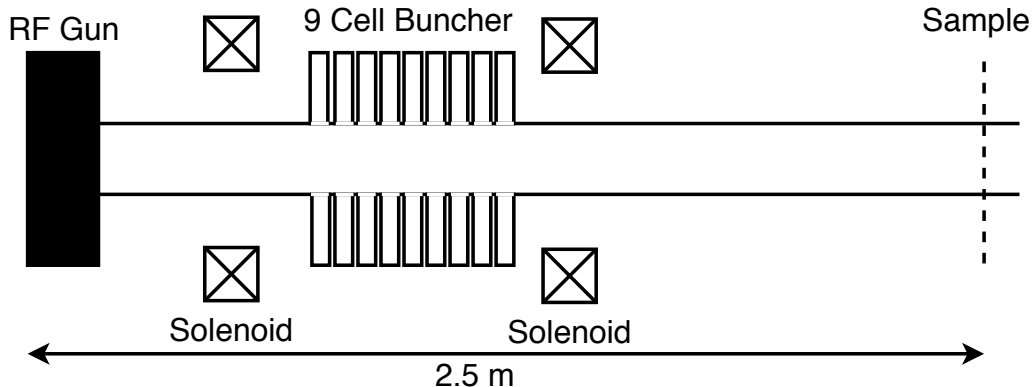
Figure 5.4: Layout of the NCRF gun beamline used in the following simulations.

5.4   Macroscopic Beam Evolution

The 90% rms transverse size of the beam along the dc and NCRF UED beamline is shown in Figs. 5.5a and 5.6a respectively. In all simulations, space charge increases the beam size, after which the first solenoid matches the beam size into the buncher cavity (which has a noticeable transverse defocusing), and the second solenoid forms the final waist. As expected from the emittance compensation process, the emittance minimum occurs very near the beam size waist.

In the Barnes-Hut simulation without the cathode boundary condition, the initial space charge blowup leads to a larger spot size at the first solenoid. Because of this, the focusing elements cause the beam waist to occur earlier than when the image force is included. Thus, omission of the image force generates significantly different beam dynamics.

The difference between the mean-field and PMP simulation is solely due to point-to-point effects, as a mean-field image force is included in each. It is interesting to note that the slightly larger spot size in PMP simulations translates to noticeably stronger focusing downstream. In the DC gun beamline, the stronger focusing is noted by a smaller beam size at the focus, and in the NCRF beamline, the beam waist is formed earlier by 5.5 cm.

The evolution of the normalized transverse rms emittance for the dc and NCRF UED beamline with 0 meV MTE is shown in Figs. 5.5b and 5.6b respectively. Starting at an emit-
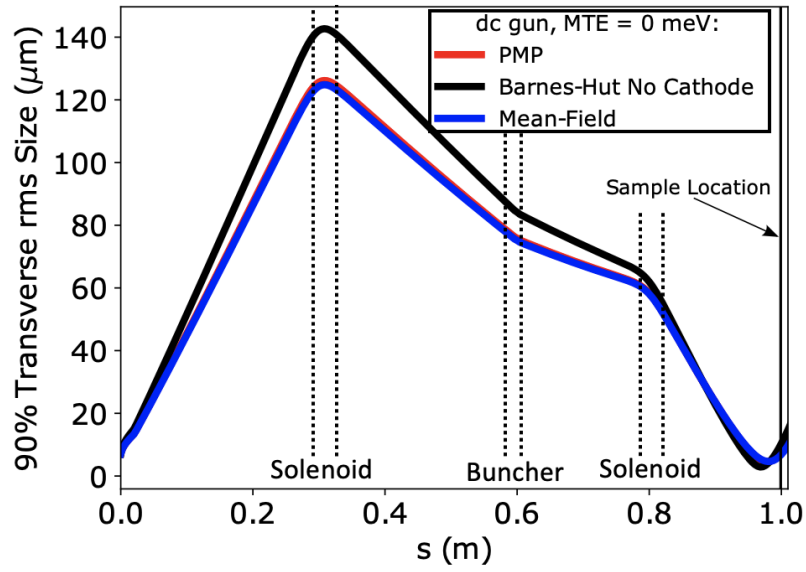
(a)
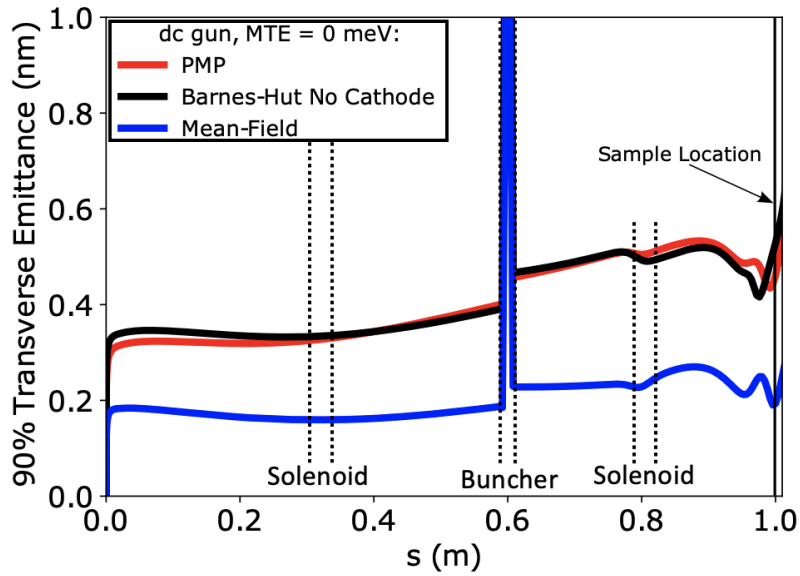
(b)

Figure 5.5: (a) Spot size and (b) transverse normalized rms emittance comparison between the PMP method, Barnes-Hut method without a cathode, and mean-field space charge simulations of the dc UED beamline with 0 meV MTE.

(a)

(b)
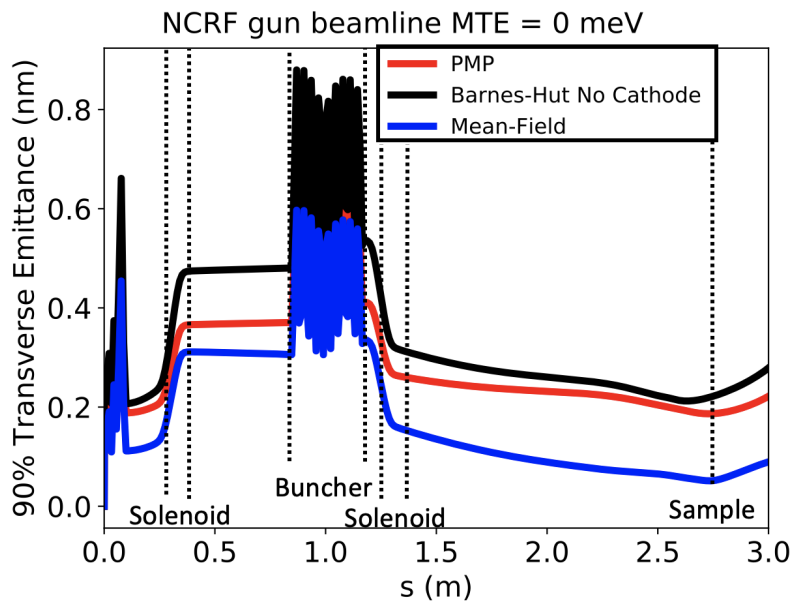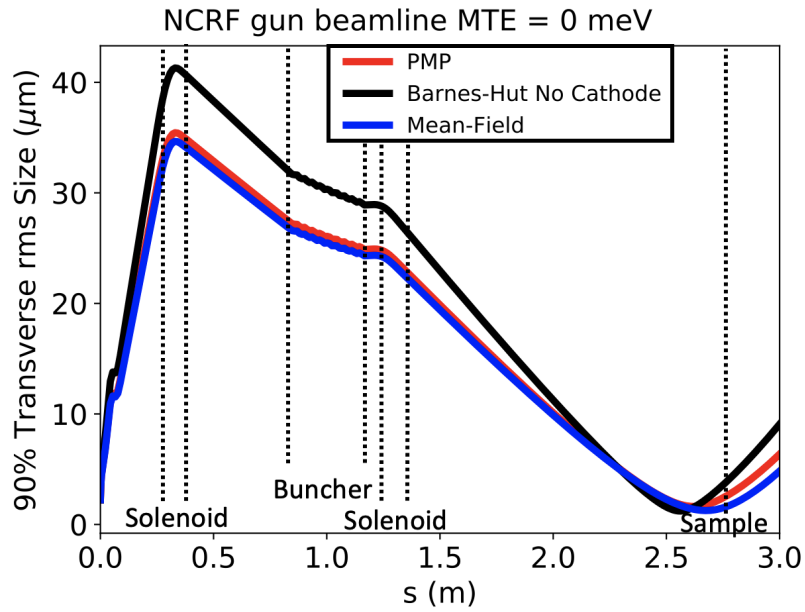
Figure 5.6: (a) Spot size and (b) transverse normalized rms emittance comparison between the PMP method, Barnes-Hut method without a cathode, and mean-field space charge simulations of the NCRF UED beamline with 0 meV MTE.

tance of zero, the emittance quickly grows as the beams experience both the mean-field space charge phase space shearing, and also a growth in temperature due to the thermalization of the initial stochastic potential energy stored between near neighbors.

Comparing the transverse 90% rms emittance of the Barnes-Hut method without a cathode to the PMP method, we find that qualitatively they behave similarly. However, due to the earlier location of the beam waist in the Barnes-Hut simulations, the location of the emittance minima also shifts to an earlier position.

Although at a higher beam energy, we note the NCRF beamline exhibits a larger relative effect from point-to-point interactions. Later we will show that this can be explained by the effects of DIH with a larger initial electron number density. Though the space charge forces are more heavily suppressed at high energy, the effects of DIH thermalization occur at low energy near the cathode where relativistic suppression is negligible. The timescale of the evolution of the thermalization is a constant fraction of the plasma period [88], which in this case is roughly 30 ps. The value of the emittance is over a factor of 3.7 larger than when using only the mean-field approximation when including point-to-point effects.

It should be noted that because these beamlines were optimized to minimize the emittance of the mean-field space charge beam with 0 meV MTE at the sample, the emittance in the PMP simulation is not necessarily optimized to be maximally compensated at its respective minimum. Thus, these numbers represent an upper bound to the maximal effect of point-to-point space charge on the emittance for these UED beamlines. However, as we will show later, most of the emittance growth above the mean-field case arises from microscopic DIH-like effects, which are insensitive to small perturbations in the focusing optics.

The slice energy spread results from the two beamlines are shown in table 5.3. In both beamlines, the slice energy spread slowly varies, except for jumps at their respective gun, buncher, and beam waist. The energy spread has time dependence affecting the second significant figure, so only the most significant figure is reported.

Table 5.3: Slice energy spread in 0 meV MTE simulations

Simulation	$\frac{\sigma_E}{E}$ Before Buncher	$\frac{\sigma_E}{E}$ After Buncher
dc(PMP)	5×10^{-6}	5×10^{-5}
dc(Barnes-Hut)	5×10^{-6}	5×10^{-5}
dc(mean-field)	9×10^{-7}	5×10^{-5}
NCRF(PMP)	4×10^{-5}	3×10^{-4}
NCRF(Barnes-Hut)	4×10^{-5}	3×10^{-4}
NCRF(mean-field)	4×10^{-5}	3×10^{-4}

In all simulations, the bunch length is approximately constant until the buncher, after which it decreases linearly in time. In the dc beamline, the bunch length at the sample is 0.92 ps in the PMP simulation and 0.91 ps in the mean-field simulation. In the NCRF beamline, the bunch length at the sample is 0.91 ps in both simulations. Thus, point-to-point effects do not play a large role in determining bunch length at the sample. We note here that the bunch lengths at the sample location are higher here than in many UED setups which achieve temporal resolution well below 1 ps. Optimizations of time-resolved electron scattering instruments inherently have a tradeoff between transverse emittance and longitudinal size, and the optimal point on this tradeoff curve depends on the phenomenon being studied. By choosing a very small transverse emittance at the expense of bunch length, the longitudinal dynamics are less sensitive to stochastic effects than the transverse dynamics, making these simulations a more stringent test of DIH.

5.5   Microscopic Evolution

We now move to analyze the microscopic real and phase space distributions in an effort to determine to what extent they follow simple predictions of beam heating via DIH, and to what extent this heating determines the total rms emittance growth from point-to-point effects.

5.5.1   Core Emittance
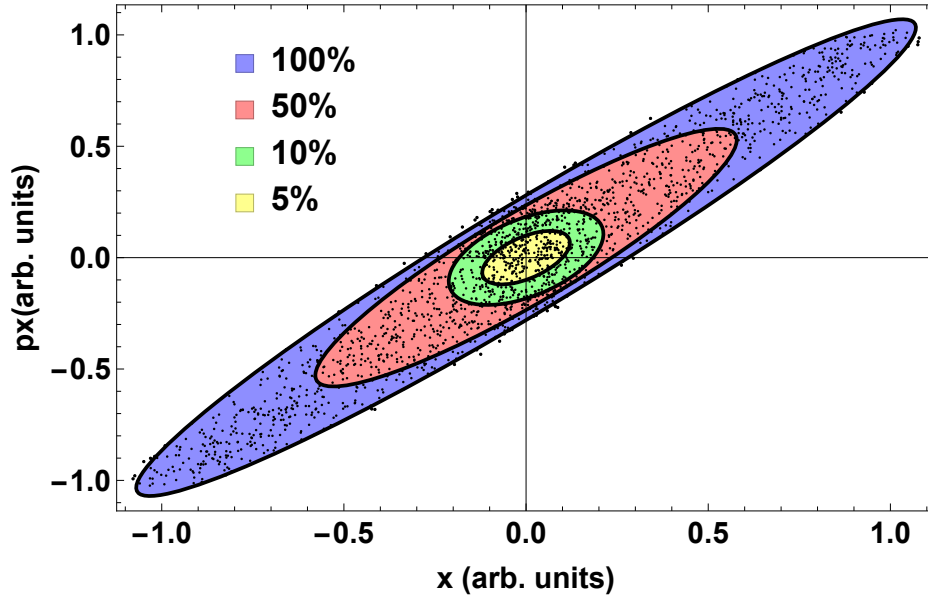
Figure 5.7: Depiction of emittance vs. particle fraction selection. Ellipses are drawn such that they represent the phase space area occupied by the beam using only a given fraction of the total number of particles. Ellipse dimensions are selected such that the emittance is minimized for each particle fraction.

One tool which can be used to analyze the microscopic evolution of a beam is the core emittance. The core emittance is a measure of the peak transverse phase space density. It is defined through an emittance vs. particle fraction curve [100]. Starting with the full beam emittance (particle fraction of 1), particles can be excluded from the emittance calculation such that the resulting emittance is minimized, see Fig. 5.7. The core emittance is defined as the limit of the slope of the emittance vs. particle fraction curve as the particle fraction goes to 0. It is inversely proportional to the peak transverse phase space density:

$$\epsilon_c = \frac{d\epsilon}{df}\bigg|_{f \to 0^+} = \frac{1}{4\pi\rho_0} \tag{5.3}$$

where ϵ is the emittance of the beam for a given fraction of particles, f is the particle fraction and ρ_0 is the peak phase space density. We expect ρ_0 to be invariant in mean-field space charge systems, but the introduction of point-to-point effects can break this invariance.
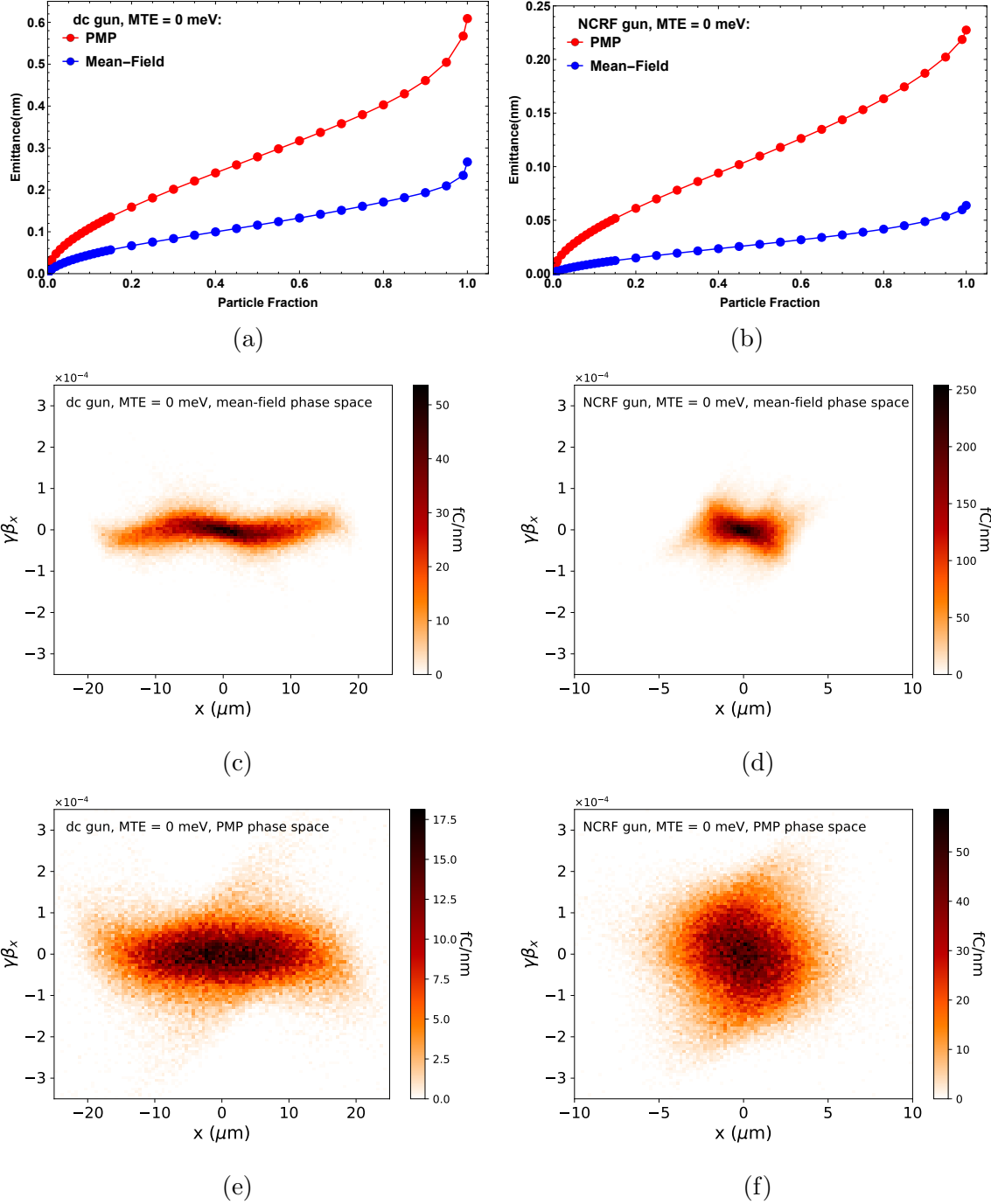
Figure 5.8: Transverse normalized rms emittance vs. particle fraction plots and phase space comparison between PMP and mean-field simulations of the 2 UED beamlines at the respective emittance minimum near the end of the beamlines. Subfigures (a), (c), and (e) correspond to the dc beamline and subfigures (b), (d), and (f) correspond to the NCRF beamline. Phase space portraits from the mean-field simulations are shown in subfigures (c) and (d) and for PMP simulations in (e) and (f) Phase space portraits are shown with linear $x - p_x$ correlation removed.

However, because we compute the core emittance with a finite number of beam particles and a finite number of bounding ellipses the value will never be exactly zero even if we start with zero MTE.

In Figs. 5.8a and 5.8b, the emittance vs. fraction curves at the emittance minima are shown for mean-field and point-to-point space charge for the dc gun and NCRF gun UED beamlines. Note the sharp increase in rms emittance due to outliers when the particle fraction approaches unity. As can be seen, for small particle fractions the emittance of the PMP simulation is significantly higher than that of the mean-field simulation. This shows that point-to-point effects not only have created more outliers, but have fundamentally degraded beam quality up to and including the core of the beam, as would be expected from DIH. To help illustrate this further, phase space portraits are shown at the respective emittance minima for the two beamlines with mean-field space charge in Figs. 5.8c and 5.8d and with PMP space charge in Figs. 5.8e and 5.8f. The decrease in core phase-space density is clearly seen by the increased width in the $\gamma\beta_x$ coordinate in Figs. 5.8e and 5.8f. Note that the faint diagonal tails in these figures are not outliers due to stochastic interactions, but the effect of slightly mistuned optics.

The core emittance of the beam was computed at different points along the dc beamline, see Fig. 5.9, and Fig. 5.10 for the NCRF gun beamline. After a quick initial rise at low energy, the core emittance in the point-to-point simulations remains far above that of the mean-field simulation.

The core emittance at the sample of these simulations is shown in table 5.4. As with the transverse rms emittance, the effects of point-to-point space charge are more distinct in the NCRF beamline, where the number density of electrons is higher.

Table 5.4: Core emittance with 0 meV MTE at sample

Beamline	PMP ϵ_c (nm)	mean-field ϵ_c (nm)
dc	0.28	0.08
NCRF	0.12	0.020
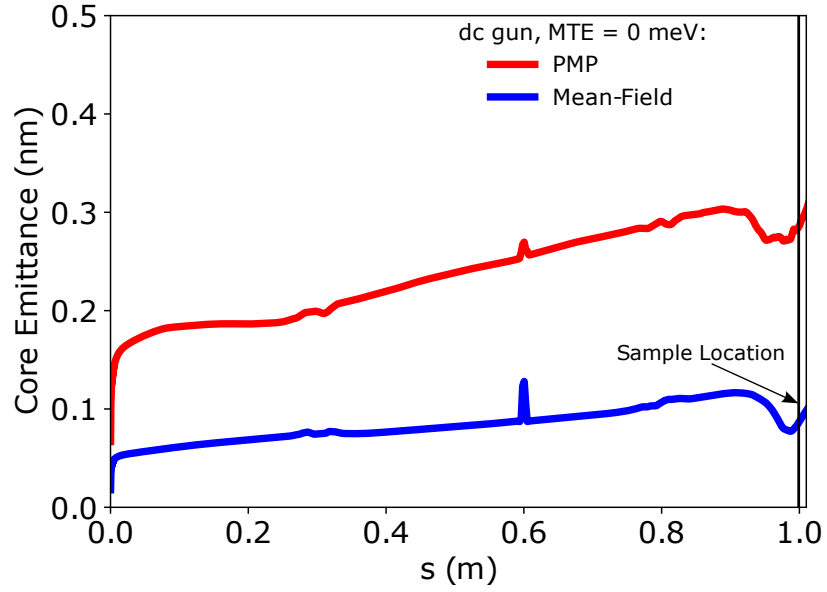
Figure 5.9: Core emittance comparison between PMP and mean-field simulations of the dc UED beamline with 0 meV MTE.

5.5.2   Radial Distribution Function

The radial distribution function, $g(r)$, of a system of particles relates the bulk density of particles to the local particle density as a function of distance from a reference particle [101]. A microscopically uniform distribution of particles has a constant radial distribution function excluding effects from finite system size. In this case, a neighbor particle to a given reference particle is equally likely to be found at any distance. However, due to the divergence of the Coulomb interaction, the number of very near neighbors to a reference particle in an electron beam evolves to become zero. This is known as the Coulomb hole and it results in a decrease of the total potential energy of the system [102]. This release of potential energy causes disorder induced heating, and we denote the resulting mean kinetic energy each particle gains from this heating by E_{DIH}.

   To calculate $g(r)$, the following procedure is used: Screen based outputs are taken from chosen positions along the beamline. Because we are interested in the dynamics of the core of
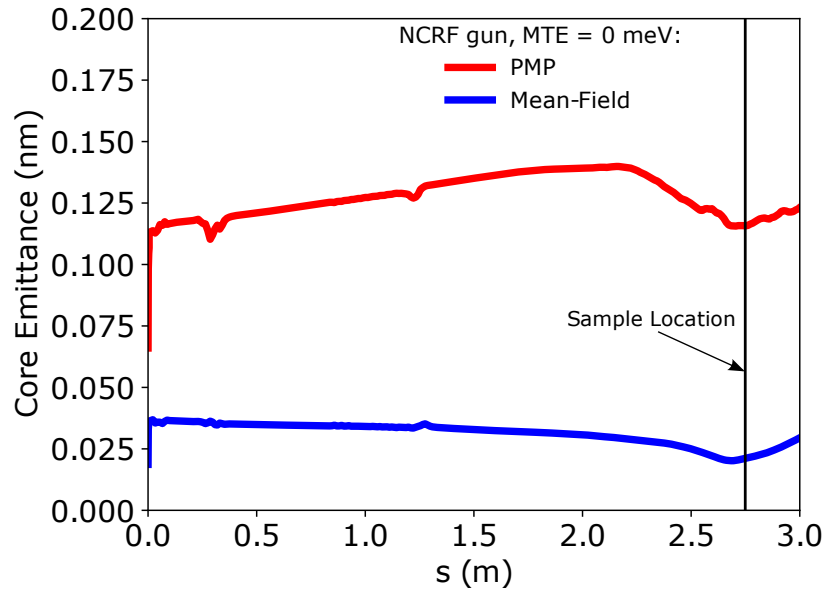
Figure 5.10: Core emittance comparison between PMP and mean-field space charge for the NCRF UED beamline with 0 MTE.
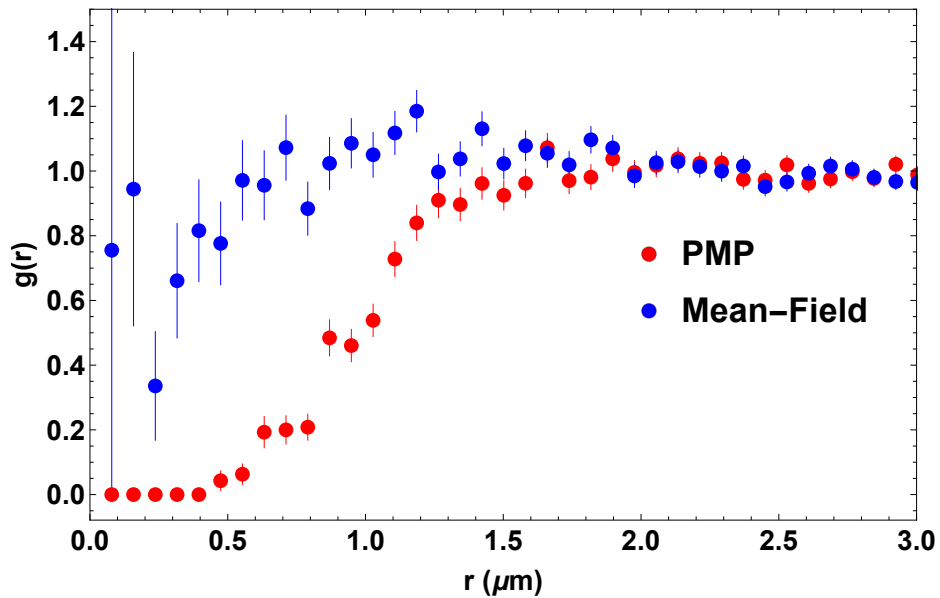
Figure 5.11: Radial distribution function comparison between PMP and mean-field simulations of the NCRF UED beamline with 0 meV MTE $\sim$ 3mm away from the cathode. Only a small r portion of the distribution is plotted to show the creation of the Coulomb hole when point-to-point space charge is used. For comparison, the distributions were normalized such that the mean of the radial distribution functions from 1.5μm to 3.0μm is equal to 1.

the beam, only the 10% of electrons which are closest to the longitudinal center of the beam are used. For each of these particles, the distance to every other selected particle is calculated. By making a histogram of these distances, we generate a plot of $g(r) \times \rho N \times 4\pi r^2 \Delta r$ as a function of r , where N is the number of particles, ρ is the bulk volume density of those particles, and Δr is the bin size. A statistical uncertainty is assigned to each bin equal to the square root of the number of particles in the bin. Dividing out the r^2 term, $g(r)$ is found up to numerical prefactors.

The radial distribution function shortly after emission in the case of the NCRF UED beamline with 0 meV MTE is shown in Fig. 5.11. For distances smaller than 1.5 μm, the radial distribution function in the case of point-to-point space charge decreases to 0 as expected, while $g(r)$ of mean-field space charge does not. This same behavior can be seen for the dc beamline with an MTE of 0 meV.

5.5.3   Disorder Induced Heating Calculation

From the radial distribution function, the potential energy of a particle due to its surrounding particles can be calculated as:

$$E_{\text{potential}} = \int_0^\infty 4\pi r^2 \rho g(r) u(r) \mathrm{d}r \qquad (5.4)$$

where ρ is the bulk volume density of the beam and $u(r)$ is the potential energy of two electrons particles separated by a distance r [103]. Using equation 5.4, E_{DIH} can be calculated by finding the difference between the potential energy calculated via the radial distribution function in the point-to-point simulation and a calculation using the same radial distribution function where the Coulomb hole is artificially filled. Tests with stationary distributions which have known E_{DIH} show that this estimation method is accurate to within 20%, with discrepancies arising primarily due to the determination of the peak location of $g(r)$.

This energy difference would be E_{DIH} for all times after heating if the beam did not change in size throughout the simulation. Because the beam size changes, additional calculation is required to recover E_{DIH}. If the beam changes in a self-similar way, such that its aspect ratio remains constant, the energy found through this subtraction is E_{DIH} multiplied by the ratio of the initial average interparticle distance (defined below) to the current average interparticle distance. This can be seen by investigating the radial scaling of equation 5.4 noting that $\rho \propto 1/r^3$ and $u(r) \propto 1/r$. Thus by multiplying by the inverse of this factor, we can estimate E_{DIH} assuming DIH takes place very near the cathode. Further, it is clear the assumption of self-similarity is invalid if the beam deviates significantly from its initial aspect ratio, which can occur when space charge forces cause significant "blowout" (spatial [104] or longitudinal [105]) and near most beam waists.

The initial interparticle spacing and initial electron density require definition, as at $t = 0$, no beam yet exists. To do this, we will approximate the beam as a uniform cylinder with equivalent rms sizes as at the cathode surface. Assuming a uniform acceleration over the small length and time scale the beam is being emitted from the cathode, the front of the beam will travel to a distance of $L = \frac{1}{2}a_{E_0}t^2$, where a_{E_0} is the acceleration of an electron in a uniform electric field E_0, and t is the difference in time between the first and last particle emitted. Approximating as a uniform distribution where $R = 2\sigma_R$ and $t = \sqrt{12}\sigma_t$, the volume of the beam can be found as:

$$V = \pi R^2 L \approx \frac{24\pi e E_0}{mc^2}\sigma_x^2(c\sigma_t)^2 \tag{5.5}$$

Using this volume, an initial average interparticle distance can be found as $\rho \approx (V/N)^{1/3}$ and initial electron density is $n_0 \approx (N/V)$.

A plot of the E_{DIH} estimate is shown in Fig. 5.12. There are three main features of this plot. First there is an initial rise in E_{DIH} corresponding to the time it takes for the Coulomb
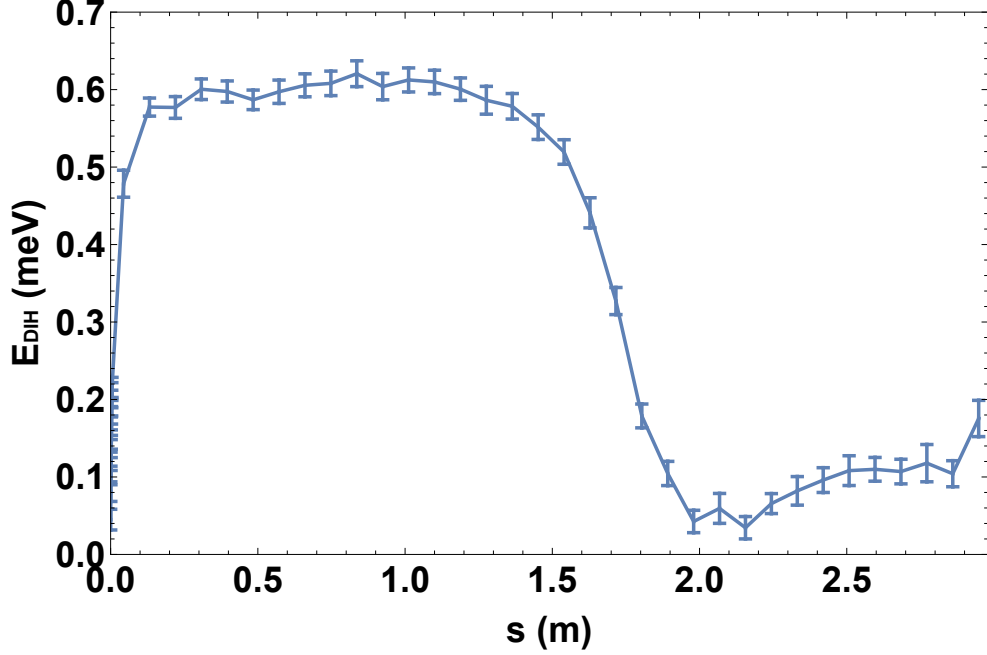
Figure 5.12: Energy from disorder induced heating as calculated from $g(r)$ in the NCRF beamline with 0 MTE and a smaller initial density of 10^{17} m^{-3}. The density was reduced by increasing the initial radial size of the electron beam at the cathode.

hole to form, i.e. the inverse plasma oscillation frequency of the beam:

$$\tau \approx 0.3\frac{2\pi}{\omega_p} = 0.6\pi \left(\frac{n_0 e^2}{m\epsilon_0}\right)^{-1/2} \tag{5.6}$$

where n_0 is the density of the electron beam [88]. After the initial rise there is a plateau. The mean value of this plateau is used for the value of E_{DIH} of the simulation, and the standard deviation of these values is treated as an uncertainty. The drop in E_{DIH} corresponds to the transverse focus of the beam. During this focusing, not only is the self-similarity assumption violated, there is another microscopic reorganization in which the Coulomb hole is filled. This is shown in Fig. 5.13. Please note that this downstream filling in the Coulomb hole does not have a significant impact on the core emittance of the beam anymore. This is because near the beam waist, the transverse temperature of the of the beam $mc^2(\epsilon/\sigma_x)^2$ is ~ 12 meV and the energy per particle required to fill the Coulomb hole is ~ 0.3 meV.
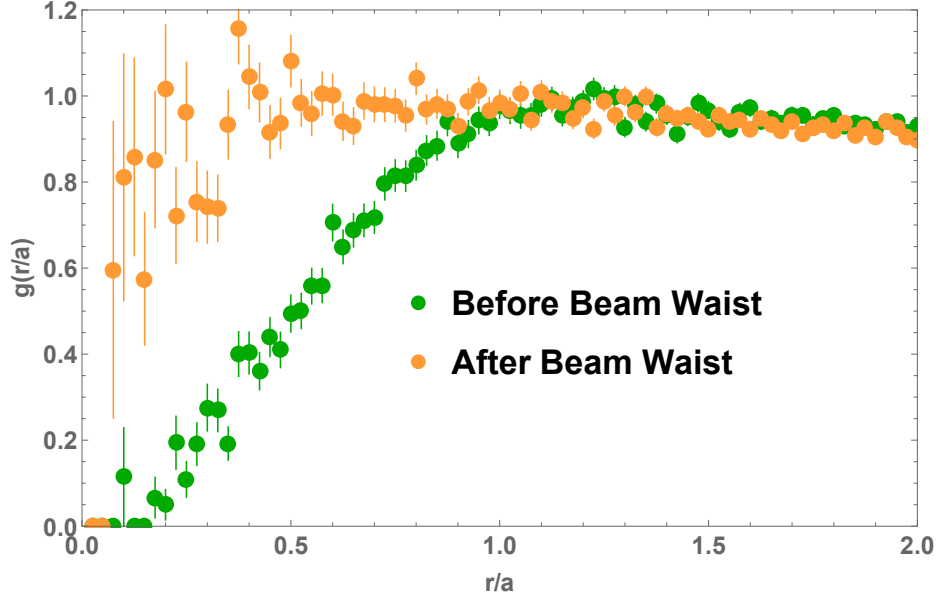
Figure 5.13: Radial distribution function comparison between of the NCRF beamline with an MTE of 0 meV and an initial density of 10^{17} m^{-3} before and after the beam waist. For comparison, the distances were normalized by the average interparticle distance, a, and the radial distribution functions, $g(r/a)$, were normalized such that $g(r/a = 1.25) = 1$.

5.5.4 Disorder Induced Heating Density Dependence

For a stationary electron plasma with a starting temperature of zero, the energy released by disorder induced heating can be calculated via Eq. 5.2. To test the density dependence of equation 5.2 in the realistic, non-stationary case, this procedure was repeated on simulations of the same NCRF beamline with 0 MTE, while changing the radius of the inital beam in order to alter its density. The result is shown in Fig. 5.14.

For densities of 10^{16} m^{-3} and above, the simulation results agree with the simple stationary theory within a factor of 2. At a density near $10^{15}m^{-1/3}$, the timescale for heating is ~ 1 ns, which is approximately the time it takes the beam to enter the first solenoid. Because the beam has had time to change significantly in size and shape, there is no reason to expect that the approximations used in calculating E_{DIH} remain true, thus it will be ignored in the following analysis. We find a that E_{DIH} in our simulations scales with density to the power 0.39 ± 0.02, close the value of $1/3$ in Eq. 5.2.
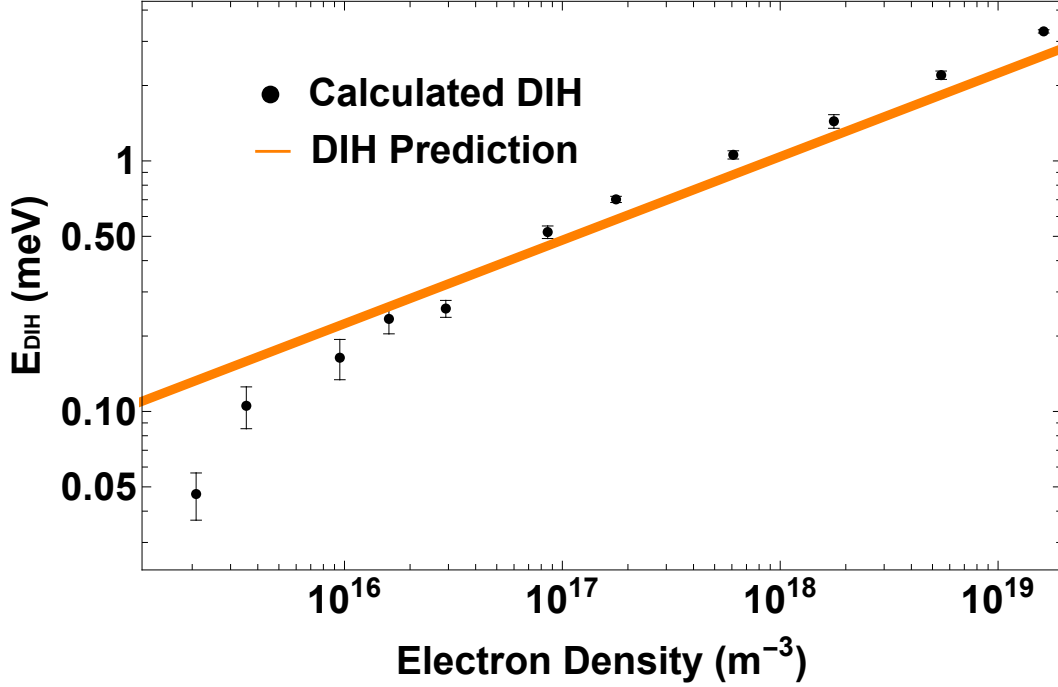
Figure 5.14: Disorder induced heating as calculated from equation 5.2 compared to the result calculated from simulation.

5.5.5 Core Emittance and rms Emittance Contributions from Disorder Induced Heating

From the calculated values of E_{DIH}, we can estimate the expected increase in the core emittance, and rms transverse emittance from DIH alone. This will help determine to what extent the Coulomb hole formation determines the growth in core and rms emittance.

For the core emittance, starting from equation 5.3, the density in x-p_x space at the transverse origin can be calculated assuming a cylindrical beam shape and a Gaussian momentum distribution:

$$\epsilon_c = \frac{\sqrt{2\pi}}{4}\sigma_x \sigma_{p_x} \tag{5.7}$$

80

The initial spread of momenta can be written in terms of the MTE in the standard way:

$$\sigma_{p_x} = \sqrt{\frac{\text{MTE}}{mc^2}} \tag{5.8}$$

For the presented simulations, the initial MTE is 0, but some of the disorder induced heating energy will be released in the transverse phase space, resulting in a non-zero momentum spread. In general, the distribution of the heating will depend on the shape of the beam. However, in the case that the average inter-particle distance is much less than the smallest length scale of the beam, the bulk heating effect will dominate and the edge effects can be ignored. In this approximation, the heating is isotropic and 2/3 of the E_{DIH} will contribute to the MTE of the beam. Assuming that the initial and DIH contributions can be added in quadrature, the core emittance becomes approximately:

$$\epsilon_c \approx \frac{\sqrt{2\pi}}{4}\sigma_x\sqrt{\frac{\text{MTE} + \frac{2}{3}E_{\text{DIH}}}{mc^2}} \tag{5.9}$$

In the case of the dc (NCRF) beamline with 0 meV MTE, the initial transverse size of the beam is 8.2 μm (2.6 μm) and the energy from DIH is 0.65 meV (1.4 meV), so the resulting core emittance due to E_{DIH} is 0.18 nm (0.070 nm).

To compare these results to those found in the previous sections, we must take into account the increase of the core emittance in the mean-field space charge simulation from 0, which is an effect of finite sampling. To do this, we will assume the effects of point-to-point space charge can be added in quadrature to the mean-field core emittance, analogously to equation 5.9 and as is valid for independent rms emittance contributions. With this assumption, the core emittance contribution of point-to-point space charge, $\epsilon_{c,P2P}$, can be found through a quadrature subtraction of the mean-field core emittance from the PMP core emittance. For the dc(NCRF) gun beamline, $\epsilon_{c,P2P}$ at the sample is .27 nm (.12 nm). 67% of $\epsilon_{c,P2P}$ at the sample in the dc case is explained by E_{DIH} (0.27 nm vs 0.18 nm), and in

the rf case, 58% of $\epsilon_{c,P2P}$ at the sample is determined by E_{DIH} (0.12 nm vs 0.070 nm).

For the rms transverse emittance contribution, we will use the intrinsic emittance of the beamline [67]:

$$\epsilon_i = \sigma_x \sqrt{\frac{\text{MTE}}{mc^2}} \tag{5.10}$$

As with the core emittance, adding in 2/3 of the disorder induced heating energy, a modification is made to the intrinsic emittance equation:

$$\epsilon_i \approx \sigma_x \sqrt{\frac{\text{MTE} + \frac{2}{3}E_{\text{DIH}}}{mc^2}} \tag{5.11}$$

In the dc (NCRF) beamline, the intrinsic 90% transverse emittance including E_{DIH} is 0.27 nm (0.11 nm). We will compare this to the quadrature subtraction of the 90% transverse emittance emittance of the mean-field simulation from the PMP simulation, which we will call ϵ_{P2P}. At the emittance minimum, ϵ_{P2P} in the dc (NCRF) beamline is 0.40 nm (0.18 nm). The intrinsic emittance contribution from disorder induced heating in the dc (NCRF) beamline thus accounts for 68% (61%) of ϵ_{P2P}. The remaining difference can be attributed to the effect of large angle scatters which kick particles far from the beam center, seen as the tails of the emittance fraction curve in Fig. 5.8a.

5.6   Warm Beam Comparison

In this section, the same dc and NCRF UED beamlines were simulated using a initial beam MTE of 150 meV. By doing so, weaim to show that the PMP and mean-field methods converge to the same result for a warm photocathode, and that Debye screen effectively mitigates point-to-point effects.

In Figs. 5.15 and 5.18, the spot size evolution is shown for the dc and NCRF UED beamlines respectively each with 150 meV MTE. At this higher MTE, the difference between
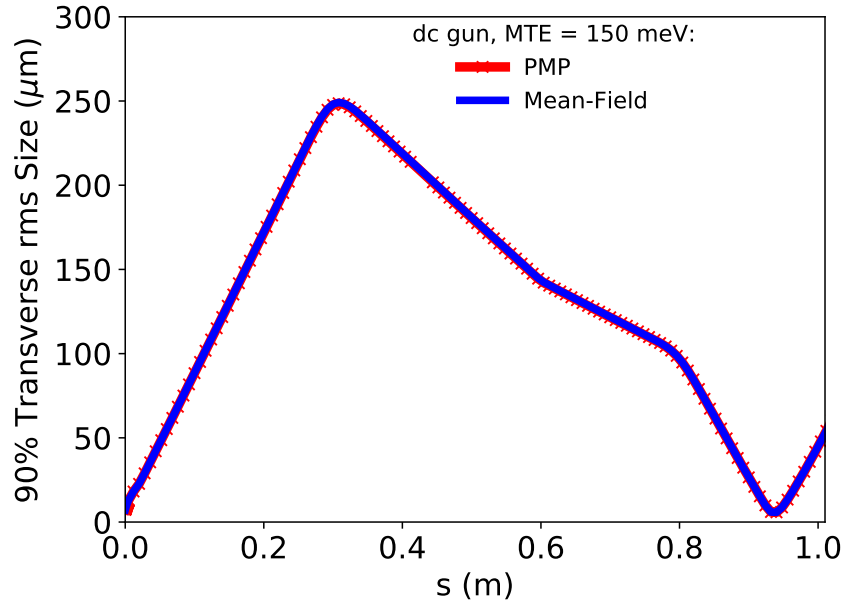
Figure 5.15: Spot size comparison between the PMP method and mean-field space charge simulations of the dc UED beamline with 150 meV MTE.
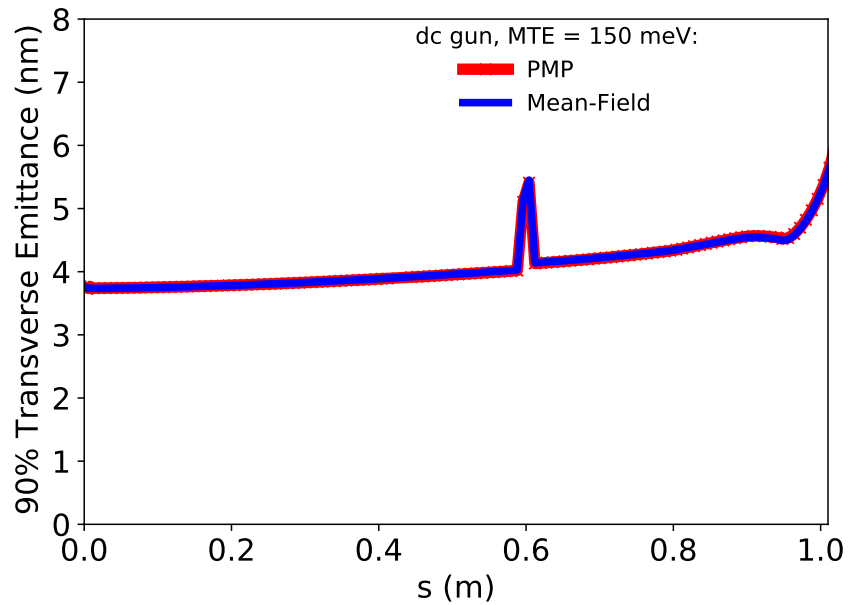
Figure 5.16: Transverse normalized rms emittance comparison between the PMP method and mean-field space charge simulations of the dc UED beamline with 150 meV MTE.
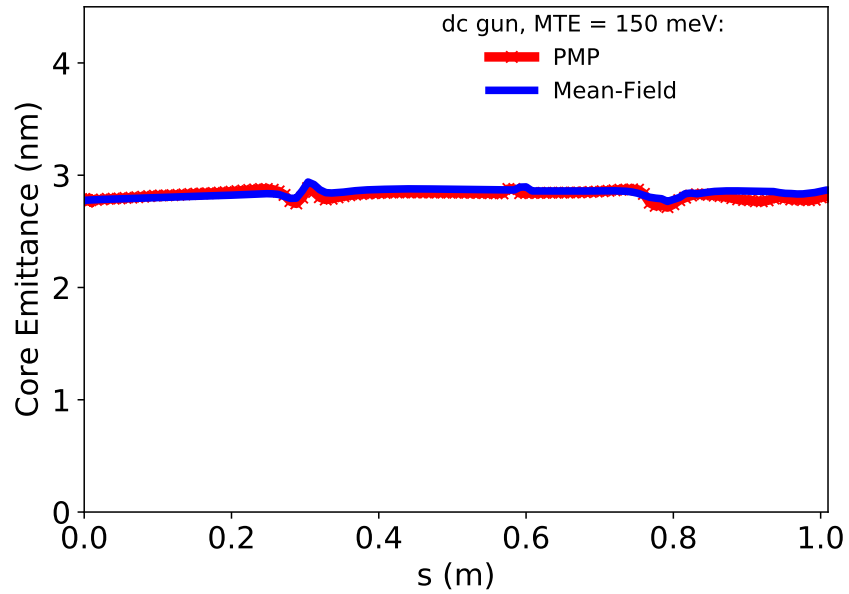
Figure 5.17: Core emittance comparison between the PMP method and mean-field space charge simulations of the dc UED beamline with 150 meV MTE.
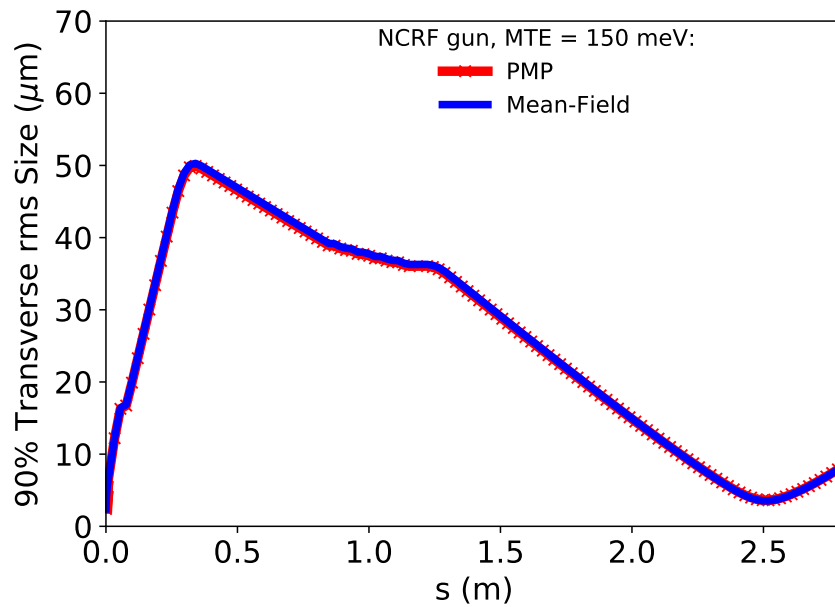
Figure 5.18: Spot size comparison between the PMP method and mean-field space charge simulations of the RF UED beamline with 150 meV MTE.
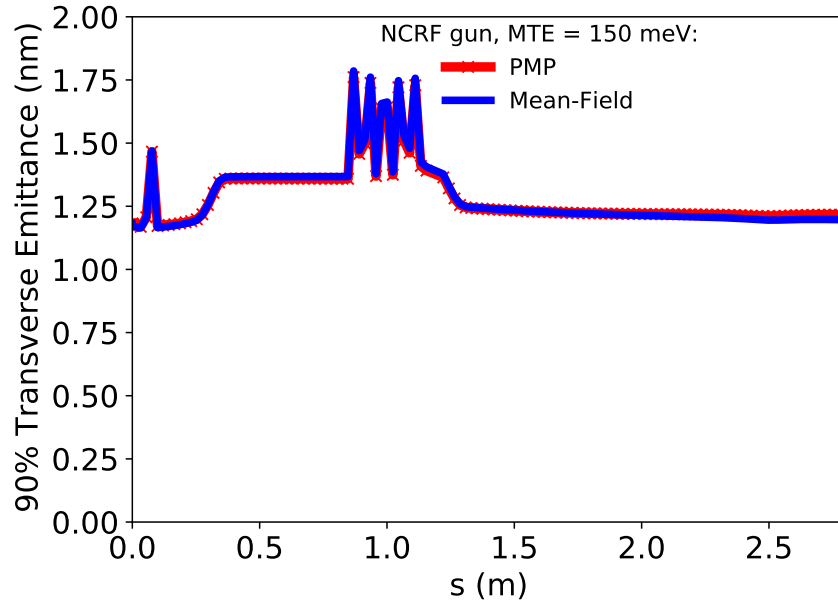
Figure 5.19: Transverse normalized rms emittance comparison between the PMP method and mean-field space charge simulations of the RF UED beamline with 150 meV MTE.
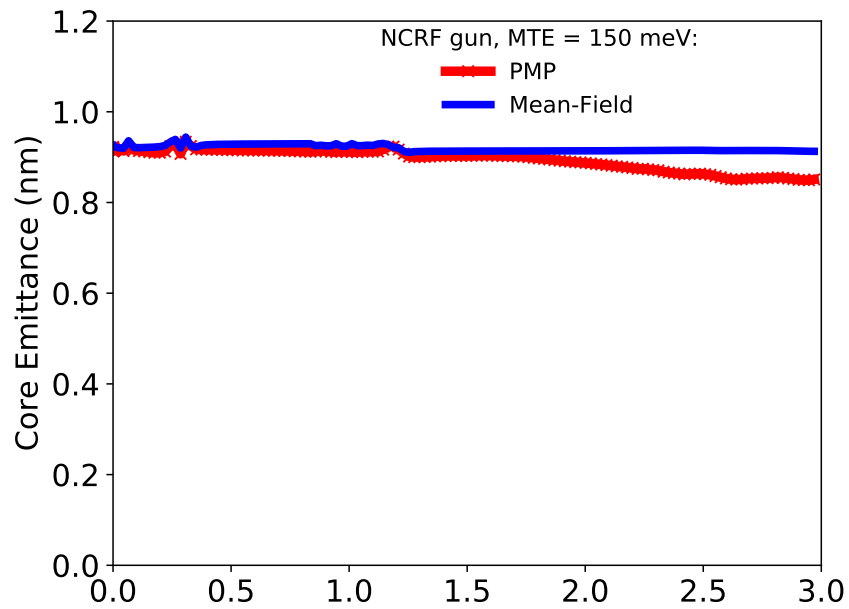
Figure 5.20: Core emittance comparison between the PMP method and mean-field space charge simulations of the RF UED beamline with 150 meV MTE.

the point-to-point and mean-field spot size has been significantly reduced. At the beams maximal size in the first solenoid, the deviation has been reduced from around 2 μm to .7 μm in the dc beamline and 1.2 μm to .5 μm in the NCRF beamline.

The evolution of the transverse rms emittance for the dc and NCRF beamlines is shown in Figs. 5.16 and 5.19 respectively. With an MTE of 150 meV, there is no significant deviation in the transverse rms emittance between the implementations of space charge as observed at 0 meV. This validates that phtocathodes with high emission temperatures can be successfully modelled without consideration of point-to-point space charge effects.

The evolution of the core emittance at an MTE of 150 meV is shown in Figs. 5.17 and 5.20 for the dc and NCRF UED beamlines respectively. Outside of fluctuations near the solenoids the core emittance in all simulations are approximately constant. No significant difference exists between the core emittance between point-to-point and mean-field simulations at 150 meV.

5.7   Modified Image Charge Method

The majority of this chapter employs a mean-field model of the image force. In this section, we show this to be a valid approximation. To do this, we analytically investigate a point-like image model and compare it to PMP.

We first aim to show that for particles much closer to the cathode compared to the average interparticle distance, the Coulombic repulsion force will be predominantly longitudinal, as the transverse fields from other charges and their images will largely cancel.

The transverse electric field from an electron a distance d away from an infinite conducting plane and its image charge in cylindrical coordinates is given by:

$$E_r = \frac{1}{4\pi\epsilon_0} \left(\frac{-er}{(r^2 + (z-d)^2)^{3/2}} + \frac{er}{(r^2 + (z+d)^2)^{3/2}} \right) \tag{5.12}$$

We first will consider the effects of particles far away from the cathode on particles which are recently emitted. At a position much closer to the cathode ($z \ll d$), this expression is approximately:

$$E_r \approx \frac{1}{4\pi\epsilon_0} \frac{-3ezrd}{2(r^2 + d^2)^{5/2}} \tag{5.13}$$

We compare this to the longitudinal field in cylindrical coordinates:

$$E_z = \frac{1}{4\pi\epsilon_0} \left(\frac{-e(z-d)}{(r^2 + (z-d)^2)^{3/2}} + \frac{e(z+d)}{(r^2 + (z+d)^2)^{3/2}} \right) \tag{5.14}$$

In the same limit, $z \ll d$:

$$E_z \approx \frac{1}{4\pi\epsilon_0} \frac{2ed}{(r^2 + d^2)^{3/2}} \tag{5.15}$$

The magnitude of the ratio of the transverse and longitudinal electric fields in this limit of $z \ll d$ is:

$$\left| \frac{E_r}{E_z} \right| \approx \frac{3zr}{4(r^2 + d^2)} \tag{5.16}$$

This ratio tends to 0 for small or large r and has a maximum at $r = d$ of:

$$\left| \frac{E_r}{E_z} \right|_{max} \approx \frac{3z}{8d} \tag{5.17}$$

Because $z \ll d$ the transverse electric field will be much smaller than the longitudinal field, and thus proving the Coulombic repulsion force will be predominantly longitudinal.

For an electron beam with an average interparticle distance a, this will apply as long as $a \gg$ d. Therefore, for particles that have just been emitted, if we are to model the effects of the cathode and to avoid divergent fields for small z, we can ignore transverse effects, and only need to find the time it takes for a particle to travel a longitudinal distance on the order of the interparticle distance, and its energy at that point.

From dynamical image charge theory, a semi-classical image potential can be computed

[92], in the approximation that the electron has no velocity parallel to the conducting surface, the potential energy V is:

$$V(v, z) = -\frac{1}{4\pi\epsilon_0} \frac{e^2 \omega_p^2}{4v\omega_s} f\left(\frac{2z\omega_s}{v}\right),$$

$$f(x) = \int_0^\infty \frac{e^{-\alpha x}}{1+\alpha^2} d\alpha$$

(5.18)

where ω_p is the plasma frequency of the material, $\omega_p^2 = 2\omega_s^2$, v is the velocity of the electron, and z is its distance from the cathode.

The energy of an electron moving at a velocity v a distance z from the cathode with an applied electric field E_z is thus:

$$E = \frac{mv^2}{2} - \frac{1}{4\pi\epsilon_0} \frac{e^2 \omega_p^2}{4v\omega_s} f\left(\frac{2z\omega_s}{v}\right) - eE_z z$$

(5.19)

The applied electric field will consist of the field from the gun as well as an approximation to the longitudinal effects of other particles. The field from the particles in front of a given particle will be approximated as a uniformly charged cylinder with a transverse size, R, equal to that of the beam, and longitudinal size, L, equal to the initial bunch length multiplied by the beam fraction that has left the cathode previously. The image charge contribution from other particles will be approximated as a positively charged cylinder with equal dimensions placed directly behind the particle. With this, the equation for the applied electric field on the jth particle emitted is:

$$E_z(j) = E_{gun}(z) + \frac{e(j-1)}{\pi R^2 \epsilon_0} \left(1 + \frac{R}{L(j)} - \sqrt{1 + \frac{R^2}{L(j)^2}}\right)$$

(5.20)

where $L(j)$ is the length of the bunch in front of the jth particle.

These equations can be self-consistently solved to find the velocity and potential at any longitudinal position for a given energy E. Calculating the velocity at several locations near

the cathode, the time it takes to reach a given distance can be calculated as well. Because the transverse effects of space charge can be ignored in this regime, the external transverse field near the cathode can be used to approximate the transverse position of particle at a later distance, although we find this effect to be insignificant for the cases considered in this manuscript.

With this information, the beam can be initialized in simulation at a position away from the cathode divergence and thereafter can be modeled using a standard, point-like image charge method. As long as the position is chosen to be sufficiently far from the cathode and less than the average particle distance, the resulting simulation should not depend heavily on the starting distance choice.
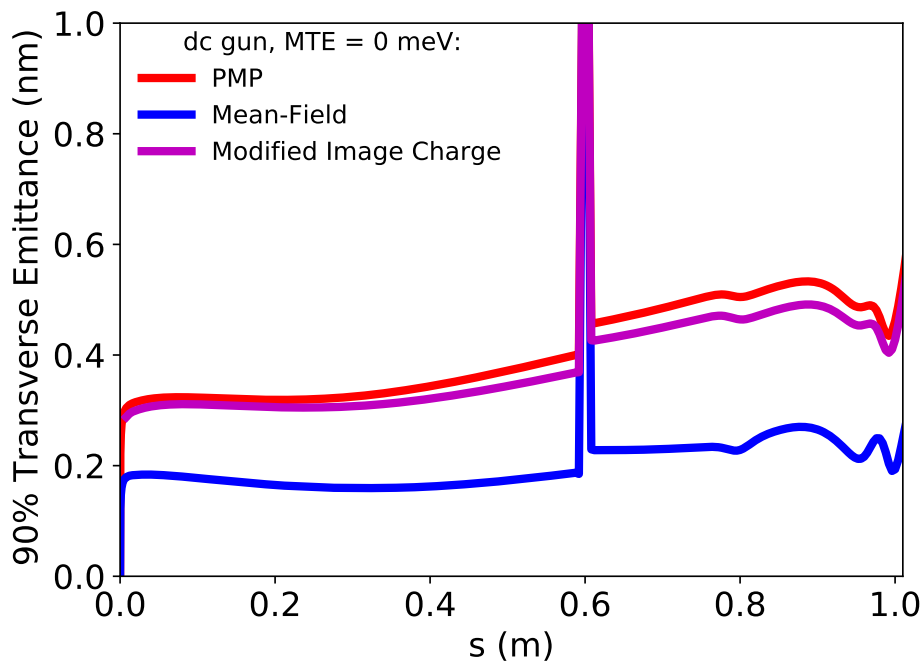
Figure 5.21: Transverse normalized rms emittance comparison for point-to-point, mean-field, and modified image charge simulations of the dc UED beamline with 0 meV MTE.

Through this analysis, we have shown that the image charges have little effect on the transverse dynamics of particles until a distance away from the cathode on the order of the average interparticle distance. Because point-to-point effects are most important for interac-
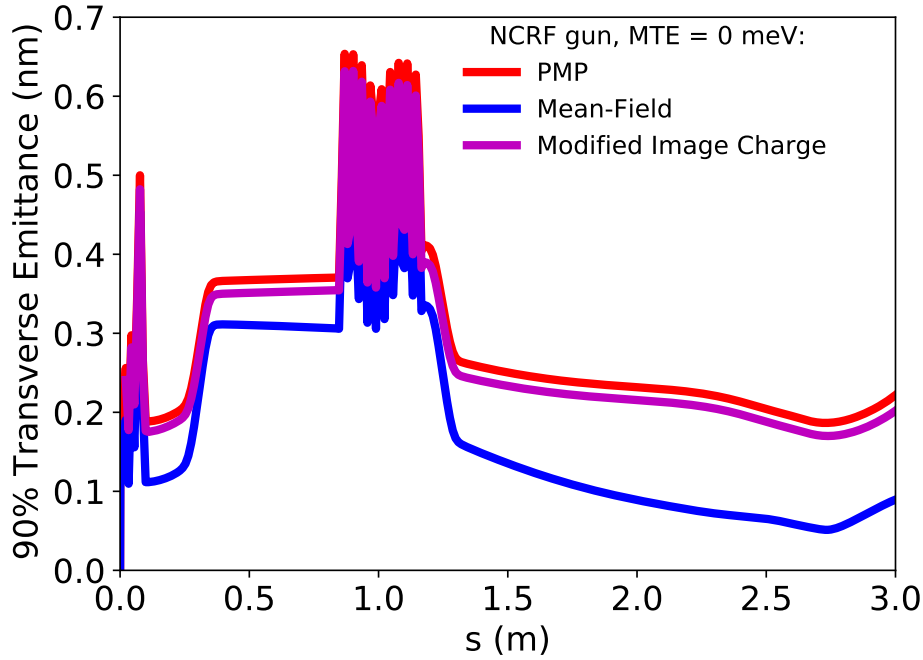
Figure 5.22: Transverse normalized rms emittance comparison for point-to-point, mean-field, and modified image charge simulations for the NCRF UED beamline with 0 meV MTE.

tions at a distance less than the average interparticle distance, a mean-field implementation of the image charge, such as is done through the PMP method used in this chapter, should produce correct results as long as the energy modulation of the produced particles by their images is correct.

In Figs. 5.21 and 5.22, the 0 meV MTE transverse normalized rms emittance results for the DC and NCRF beamline are shown respectively, now including results from the modified image charge method discussed in this section. E was chosen such that the minimum kinetic energy of an electron was 5 meV, on the order of the smallest MTE measured today. The particles were started at a distance 0.5 μm away from the cathode. Deviations in the emittance from the PMP method are less than 10% throughout the simulations.

5.8   Summary and Outlook

In this chapter, I have shown that as photoemitted electron beam temperatures are made ever smaller, the effects of the point like nature of the Coulomb interaction become crucial to understanding photoinjector beam dynamics. We have introduced and benchmarked a simple method to compute the image force in a point-to-point beam dynamics simulations free of divergences and additional tuning parameters. Using this method, we have quantified Coulomb scattering effects on the beam phase space density in two UED beamline archetypes. Using a photocathode with zero intrinsic emittance, the emittance of the beam in both the rf and dc UED beamlines studied was larger by a factor of at least 2, see Figs. 5.5b and 5.6b, and the core emittance is larger by a factor of at least 3, see Figs. 5.9 and 5.10, when compared to simulation on the same beamline but assuming mean-field space charge. In addition, the energy released by disorder induced heating was calculated using the radial distribution function, and the heating was found to scale with the density to the power of 0.39 ± 0.03, close to the a simple theoretical estimate of $1/3$, and was shown to be the dominant effect in both core and 90% rms emittance growth. We found disorder induced heating contributed to the emittance of the beamlines studied as shown in equation 5.11.

CHAPTER 6

CONCLUSION

Ultrafast electron diffraction is one of the prominent tools used in current studies of ultrafast science. The use of electrons as a probe is both a blessing and a curse, as their strong interaction with the samples they probe comes at a cost of the electrons strongly interacting with each other. Managing the trade-off between the degrading effects of space charge and producing resolved images on a human timescale is a quintessential issue in designing a UED beamline.

The spatial resolution of the images is determined by the transverse emittance, which is close to a conserved quantity. The minimum emittance of a UED beamline is set by the quality of the electron source. However, the quality of the electron source does not matter if the emittance of the electron beam is not preserved to the sample being studied. Three causes of emittance dilution, longitudinal-transverse coupling, non-linear forces, and divergent forces in particular are relevant for UED beamlines.

Non-linear forces in UED beamlines come from two main sources, space charge and stray fields. The effects of these fields disproportionately impact larger beams, which counter-intuitively impact UED beamlines which want to diffraction over smaller areas the most. The non-linearity of space charge can be mitigated through careful shaping or clipping of the electron beam or by going to higher energies. Stray fields coming from the beamline elements can be corrected by precisely designing elements to cancel these fields.

To improve the performance of UED beamline operating in the micro-diffraction regime, a series of corrector magnets up to the sextupole moment were created and installed into the MEDUSA beamline. The inclusion of the sextupole corrector reduced the emittance of the stray field corrected beamline by 25% compared to the non-corrected beam and was properly modeled as a beamline which had no stray fields.

The divergent nature of the Coulomb interaction is most pronounced in cold dense elec-

tron beams, where electrons which are close to each other, remain close for longer periods of time. A cold dense beam however has a very large peak brightness, which is necessary for UED of non-reversible processes. To produce cold dense electron beams, photocathodes are being developed with very low MTE. While the emittance of very low MTE photocathodes can be mostly conserved in simulation, the mean-field approximation used in those simulations is no longer valid, bringing the results of those simulations into question.

Multiple methods were developed and validated against each other for the fast approximation of a Coulomb interaction which is mean-field at long distances and exact at short distances in the presence of a photocathode. Using these tools, the evolution of the emittance of an electron beam in different UED beamlines designs was simulated. For typical densities used in single shot UED, I found that the emittance of simulated electron beams can grow to be over twice what is predicted in mean-field simulations, and is properly modeled by the temperature growth in a stationary electron ball with random initialized positions.

The future of UED depends on the development of high brightness electron sources and beamlines which can preserve the electron beam quality. Different ultrafast phenomena will have varying requirements on beam size, emittance, and brightness needed for their study. For stricter requirements, the magnitudes of different beam degradation effects can become important. The next effect that will be important to correct in UED is thus linked to the question, what do people want to study next?

APPENDIX A

WAKEFIELD CALCULATION WITH A RECTANGULAR

DIELECTRIC BOUNDARY

This appendix will discuss my work in the fast computation of the wakefield generated from a rectangular beam pipe with one pair of outer walls coated with a thick layer of a dielectric material, see figure A.1 taken from [106].
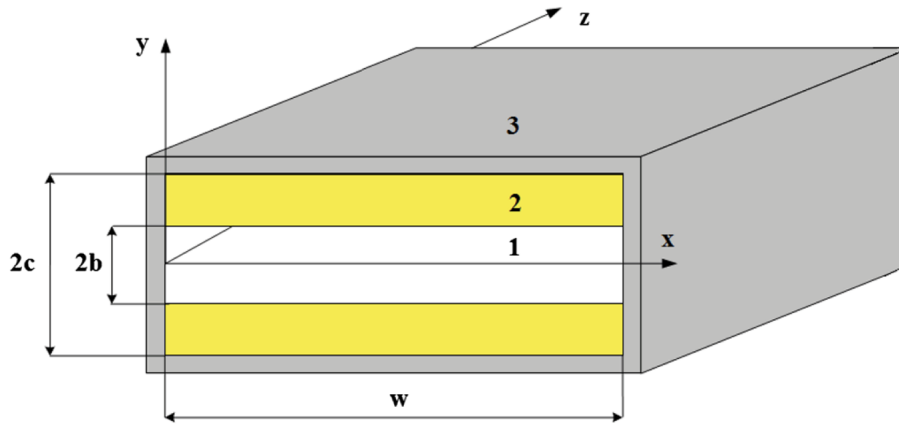
Figure A.1: Rectangular beam pipe with dielectric coating one set of opposite walls, the three marked areas indicate (1) vacuum, (2) dielectric, and (3) conducting wall.

To simulate the effects on particles travelling through this structure, it is necessary to solve for the wakefields from all particles traveling through the structure and apply those fields to the trailing particles. The full solution to this problem involve the solving of an eigenfunction/eigenvalue problem which can be found in [106]. The solutions for the eigenvalues are in the form of transcendental equations like the following:

$$\mu_1 k_{ch}^H \tanh(k_{ch}^H b) + k_{md}^H \cot(k_{md}^H(c - b)) = 0$$

where:

$$k_{ch}^H = \sqrt{(1 - \beta^2)\lambda_H + k_x^2}$$

$$k_{md}^H = \sqrt{(\epsilon_1 \mu_1 \beta^2 - 1)\lambda_H - k_x^2)}$$

$$k_x = \pi n/w$$

Here ϵ_1 and μ_1 represent the permittivity and permeability of a dielectric inserted into a waveguide. b,c, and w are parameters controlling the size of the waveguide and dielectric. n is a positive integer to be iterated over. β is the relativistic velocity of the bunch of particles traveling through the waveguide. Lastly λ_H is the eigenvalue that is being solved for. Thus the problem of calculating the effect of these wakefields begins with the calculations of the roots of these functions.

These equations are almost periodic and have an infinite number of discontinuities. β for ultra relativistic particles is very close to 1 which can remove dependence of λ_H from k_{ch}^H. The ratio of $\frac{cn}{w}$ determines how compressed the roots are, and the range of parameters is quite large: $10^{-3} < c/w < 10^3$. All of these properties cause many issues in normal fast root finders. Thus it is necessary to develop a quick root finder that can deal with this class of equations.

The root finder exploits the near periodic nature of the function to make intelligent guesses at where the next root will be found. By rescaling the function, the n dependence of the roots can be mostly removed, further allowing the root finder to take solutions for previously calculated values of n and use them to quickly calculate the roots for higher n. A schematic of the root finding algorithm can be seen in fig. A.2

After a sufficient number of eigenvalues are collected from a desired number of modes, the fields generated from the particles can be found through a summation of eigenfunctions using these found eigenvalues.

The transverse and longitudinal force from a particle with $x > 0, y = 0$ using this method on a trailing test particle with equal transverse coordinates are shown in figs. A.3 and A.4 respectively. The force in the y direction for this position is 0 from symmetry. From these

95

Initialization and Function Choice

Begin Loop Over n

Check Value of n

n =1   n =2   n >= 3

Use Standard Step Size and Start Position

Use Standard Step Size and Dynamic Start Position

Use Dynamic step size and start position based on previous 2 n

Step Forward Until Proper Change of Sign

Reset starting position and reduce step size

Apply Bisection Method

Set Standard or Dynamic Step Size and Starting Position

n>1

Bad

n =1

Compare to same root of n-1

1st Root Found

Good

Save Root

2nd Root Found
Loop over Remainder of roots

Set Dynamic Step Size and Starting Position Based on Previous Roots

Step Forward Until Proper Change of Sign

Need More Roots

Apply Bisection Method

Save Root

Done with Current n

Repeat with n++

Rescale Roots

Figure A.2: Root-finding method for the calculation of the eigenvalues for the dielectric wakefield problem.

images, the force generated is seen to be defocusing transversely and longitudinally. Particles trailing the lead particle will be kicked farther from the beam axis and be decelerated.
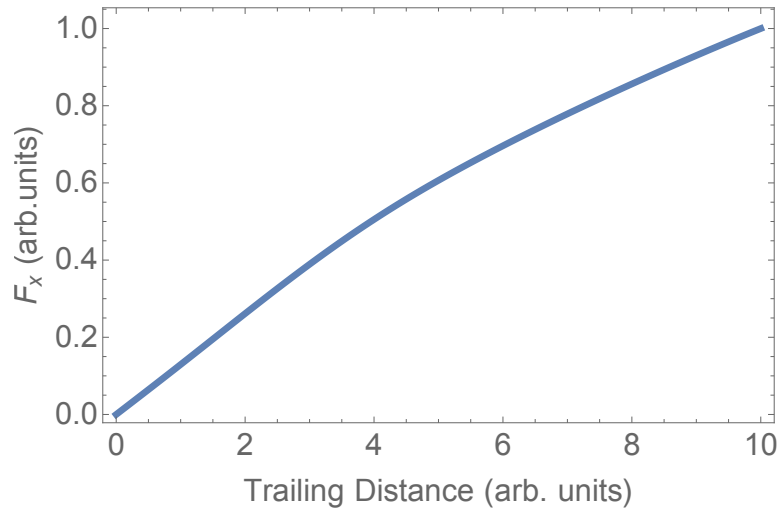
Figure A.3: Transverse force on a test particle trailing a particle with $x > 0$ and $y = 0$ in the dielectric structure.
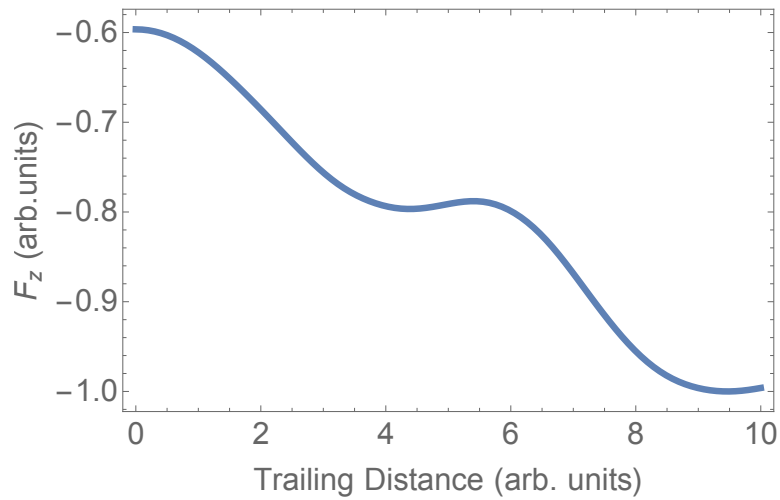
Figure A.4: Longitudinal force on a test particle trailing a particle with $x > 0$ and $y = 0$ in the dielectric structure.

APPENDIX B

EMITTANCE COMPENSATION IN APPLICATION

The following subsection is based on work done in [107] and presented at the International Particle Accelerator Conference 2018.

In [94], MOGA was applied to 3D space charge simulations (using General Particle Tracer (GPT) [91]) of the cryogun beamline under commissioning at Cornell in order to determine the limitations of the emittance performance from an extremely low MTE cathode. This setup features a 225kV DC gun housing a cryogenically cooled cathode with an (projected) MTE of 5 meV and a 3 GHz normal conducting buncher cavity field map between two solenoid magnets. The intended sample location is located at roughly 1 m from that cathode (the exact position varies slightly among the different optimized solutions). A typical field profile is shown in Fig. B.1.
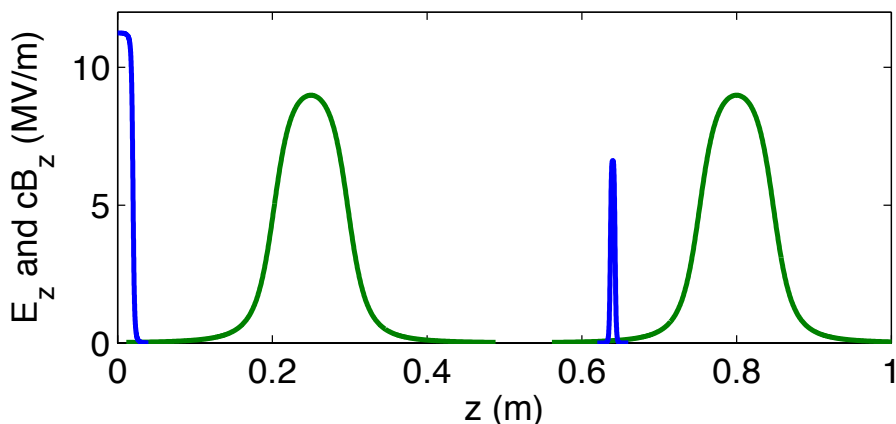
Figure B.1: Generic on-axis electric field E_z (blue) and solenoid field B_z (green) profiles for the cryogun set-up. The intended sample location is at roughly 1 m.

In all simulations, the optimizer varied the beamline parameters, element positions, and arbitrarily shaped both the transverse and longitudinal laser distributions. The resulting optimal emittance as a function of bunch charge is shown in Fig. B.2. I will focus on two example cases from this front corresponding to charges of 10^5 and 10^6 electrons. For
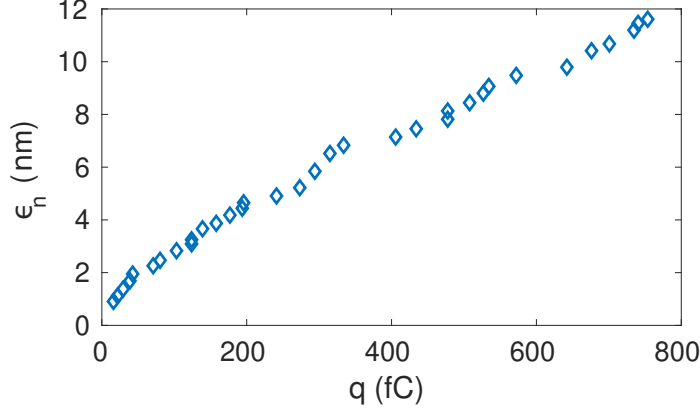
Figure B.2: The optimal emittance as a function of bunch charge at the sample location (roughly 1m).

these examples the corresponding intended sample locations are 1.0 m and 0.95 m from the cathode. The initial/final emittance at the sample location was 0.33/0.81 (0.89/5) nm for the 10^5 (10^6) bunch charges, corresponding to an emittance growth of 145%, and 460%, respectively.

In analyzing the emittance growth in the two example beamlines, I will consider two contributions, slice misalignment, and slice size mismatch. Here, misalignment refers to the spread of the slopes in the transverse phase spaces (p_x vs. x and p_y vs. y), while mismatch refers to differences in the rms sizes in each phase space coordinate. Fig. B.3 shows the combined effect of these two contributions by plotting the ratio of the full emittance to the average slice emittance. 50 longitudinal slices were used in this calculation. In the 10^5 electron case, the emittance grows substantially compared to the average slice emittance, however this is nearly completely compensated. The situation is different for the 10^6 electron example, where the ratio grows quickly at the beginning and then is partially compensated at the end of the beamline. The failure to restore all of the emittance in the beam is due to the strong non-linear space charge forces in the electron beam.

In order to determine the lowest possible emittance from ideal linear emittance compensation, the extent of slice mismatch and slice misalignment at the end of the beamline have
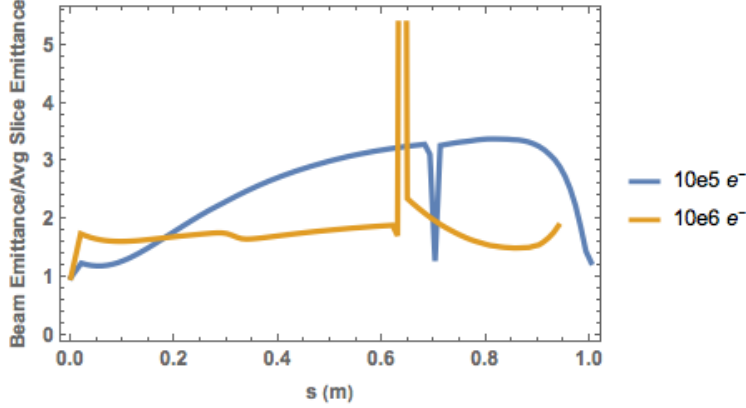
Figure B.3: Ratio of the beam emittance to the average slice emittance (50 slices) for the two example charges.

been computed. To do this, the final beam was sliced into 50 longitudinal slices of equal length and the x-p_x and y-p_y correlations calculated. The values of p_x and p_y of each particle were then adjusted to remove the individual slice slope. Next, the spreads in position and momentum were calculated for the slices, as well as the full beam. The spread in position space of each slice was then replaced by the spread in position space of the beam. The spread in momentum space was then proportionally changed for each slice to preserve individual slice emittance. Lastly, each particle's p_x and p_y were changed to make each slice's slope equal to the beam slope.

Before applying this method, the transverse emittance of the beam in the 10^5 (10^6) electron case was 0.858 nm (4.90 nm) at the end of the beamline. After the removal of slice effects, this was reduced to 0.727 nm (2.73 nm). This corresponds to a 15.4% (44.4%) reduction of the final beam emittance if these effects could be removed. This is consistent with fig. B.3 which at the end of the beamline shows the slice emittance is 17% (47%) smaller than the beam emittance, showing that in application, it is difficult to fully restore emittance lost to longitudinal correlations in the beam.

APPENDIX C

DISPLACED IMAGE CHARGE METHOD

An alternative simulation method for including the effects of image effects without divergence may be preferable in cases where mean-field image forces are not accessible for the PMP method, but the more exact method is too computationally expensive. In this case, a simplified model of point-like images can be used, with one tuning parameter to be chosen, related to the final energy of the beam.

This method relies on a displaced image charge method, schematically shown in fig. C.1. In this model, the electron is always assumed to start at a distance r_c away from the cathode. In implementation, this means that the an image charge is placed for each electron at a distance $2r_c$ further back from the cathode than the distance from the cathode to the electron.
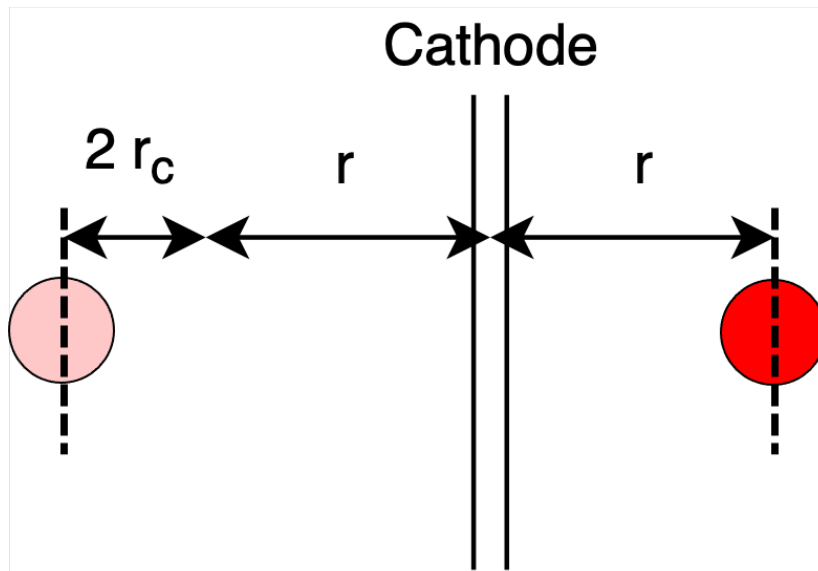
Figure C.1: Diagrammatic representation of the displaced image charge method. An electron is further displaced from its positively charged image by an additional distance, $2r_c$.

The justification of this model follows that done in section 5.7. The main difference being, in this method you choose a distance scale based on the final desired energy of the electron

beam, while skipping the mathematically taxing computation. In this sense the method is easier to work with, but holds less predictive power than the other methods. With an r_c chosen to match the energies predicted in the PMP and modified image charge method, the simulation results are unchanged from the other methods.

For these reasons it is suggested that this method be used only when a value of r_c can be determined from either experimental deviations in the measurements of the beam size at distances far from the cathode compared to a mean-field prediction, or with a theoretical estimation of the expected energy loss from the image potential. Coming up with a heuristic choice for a value of r_c is a topic of future work.

REFERENCES

[1] Hugh T. Philipp, Mark W. Tate, Katherine S. Shanks, Luigi Mele, Maurice Peemen, Pleun Dona, Reinout Hartong, Gerard van Veen, Yu-Tsun Shao, Zhen Chen, Julia Thom-Levy, David A. Muller, and Sol M. Gruner. Very-high dynamic range, 10,000 frames/second pixel array detector for electron microscopy, 2021.

[2] Krystel El Hage, Sebastian Brickel, et al. Implications of short time scale dynamics on long time processes. *Structural Dynamics*, 4(6):061507, 2017.

[3] K. Parlinski. Lattice dynamics: Vibrational modes. In Franco Bassani, Gerald L. Liedl, and Peter Wyder, editors, *Encyclopedia of Condensed Matter Physics*, pages 98–102. Elsevier, Oxford, 2005.

[4] Majed Chergui and Ahmed H. Zewail. Electron and x-ray methods of ultrafast structural dynamics: Advances and applications. *ChemPhysChem*, 10(1):28–43, 2009.

[5] John C. H. Spence. Outrunning damage: Electrons vs x-rays timescales and mechanisms. *Structural Dynamics*, 4(4):044027, 2017.

[6] Jie Yang, Xiaolei Zhu, J. Pedro F. Nunes, Jimmy K. Yu, Robert M. Parrish, Thomas J. A. Wolf, Martin Centurion, Markus GÃŒhr, Renkai Li, Yusong Liu, Bryan Moore, Mario Niebuhr, Suji Park, Xiaozhe Shen, Stephen Weathersby, Thomas Weinacht, Todd J. Martinez, and Xijie Wang. Simultaneous observation of nuclear and electronic dynamics by ultrafast electron diffraction. *Science*, 368(6493):885–889, 2020.

[7] J. Yang, Nunes Dettori, R., J.P.F., et al. Direct observation of ultrafast hydrogen bond strengthening in liquid water. *Nature*, 596:531–535, 2021.

[8] A A Ishchenko, S A Aseyev, V N Bagratashvili, V Ya Panchenko, and E A Ryabov. Ultrafast electron diffraction and electron microscopy: present status and future prospects. *Physics-Uspekhi*, 57(7):633–669, jul 2014.

[9] A. Einstein. Über einen die erzeugung und verwandlung des lichtes betreffenden heuristischen gesichtspunkt. *Annalen der Physik*, 322(6):132–148, 1905.

[10] Jeff Hecht. Short history of laser development. *Optical Engineering*, 49(9):1 – 23, 2010.

[11] Alan Chodos. November 8, 1895: Roentgen's discovery of x-rays. *APS News*, 10(10), 2001.

[12] Tetsuya Ishikawa. Accelerator-based x-ray sources: synchrotron radiation, x-ray free electron lasers and beyond. *Philosophical Transactions of the Royal Society A: Mathematical, Physical and Engineering Sciences*, 377(2147):20180231, 2019.

[13] S. P. Weathersby, G. Brown, et al. Mega-electron-volt ultrafast electron diffraction at slac national accelerator laboratory. *Review of Scientific Instruments*, 86(7):073702, 2015.

[14] S. D. Brorson, J. G. Fujimoto, and E. P. Ippen. Femtosecond electronic heat-transport dynamics in thin gold films. *Phys. Rev. Lett.*, 59:1962–1965, Oct 1987.

[15] Richard Henderson. The potential and limitations of neutrons, electrons and x-rays for atomic resolution microscopy of unstained biological molecules. *Quarterly Reviews of Biophysics*, 28(2):171–193, 1995.

[16] S. Williamson, G. Mourou, and J. C. M. Li. Time-resolved laser-induced phase transformation in aluminum. *Phys. Rev. Lett.*, 52:2364–2367, Jun 1984.

[17] A. Rahman and I. K. Schuller. Inelastic electron-phonon scattering and time-resolved laser-induced phase transformation in aluminum. *Phys. Rev. Lett.*, 55:1939–1939, Oct 1985.

[18] H. E. Elsayed-Ali and G. A. Mourou. Picosecond reflection high-energy electron diffraction. *Applied Physics Letters*, 52(2):103–104, 1988.

[19] J.C. Williamson, M. Dantus, S.B. Kim, and A.H. Zewail. Ultrafast diffraction and molecular structure. *Chemical Physics Letters*, 196(6):529–534, 1992.

[20] Bradley J. Siwick, Jason R. Dwyer, Robert E. Jordan, and R. J. Dwayne Miller. An atomic-level view of melting using femtosecond electron diffraction. *Science*, 302(5649):1382–1385, 2003.

[21] Jianming Cao, Xuan Wang, and Dongping Zhong. Mapping the structural dynamics of water dissociation. *Science*, 374(6563):34–35, 2021.

[22] Hari Padmanabhan, Maxwell Poore, Peter K. Kim, et al. Interlayer magnetophononic coupling in mnbi2te4. *Nature Communications*, 13(1):1929, 2022.

[23] E. G. Champenois, D. M. Sanchez, J. Yang, J. P. Figueira Nunes, et al. Conformer-specific photochemistry imaged in real space and time. *Science*, 374(6564):178–182, 2021.

[24] Mianzhen Mo, Minxue Tang, Zhijiang Chen, J. Ryan Peterson, Xiaozhe Shen, et al. Ultrafast visualization of incipient plasticity in dynamically compressed matter. *Nature Communications*, 13(1):1055, 2022.

[25] B. Q. Lv, Alfred Zong, D. Wu, A. V. Rozhkov, Boris V. Fine, Su-Di Chen, et al. Unconventional hysteretic transition in a charge density wave. *Phys. Rev. Lett.*, 128:036401, Jan 2022.

[26] Diego Turenne, Alexander Yaroslavtsev, Xiaocui Wang, Vivek Unikandanuni, Igor Vaskivskyi, et al. Nonequilibrium sub–10 nm spin-wave soliton formation in fept nanoparticles. *Science Advances*, 8(13):eabn0523, 2022.

[27] Weronika O. Razmus, Kyle Acheson, Philip Bucksbaum, Martin Centurion, Elio Champenois, et al. Multichannel photodissociation dynamics in cs2 studied by ultrafast electron diffraction. *Phys. Chem. Chem. Phys.*, 24:15416–15427, 2022.

[28] John David Jackson. *Classical electrodynamics; 2nd ed.* Wiley, New York, NY, 1975.

[29] H. Wiedemann. *Particle Accelerator Physics.* SpringerLink: Springer e-Books. Springer Berlin Heidelberg, 2007.

[30] Vinit Kumar. Understanding the focusing of charged particle beams in a solenoid magnetic field. *American Journal of Physics*, 77(8):737–741, 2009.

[31] Kwang-Je Kim. Rf and space-charge effects in laser-driven rf electron guns. *Nuclear Instruments and Methods in Physics Research Section A: Accelerators, Spectrometers, Detectors and Associated Equipment*, 275(2):201–218, 1989.

[32] Alex Chao. Beam Dynamics of Collective Instabilities in High Energy Accelerators. *CERN Yellow Rep. School Proc.*, 3:43, 2017.

[33] T. Tajima and J. M. Dawson. Laser electron accelerator. *Phys. Rev. Lett.*, 43:267–270, Jul 1979.

[34] Giuseppe Dattoli, Andrea Doria, Elio Sabia, and Marcello Artioli. *Charged Beam Dynamics, Particle Accelerators and Free Electron Lasers.* 2053-2563. IOP Publishing, 2017.

[35] S.B. van der Geer, O.J. Luiten, M.J. de Loos, and U. van Rienen G. Pöplau. A fast 3d multigrid based space-charge routine in the gpt code. 01 2002.

[36] Los Alamos Accelerator Code Group. A compendium of computer codes used in particle accelerator design and analysis. *AIP Conference Proceedings*, 184(2):1137–1326, 1989.

[37] R L Mills and A M Sessler. Liouville's theorem and phase-space cooling. 9 1993.

[38] Klaus Floettmann. Some basic features of the beam emittance. *Phys. Rev. ST Accel. Beams*, 6:034202, Mar 2003.

[39] David H. Dowell. Correcting emittance growth due to stray sextupole fields, September 2018.

[40] B. E. Carlsten. Space-charge-induced emittance compensation in high-brightness photoinjectors. *Nuclear Instruments and Methods in Physics Research*, Sept 1994.

[41] P. Musumeci, J. Giner Navarro, J.B. Rosenzweig, L. Cultrera, I. Bazarov, J. Maxson, S. Karkare, and H. Padmore. Advances in bright electron sources. *Nuclear Instruments and Methods in Physics Research Section A: Accelerators, Spectrometers, Detectors and Associated Equipment*, 907:209 – 220, 2018. Advances in Instrumentation and Experimental Methods (Special Issue in Honour of Kai Siegbahn).

[42] Arnaud Arbouet, Giuseppe M. Caruso, and Florent Houdellier. Chapter one - ultra-fast transmission electron microscopy: Historical development, instrumentation, and applications. In Peter W. Hawkes, editor, *Advances in Imaging and Electron Physics*, volume 207 of *Advances in Imaging and Electron Physics*, pages 1–72. Elsevier, 2018.

[43] W. H. Li, C. J. R. Duncan, M. B. Andorf, A. C. Bartnik, E. Bianco, L. Cultrera, A. Galdi, M. Gordon, M. Kaemingk, C. A. Pennington, L. F. Kourkoutis, I. V. Bazarov, and J. M. Maxson. A kiloelectron-volt ultrafast electron micro-diffraction apparatus using low emittance semiconductor photocathodes. *Structural Dynamics*, 9(2):024302, 2022.

[44] M. Chergui. 1.19 ultrafast structural dynamics of biological systems. In Edward H. Egelman, editor, *Comprehensive Biophysics*, pages 398–424. Elsevier, Amsterdam, 2012.

[45] Jason R Dwyer, Christoph T Hebeisen, Ralph Ernstorfer, Maher Harb, Vatche B Deyirmenjian, Robert E Jordan, and R.J Dwayne Miller. Femtosecond electron diffraction: ‘making the molecular movie’. *Philosophical Transactions of the Royal Society A: Mathematical, Physical and Engineering Sciences*, 364(1840):741–778, 2006.

[46] R. Shankar. *All Is Not Well with Classical Mechanics*, pages 107–113. Springer US, New York, NY, 1994.

[47] G. Chartier, A. AC04630632], and Inc Books24x7. *Introduction to Optics*. Advanced Texts in Physics. Springer, 2005.

[48] N.W. Ashcroft and N.D. Mermin. *Solid State Physics*. Cengage., 2021.

[49] O. J. Luiten, S. B. van der Geer, M. J. de Loos, F. B. Kiewiet, and M. J. van der Wiel. How to realize uniform three-dimensional ellipsoidal electron bunches. *Phys. Rev. Lett.*, 93:094802, Aug 2004.

[50] M. Gordon, W. H. Li, A. C. Bartnik, C. J. R. Duncan, M. Kaemingk, C. A. Pennington, I.V. Bazarov, Y.-K. Kim, and J. M. Maxson. Four-dimensional emittance measurements of ultrafast electron diffraction optics corrected up to sextupole order. *Manuscript submitted for publication*.

[51] Ya-Qing Bie, Alfred Zong, Xirui Wang, Pablo Jarillo-Herrero, and Nuh Gedik. A versatile sample fabrication method for ultrafast electron diffraction. *Ultramicroscopy*, 230:113389, 2021.

[52] Elspeth F. Garman. Developments in x-ray crystallographic structure determination of biological macromolecules. *Science*, 343(6175):1102–1108, 2014.

[53] Adam Bartnik, Colwyn Gulliford, Ivan Bazarov, Luca Cultera, and Bruce Dunham. Operational experience with nanocoulomb bunch charges in the Cornell photoinjector. *Phys. Rev. ST Accel. Beams*, 18(8):083401, August 2015.

[54] David H. Dowell, Erik Jongewaard, James Lewandowski, Cecile Limborg-Deprey, Zenghai Li, John Schmerge, Arnold Vlieks, Juwen Wang, and Liling Xiao. The Development of the Linac Coherent Light Source RF Gun, March 2015.

[55] David H. Dowell, Feng Zhou, and John Schmerge. Exact cancellation of emittance growth due to coupled transverse dynamics in solenoids and rf couplers. *Phys. Rev. Accel. Beams*, 21(1):010101, January 2018.

[56] Lianmin Zheng, Jiahang Shao, Yingchao Du, John G. Power, Eric E. Wisniewski, Wanming Liu, Charles E. Whiteford, Manoel Conde, Scott Doran, Chunguang Jing, Chuanxiang Tang, and Wei Gai. Experimental demonstration of the correction of coupled-transverse-dynamics aberration in an rf photoinjector. *Phys. Rev. Accel. Beams*, 22(7):072805, July 2019.

[57] P. Denham, F. Cropp, and P. Musumeci. Analysis of skew quadrupole compensation in rf-photoinjectors, 2020.

[58] Ji Qiang, Scott Anderson, David Dowell, Paul Emma, John Schmerge, Mark Woodley, and Feng Zhou. Beam Dynamics Simulation of the Solenoid Sextupole Error in the LCLS-II Injector. In *9th International Particle Accelerator Conference*, 6 2018.

[59] J. Qiang, S. Paret, A. Ratti, J. Barranco, T. Pieloni, G. Arduini, X. Buffat, and Y. Papaphilippou. Simulation of beam-beam interaction with crab cavities for lhc upgrade. *Nuclear Instruments and Methods in Physics Research Section A: Accelerators, Spectrometers, Detectors and Associated Equipment*, 900:53–59, 2018.

[60] Oleg Chubar, Pascal Elleaume, and Joel Chavanne. A three-dimensional magnetostatics computer code for insertion devices. *Journal of Synchrotron Radiation*, 5(3):481–484, May 1998.

[61] Eric W. Weisstein. Circle packing.

[62] M. Gordon, S. B. van der Geer, J. Maxson, and Y.-K. Kim. Point-to-point coulomb effects in high brightness photoelectron beam lines for ultrafast electron diffraction. *Phys. Rev. Accel. Beams*, 24:084202, Aug 2021.

[63] Sol M. Gruner, Don Bilderback, Ivan Bazarov, Ken Finkelstein, Geoffrey Krafft, Lia Merminga, Hasan Padamsee, Qun Shen, Charles Sinclair, and Maury Tigner. Energy recovery linacs as synchrotron radiation sources (invited). *Review of Scientific Instruments*, 73(3):1402–1406, 2002.

[64] P. Emma, R. Akre, J. Arthur, R. Bionta, C. Bostedt, J. Bozek, A. Brachmann, P. Bucksbaum, R. Coffee, F. J. Decker, Y. Ding, D. Dowell, S. Edstrom, A. Fisher, J. Frisch, S. Gilevich, J. Hastings, G. Hays, Ph. Hering, Z. Huang, R. Iverson, H. Loos, M. Messerschmidt, A. Miahnahri, S. Moeller, H. D. Nuhn, G. Pile, D. Ratner, J. Rzepiela, D. Schultz, T. Smith, P. Stefan, H. Tompkins, J. Turner, J. Welch, W. White, J. Wu, G. Yocky, and J. Galayda. First lasing and operation of an ångstrom-wavelength free-electron laser. *Nature Photonics*, 4(9):641–647, 2010.

[65] T. van Oudheusden, E. F. de Jong, S. B. van der Geer, W. P. E. M. Op 't Root, O. J. Luiten, and B. J. Siwick. Electron source concept for single-shot sub-100 fs electron diffraction in the 100 kev range. *Journal of Applied Physics*, 102(9):093501, 2007.

[66] Ivan V. Bazarov, Bruce M. Dunham, Yulin Li, Xianghong Liu, Dimitre G. Ouzounov, Charles K. Sinclair, Fay Hannon, and Tsukasa Miyajima. Thermal emittance and response time measurements of negative electron affinity photocathodes. *Journal of Applied Physics*, 103(5):054901, 2008.

[67] Hyeri Lee, Siddharth Karkare, Luca Cultrera, Andrew Kim, and Ivan V. Bazarov. Review and demonstration of ultra-low-emittance photocathode measurements. *Review of Scientific Instruments*, 86(7):073309, 2015.

[68] Luca Serafini and James B. Rosenzweig. Envelope analysis of intense relativistic quasilaminar beams in rf photoinjectors:ma theory of emittance compensation. *Phys. Rev. E*, 55:7565–7590, Jun 1997.

[69] Christopher M. Pierce, Matthew B. Andorf, Edmond Lu, Colwyn Gulliford, Ivan V. Bazarov, Jared M. Maxson, Matthew Gordon, Young-Kee Kim, Nora P. Norvell, Bruce M. Dunham, and Tor O. Raubenheimer. Low intrinsic emittance in modern photoinjector brightness. *Phys. Rev. Accel. Beams*, 23:070101, Jul 2020.

[70] S. P. Weathersby, G. Brown, M. Centurion, T. F. Chase, R. Coffee, J. Corbett, J. P. Eichner, J. C. Frisch, A. R. Fry, M. Gühr, N. Hartmann, C. Hast, R. Hettel, R. K. Jobe, E. N. Jongewaard, J. R. Lewandowski, R. K. Li, A. M. Lindenberg, I. Makasyuk, J. E. May, D. McCormick, M. N. Nguyen, A. H. Reid, X. Shen, K. Sokolowski-Tinten, T. Vecchione, S. L. Vetter, J. Wu, J. Yang, H. A. Dürr, and X. J. Wang. Mega-electron-volt ultrafast electron diffraction at slac national accelerator laboratory. *Review of Scientific Instruments*, 86(7):073702, 2015.

[71] Y. Ding, A. Brachmann, F.-J. Decker, D. Dowell, P. Emma, J. Frisch, S. Gilevich, G. Hays, Ph. Hering, Z. Huang, R. Iverson, H. Loos, A. Miahnahri, H.-D. Nuhn, D. Ratner, J. Turner, J. Welch, W. White, and J. Wu. Measurements and simulations of ultralow emittance and ultrashort electron beams in the linac coherent light source. *Phys. Rev. Lett.*, 102:254801, Jun 2009.

[72] Massimo Altarelli et al. XFEL: The European X-Ray Free-Electron Laser. Technical design report. 7 2006.

[73] Jun Feng, J. Nasiatka, Weishi Wan, Siddharth Karkare, John Smedley, and Howard A. Padmore. Thermal limit to the intrinsic emittance from metal photocathodes. *Applied Physics Letters*, 107(13):134101, 2015.

[74] Siddharth Karkare, Gowri Adhikari, W. Andreas Schroeder, J. Kevin Nangoi, Tomas Arias, Jared Maxson, and Howard Padmore. Ultracold electrons via near-threshold photoemission from single-crystal cu(100). *Phys. Rev. Lett.*, 125:054801, Jul 2020.

[75] Martin Reiser. *Linear Beam Optics with Space Charge: Sections 4.1 - 4.4*, chapter 4, pages 163–232. John Wiley & Sons, Ltd, 2008.

[76] A. J. McCulloch, D. V. Sheludko, M. Junker, and R. E. Scholten. High-coherence picosecond electron bunches from cold atoms. *Nat. Commun. 4*, Article number: 1692, 2013.

[77] Dene Murphy, Rory Speirs, D Sheludko, Corey Putkunz, Andrew Mcculloch, Ben Sparkes, and R Scholten. Detailed observation of space-charge dynamics using ultracold ion bunches. *Nature communications*, 5:4489, 07 2014.

[78] B. J. Claessens, S. B. van der Geer, G. Taban, E. J. D. Vredenbregt, and O. J. Luiten. Ultracold electron source. *Phys. Rev. Lett.*, 95:164801, Oct 2005.

[79] J. G. H. Franssen, T. C. H. de Raadt, M. A. W. van Ninhuijs, and O. J. Luiten. Compact ultracold electron source based on a grating magneto-optical trap. *Phys. Rev. Accel. Beams*, 22:023401, Feb 2019.

[80] S.B. van der Geer, M.J. de Loos, E.J.D. Vredenbregt, and O.J. Luiten. Ultracold electron source for single-shot, ultrafast electron diffraction. *Microscopy and Microanalysis*, 15(4):282–289, 2009.

[81] J. G. H. Franssen, T. L. I. Frankort, E. J. D. Vredenbregt, and O. J. Luiten. Pulse length of ultracold electron bunches extracted from a laser cooled gas. *Structural Dynamics*, 4(4):044010, 2017.

[82] WJ Engelen, EP Smakman, DJ Bakker, OJ Luiten, and E J D Vredenbregt. Effective temperature of an ultracold electron source based on near-threshold photoionization. *Ultramicroscopy*, 136:73—80, January 2014.

[83] B. J. Claessens, M. P. Reijnders, G. Taban, O. J. Luiten, and E. J. D. Vredenbregt. Cold electron and ion beams generated from trapped atoms. *Physics of Plasmas*, 14(9):093101, 2007.

[84] Josh Barnes and Piet Hut. A hierarchical o(n log n) force-calculation algorithm. *Nature*, 324(6096):446–449, 1986.

[85] L Greengard and V Rokhlin. A fast algorithm for particle simulations. *Journal of Computational Physics*, 73(2):325 – 348, 1987.

[86] Germán Sciaini and R J Dwayne Miller. Femtosecond electron diffraction: heralding the era of atomically resolved dynamics. *Reports on Progress in Physics*, 74(9):096101, August 2011.

[87] D.O. Gericke and M.S. Murillo. Disorder-induced heating of ultracold plasmas. *Contributions to Plasma Physics*, 43(5-6):298–301, 2003.

[88] Jared Maxson, Ivan Bazarov, Christopher Coleman-Smith, Weishi Wan, and Howard Padmore. Fundamental photoemission brightness limit from disorder induced heating. *New Journal of Physics*, 15, 04 2013.

[89] Daniel H. E. Dubin and T. M. O'Neil. Trapped nonneutral plasmas, liquids, and crystals (the thermal equilibrium states). *Rev. Mod. Phys.*, 71:87–172, Jan 1999.

[90] S. Chandrasekhar. Stochastic problems in physics and astronomy. *Rev. Mod. Phys.*, 15:1–89, Jan 1943.

[91] Pulsar website for gpt. `http://www.pulsar.nl/gpt/`, 2011.

[92] R. Ray and G.D. Mahan. Dynamical image charge theory. *Physics Letters A*, 42(4):301 – 302, 1972.

[93] G.H. Jansen. Coulomb interactions in particle beams. *Nuclear Instruments and Methods in Physics Research Section A: Accelerators, Spectrometers, Detectors and Associated Equipment*, 298(1):496 – 504, 1990.

[94] Colwyn Gulliford, Adam Bartnik, and Ivan Bazarov. Multiobjective optimizations of a novel cryocooled dc gun based ultrafast electron diffraction beam line. *Phys. Rev. Accel. Beams*, 19:093402, Sep 2016.

[95] Colwyn Gulliford, Adam Bartnik, Ivan Bazarov, and Jared Maxson. Multiobjective optimization design of an rf gun based electron diffraction beam line. *Phys. Rev. Accel. Beams*, 20:033401, Mar 2017.

[96] Hyeri Lee, Xianghong Liu, Luca Cultrera, Bruce Dunham, Vaclav O. Kostroun, and Ivan V. Bazarov. A cryogenically cooled high voltage dc photoemission electron source. *Review of Scientific Instruments*, 89(8):083303, 2018.

[97] P.L.E.M. Pasmans, G.B. van den Ham, S.F.P. Dal Conte, S.B. van der Geer, and O.J. Luiten. Microwave tm010 cavities as versatile 4d electron optical elements. *Ultramicroscopy*, 127:19 – 24, 2013. Frontiers of Electron Microscopy in Materials Science.

[98] Dennis T. Palmer, Roger H. Miller, Herman Winick, Xi Jie Wang, Kenneth Batchelor, Martin H. Woodle, and Ilan Ben-Zvi. Microwave measurements and beam dynamics simulations of the BNL/SLAC/UCLA emittance-compensated 1.6-cell photocathode rf gun. In Eric Munro and Henry P. Freund, editors, *Electron-Beam Sources and Charged-Particle Optics*, volume 2522, pages 514 – 526. International Society for Optics and Photonics, SPIE, 1995.

[99] R.B. Neal. *The Stanford two-mile accelerator*. Number v. 1. W. A. Be, 1968.

[100] Ivan V. Bazarov. Synchrotron radiation representation in phase space. *Phys. Rev. ST Accel. Beams*, 15:050703, May 2012.

[101] David Chandler. *Introduction to Modern Statistical Mechanics.* Oxford University Press, 1987.

[102] Baerends E.J. Buijse M.A. *Density Functional Theory of Molecules, Clusters, and Solids*, volume 12 of *Understanding Chemical Reactivity.* Springer, Dordrecht, 1996.

[103] F. Mandl. *Statistical Physics.* Wiley, 2 edition, 2013.

[104] D. Filippetto, P. Musumeci, M. Zolotorev, and G. Stupakov. Maximum current density and beam brightness achievable by laser-driven electron sources. *Phys. Rev. ST Accel. Beams*, 17:024201, Feb 2014.

[105] P. Musumeci, J. T. Moody, R. J. England, J. B. Rosenzweig, and T. Tran. Experimental generation and characterization of uniformly filled ellipsoidal electron-beam distributions. *Phys. Rev. Lett.*, 100:244801, Jun 2008.

[106] S. S. Baturin, I. L. Sheinman, A. M. Altmark, and A. D. Kanareykin. Transverse operator method for wakefields in a rectangular dielectric loaded accelerating structure. *Phys. Rev. ST Accel. Beams*, 16:051302, May 2013.

[107] C. M. Pierce, M. Gordon, et al. Understanding and Compensating Emittance Diluting Effects in Highly Optimized Ultrafast Electron Diffraction Beamlines. In *Proc. 9th International Particle Accelerator Conference (IPAC'18), Vancouver, BC, Canada, April 29-May 4, 2018*, number 9 in International Particle Accelerator Conference, pages 3004–3006, Geneva, Switzerland, June 2018. JACoW Publishing. https://doi.org/10.18429/JACoW-IPAC2018-THPAF024.

[108] D. Dowell. Sources of emittance in rf photocathode injectors: Intrinsic emittance, space charge forces due to non-uniformities, rf and solenoid effects. *Cornell U physics ArXive, http://arxiv.org/abs/1610.01242*, arXiv:1610.01242v3 [physics.acc-ph], 10 2016.